

AD-A096 062

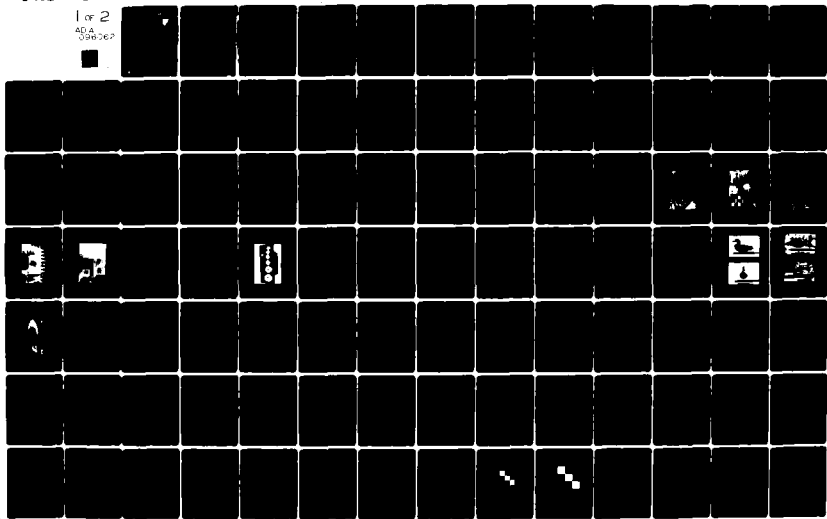
GEORGIA INST OF TECH ATLANTA ELECTROMAGNETIC EFFECTI--ETC F/6 20/3
A STUDY OF THE ANALYSIS AND MEASUREMENTS OF THREE-DIMENSIONAL A--ETC(U)
DEC 80 J J WANG, C PAPANICOLOPULOS F19628-78-C-0223

UNCLASSIFIED

RADC-TR-80-372

NL

1 of 2
40A
309262



LEVEL II

12
BS

RADC-TR-80-372
Final Technical Report
December 1980



AD A 098962

A STUDY OF THE ANALYSIS AND MEASUREMENTS OF THREE-DIMENSIONAL ARBITRARILY-SHAPED DIELECTRIC SCATTERERS

Georgia Institute of Technology

J. J. H. Wang
C. Papanicolopoulos

DTIC
ELECTE
MAR 0 6 1981
S D
E

APPROVED FOR PUBLIC RELEASE; DISTRIBUTION UNLIMITED

FILE COPY

ROME AIR DEVELOPMENT CENTER
Air Force Systems Command
Griffiss Air Force Base, New York 13441

81 3 06 063

This report has been reviewed by the RADC Public Affairs Office (PA) and is releasable to the National Technical Information Service (NTIS). At NTIS it will be releasable to the general public, including foreign nations.

RADC-TR-80-372 has been reviewed and is approved for publication.

APPROVED: 

OTHO E. KERR
Project Engineer

APPROVED: 

ALLAN C. SCHELL
Chief, Electromagnetic Sciences Division

FOR THE COMMANDER: 

JOHN P. HUSS
Acting Chief, Plans Office

If your address has changed or if you wish to be removed from the RADC mailing list, or if the addressee is no longer employed by your organization, please notify RADC (EEC) Hanscom AFB MA 01731. This will assist us in maintaining a current mailing list.

Do not return this copy. Retain or destroy.

UNCLASSIFIED

SECURITY CLASSIFICATION OF THIS PAGE (When Data Entered)

18
6

19 REPORT DOCUMENTATION PAGE

READ INSTRUCTIONS BEFORE COMPLETING FORM

1. REPORT NUMBER RADG TR-84-572	2. GOVT ACCESSION NO. AD A096062	3. RECIPIENT'S CATALOG NUMBER
4. TITLE (and Subtitle) A STUDY OF THE ANALYSIS AND MEASUREMENTS OF THREE-DIMENSIONAL ARBITRARILY-SHAPED DIELECTRIC SCATTERERS	5. TYPE OF REPORT & PERIOD COVERED Final Technical Report Sep 78 - Sep 80	6. PERFORMING ORG. REPORT NUMBER N/A
7. AUTHOR J. J. H. Wang C. Papanicolaou	8. CONTRACT OR GRANT NUMBER(s) F19628-78-C-0223	
9. PERFORMING ORGANIZATION NAME AND ADDRESS Georgia Institute of Technology Engineering Experiment Station Atlanta GA 30332	10. PROGRAM ELEMENT PROJECT TASK AREA & WORK UNIT NUMBERS 61102F 23051437	17-4
11. CONTROLLING OFFICE NAME AND ADDRESS Deputy for Electronic Technology (RADG/EEC) Hanscom AFB MA 01731	12. REPORT DATE Dec 1980	
14. MONITORING AGENCY NAME & ADDRESS (if different from Controlling Office) None	13. NUMBER OF PAGES 121	15. SECURITY CLASS. for this report. UNCLASSIFIED
15. DISTRIBUTION STATEMENT (of this Report) Approved for public release; distribution unlimited.	16. DECLASSIFICATION/DOWNGRADING SCHEDULE N/A	
17. DISTRIBUTION STATEMENT (of the abstract entered in Block 20, if different from Report) None		
18. SUPPLEMENTARY NOTES RADG Project Engineer: Gene E. Kerr (RADG/EEC)		
19. KEY WORDS (Continue on reverse side if necessary and identify by block number) Method of Moments Arbitrarily-shaped Dielectric Scatterers Electromagnetic Scattering and Radiation Integral Equation Solution Muller-Green's Function		
20. ABSTRACT (Continue on reverse side if necessary and identify by block number) Theoretical and experimental research was conducted to determine the electromagnetic scattering from heterogeneous dielectric bodies. The discrepancies in the literature regarding the singularity of the electric dyadic Green's functions were resolved and a unified and consistent view is presented. Compact range scattering measurements at 1 GHz were successfully performed. Extensive computations were made for a variety of dielectric scatterers, including a one-foot (Cont'd)		

UNCLASSIFIED

SECURITY CLASSIFICATION OF THIS PAGE (When Data Entered)

UNCLASSIFIED

SECURITY CLASSIFICATION OF THIS PAGE(When Data Entered)

Item 20 (Cont'd)

bird at 1 GHz. The agreements between measurements and computation were good except for the case of the sphere. Various computational techniques for handling large matrices were studied and a new local-file manipulation technique has been explored and found to be potentially useful.

UNCLASSIFIED

SECURITY CLASSIFICATION OF THIS PAGE(When Data Entered)

SUMMARY

The objective of this program is to conduct theoretical and experimental research to determine the electromagnetic scattering from heterogeneous dielectric bodies as individual bodies and as a cluster of bodies. The discrepancies in the literature regarding the singularity of the electric dyadic Green's functions were resolved and a unified and consistent view is presented. Compact range scattering measurements at 1 GHz were successfully performed to obtain measured data to validate the numerical analyses. Extensive computations were made for a variety of dielectric scatterers, including a one-foot bird at 1 GHz. The agreements between measurement and computation were good except for the resonant sphere, for which the calculated resonant frequencies were shifted by about 20 percent. Various numerical techniques were investigated successfully for implementation in the volume methods to treat symmetrical scatterers through use of symmetric matrices, the use of banded matrices, and virtual memory. A new local-file manipulation technique for handling large matrices has been explored and found to be potentially useful.

There has been very little research into the problem of scattering by dielectric objects of complex permittivity. Future research in this area should include the investigation of the surface integral equation technique and the exact solution for the dielectric prolate spheroid.

Distribution For	
CONFIDENTIAL	<input checked="" type="checkbox"/>
SECRET	<input type="checkbox"/>
RESTRICTED	<input type="checkbox"/>
UNCLASSIFIED	<input type="checkbox"/>

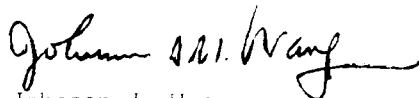
A

PREFACE

The research on this contract was carried out in the Electromagnetic Effectiveness Division of the Electronics Technology Laboratory of the Engineering Experiment Station at the Georgia Institute of Technology, Atlanta, Georgia 30332. Dr. Johnson J. Wang served as the Project Director. This program is sponsored by the Rome Air Development Center, Air Force Systems Command and was designated on Georgia Tech Project A-2212. This final report covers the work which was performed from 1 September 1978 to 31 August 1980.

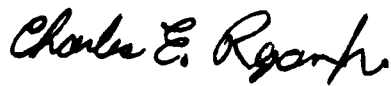
The authors wish to express their gratitude to Mr. Otho E. Kerr, Drs. John K. Schindler and Lee Poirier for their interest and support in this research. The authors also acknowledge the various contributions in the compact-range scattering measurements by Messrs. E. E. Weaver, W. P. Cooke, F. L. Cain and Dr. C. E. Ryan, Jr. as well as the expert programming assistance by Mr. Dwight Rudoiph.

Respectfully submitted,



Johnson J. Wang
Project Director

Approved:



Charles E. Ryan, Jr.
Chief,
EM Effectiveness Division

TABLE OF CONTENTS

Chapter		Page
	CONTENTS	
	I. UNIFIED AND CONSISTENT VIEW OF THE ELECTRIC II. THE ELECTRIC BIADIC GREEN'S FUNCTIONS OF THE SOURCE REGION	3
	A. Introduction	3
	B. A Unified and Consistent View.	7
	C. Various Forms of G^E for the Rectangular Cavities	17
III.	COMPACT RANGE SCATTERING MEASUREMENT.	24
	A. Compact range Scattering Measurement Techniques at 1 GHz.	24
	B. Simulation of Biological Bodies.	40
IV.	NUMERICAL COMPUTATIONS FOR VARIOUS DIELECTRIC SCATTERERS.	45
	A. Scatterers of Simple Shapes.	49
	B. Scatterer Computation for 1-foot Birds.	63
V.	IMPROVEMENTS OF COMPUTER ALGORITHM.	74
	A. Symmetrical Matrices	74
	B. Symmetrical scatterers	74
	C. Banded Matrix Techniques	77
	D. Virtual Memory Technique	82
	E. Local-file Manipulation Technique.	83
VI.	METHODOLOGY FOR THE MODELING OF THE SCATTERING OF A FLOCK OF FLYING BIRDS.	91
VII.	CONCLUSIONS AND RECOMMENDATIONS	94
VIII.	REFERENCES.	96
<u>Appendices</u>		
I.	SUBROUTINES USED IN LOCAL-FILE MANIPULATION ALGORITHM	100
II.	MATRIX SOLUTION BY THE LOWER-UPPER DECOMPOSITION METHOD.	103

LIST OF FIGURES

<u>Figure</u>	<u>Page</u>
1. A three-dimensional boundary-value problem in which V is the source region and V_t , V_s , V_e are volumes enclosed by surfaces S_t , S_s and S_e , respectively. . . .	4
2. A pillbox principal volume cutting the volume cell V_D into two boxes.	13
3. Block diagram for 1 GHz compact range RCS measurement .	25
4. The arrangement of the shock-mounted cancellation network used in the 1 GHz scattering measurements	26
5. The dual-channel receiving system used in the compact range measurement	27
6. Partial view of the 12-foot high, 16-foot wide reflector used in the compact range	28
7. The rectangular horn with a 24 in. x 32 1/2 in. aperture used as a feed for the reflector in the compact range	29
8. Styrofoam support for the scattering target used in the compact range	30
9. Stainless-steel spheres used in the calibration of the scattering measurement.	33
10. Comparison between compact range measurements and other known data for a finite circular cylinder	
a) E-plane pattern	34
b) H-plane pattern	35
11. Comparisons of measured and calculated backscattering cross-section of a square plate.	
a) backscattering pattern as a function of elevation angle	36
b) Backscattering cross-section as a function of plate size.	37
12. Compact range scattering measurement of conducting boxes.	
a) Backscatter as a function of length as viewed from the side.	38
b) Backscatter as a function of length as viewed from the end	39
13. Side and front views of a sitting bird made of plaster of paris.	41

LIST OF FIGURES (Continued)

Figure	Page	
14.	Side view of a "Super-stuff" simulated bird, SB4, in a styrofoam holder	42
15.	Side view of a "Super-stuff" simulated bird, SB4, in a styrofoam holder	43
16.	Comparison between the calculated results and Richmond's data for a dielectric cylinder.	47
17.	A rectangular box of saline water under plane wave excitation (numbers are the index numbers for the volume cells)	48
18.	Comparison between calculated and measured RCS of square boxes of saline water shown in Figure 18.	52
19.	An I-shaped box of saline water under plane wave excitation (numbers are the index numbers for the volume cells)	54
20.	Comparison between calculated and measured RCS of I-shaped boxes of saline water.	61
21.	Calculation of RCS of a sphere with a dielectric constant of 2.92 as a function of radius a	62
22.	Calculation of back-scatter cross-section for a sphere of radius a and $\epsilon_p = 29.43 - j0.158$	63
23.	Calculation of back-scatter cross-section for a sphere of radius a and $\epsilon_p = 29.43 - j0.158$	64
24.	Side(a), front(b), and top(c) views of the 118 cell bird no. SB-4 to simulate a 0.3 pound Green-Winged Teal, $\epsilon_p = 47.0 - j13.2$	66
25.	Simulated bird model SB4 under plane wave excitation.	67
26.	Back scattering cross section of bird SB4 versus elevation angle θ with vertical polarization as shown in Figures 25 and 26.	68
27.	Back scattering cross section of bird SB4 versus elevation angle θ with horizontal polarization as shown in Figures 25 and 26.	69
28.	A symmetrical scatterer illuminated by a plane wave incident in the plane of symmetry	72
29.	A scattering problem with two-plane symmetry.	76

LIST OF FIGURES (Continued)

<u>Figure</u>	<u>Page</u>
30. A display of the magnitude of matrix elements in a VIE matrix for an 8-cell dielectric cylinder which is strongly banded.	79
31. A display of the magnitude of matrix elements in a VIE matrix for a 12-cell prolate spheroid which is weakly banded	80
32. Convergence of solution for the case of a 12-cell prolate spheroid expressed in percentage of error as a function of the normalized width of diagonal band.	81
33. Block diagram for the local-file manipulation algorithm	84
34. The local-file simultaneous storage process for the i^{th} , $(i + N)^{\text{th}}$ and $(i + 2N)^{\text{th}}$ rows in a large $3N \times 3N$ matrix.	86
35. Comparison of computer time required to generate (including input/output time) a matrix of various sizes by various matrix storage methods	88
36. Comparison of matrix solution time on CDC CYBER-74 by various methods.	89
37. A flock of birds illuminated by a radar wave.	92

LIST OF TABLES

<u>Table</u>		<u>Page</u>
I.	COMPARISON BETWEEN COMPACT RANGE MEASUREMENT AND EXACT CALCULATIONS FOR CONDUCTING SPHERES CALIBRATED WITH THE 0.04403 λ SPHERE.	32
II.	ELECTRIC FIELD DISTRIBUTION IN THE 36-CELL RECTANGULAR BLOCK.	49
III.	ELECTRIC FIELD DISTRIBUTION IN THE 128-CELL BLOCK. . .	55
IV.	SUBROUTINES USED IN THE LOCAL-FILE MANIPULATION ALGORITHM.	85

SECTION I
INTRODUCTION

During the past decade, there has been a rapidly rising interest in electromagnetic problems involving dielectric objects. The interest in this area arises from a multitude of military and civilian needs. Human beings are increasingly more exposed to microwave radiation hazards on aircraft, ships, military installations and even in their homes. The knowledge of the electromagnetic scattering from birds, animals and humans is essential in the analysis of detection, identification and interference problems in radar systems. Biological and medical applications, such as blood thawing, enzyme inactivation and hyperthermia treatment of cancerous tissues, also demand accurate knowledge of the electromagnetic fields in dielectric bodies. Thus, electromagnetic scattering by dielectric bodies is a fundamental and important problem, and solutions for these scatterers have wide application.

Since September 1978, Georgia Tech has been supported by the Deputy for Electronic Technology (RADC/EEC), Air Force Systems Command, under contract F19628-78-C-0223 to conduct a two-year research program in this area. The emphasis is focused on analyses and measurements of the scattering characteristics of heterogeneous dielectric objects as individual bodies and as a cluster of bodies. Progress to date has included the clarification of discrepancies in the literature on the singularity of the Green's function in the source region, and measurements and calculations of the scattering cross-section of dielectric bodies of arbitrary shapes and complex dielectric constants. In addition, various numerical techniques have been investigated and a new local-file manipulation technique was explored and found to be potentially useful.

Numerical techniques developed in the current research program are capable of producing fairly accurate data for objects less than one free-space wavelength long. There are models for which the present technique is highly accurate, and there are geometries, such as the sphere, for which the present technique is not quite satisfactory probably due to the inherent deficiencies of the volume integral equation method.

The success of compact-range scattering measurements at a frequency of 1 GHz represents an advance in the state-of-the-art of scattering measurements using the compact range technique. This extension of the compact range scattering measurements to lower frequencies demonstrates the versatility and usefulness of the compact range as a general purpose EM measurements facility.

Introduction

The problem of the interaction of a point charge with a dielectric

medium has been extensively discussed (1,2). The electric image charge function, which relates the current source and the electric field, is simpler in the static region and is difficult to handle. There have been various discussions regarding the treatment of the static field in the dynamic case as well as the radiation reaction. The present paper is devoted to the use of the Green's function method. In the analysis, it is not necessary to calculate the electric field directly. By using the mathematical properties of the Green's function, the Green's functions, which are related to the radiation reaction, are presented in the report.

The following is the time-dependent Maxwell equation for

$$\text{div } \mathbf{E} = -\nabla \cdot \mathbf{j} - \rho$$

where \mathbf{E} is the electric field, \mathbf{j} is the current density, ρ is the charge density, and ∇ is the gradient operator. The boundary conditions can be written in the form of an infinite series of terms. The boundary conditions are given as follows:

$$\text{div } \mathbf{E} = \int_V \mathbf{E} \cdot \nabla' \delta(\mathbf{r} - \mathbf{r}') dV'$$

where G^e is called the electric dyadic Green's function, which can be derived either by the method of potential or the summation method. In the latter method, G^e is derived by solving the following equation

$$(\nabla \cdot \nabla - k^2) G^e(\mathbf{r}, \mathbf{r}') = -\mathbf{I} \delta(\mathbf{r} - \mathbf{r}')$$

subject to all the applicable boundary conditions for \mathbf{E} and \mathbf{j} . The Dirac-delta function and \mathbf{I} is a unit dyad. The presence of the delta

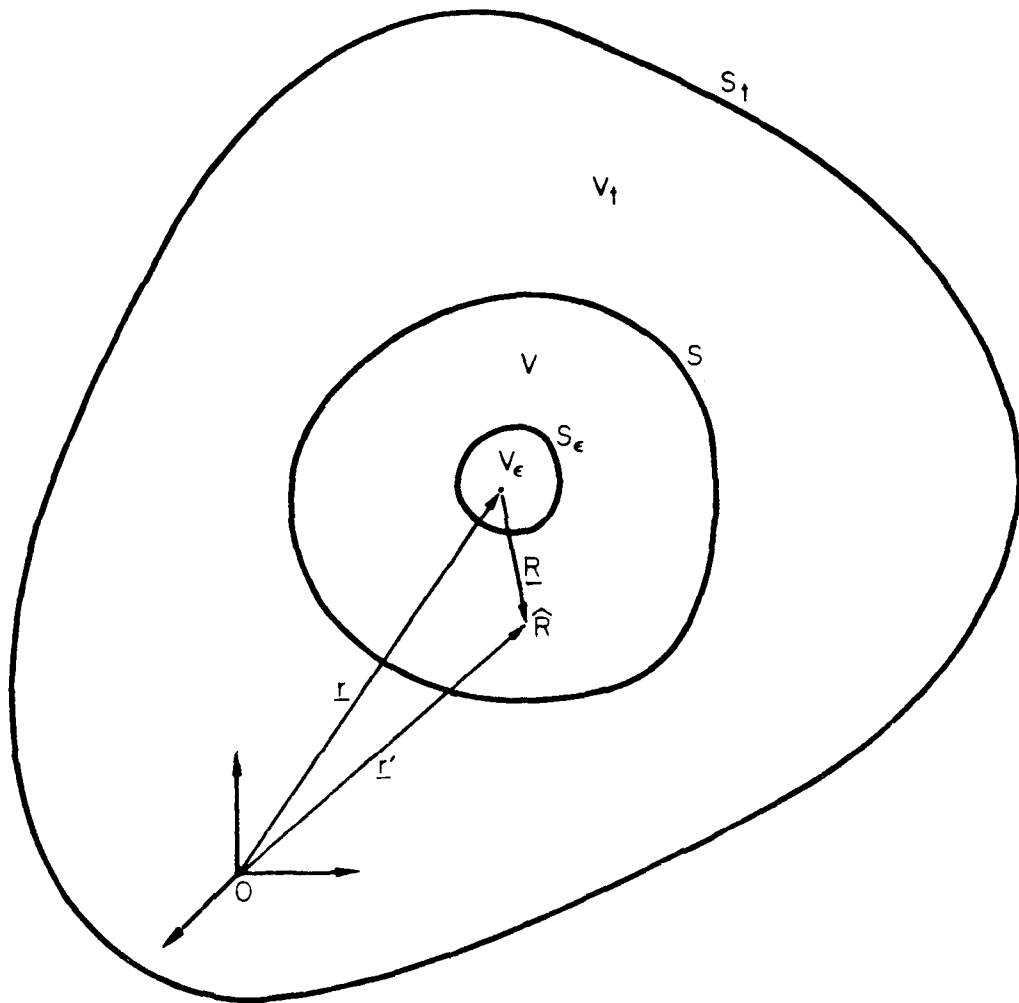


Figure 1. A three-dimensional boundary-value problem in which V is the source region and V_t , V , V_ϵ are volumes enclosed by surfaces S_t , S and S_ϵ , respectively.

reaction dictates that G_0^e as obtained from equation (3) should be viewed in the light of the theory of distributions.

In an unbounded region, the electric field $E(r)$ is given by the iteration as

$$G_0^e(r, r') = -\frac{j\omega\mu_0}{4\pi} \left(1 + \frac{-j}{k^2} \nabla^2\right) g_1(r, r') \quad (4)$$

where

$$g_1(r, r') = \frac{e^{-jkR}}{R}, \quad \text{and} \quad (5a)$$

$$R = |r - r'|. \quad (5b)$$

In the source region where $r = r'$, questions arise as to whether (4) is still valid and, if valid, how to compute it since the R^{-3} term in (4) is in general not integrable [3]. For the static case in which $k = 0$, the rigorous treatment by Kellogg [3] is applicable. Using the method of retarded potential, Van Bladel [4] showed that

$$E(r) = PV \int_V \underline{J}(r') \cdot G_0^e(r, r') dV' - \frac{\underline{J}(r)}{3j\omega\epsilon_0}. \quad (6)$$

"PV" in Equation (6) denotes "Principal Value" integration, which specifies an integration carried out over the volume $V - V_0$, where V_0 is an infinitesimal spherical volume centered at r .

With a rigorous classical procedure similar to Kellogg's treatment of the static case, Fikioris [5] derived the following expression

$$E(r) = \int_{V-V_D} \underline{J}(r') \cdot G_0^e(r, r') dV' + \int_{V_D} [\underline{J}(r') - \underline{J}(r)] \cdot G_0^e(r, r') dV' + \frac{\underline{J}(r)}{3j\omega\epsilon_0} \left[\frac{j}{3} e^{-jka} (1 + jka) - 1 \right], \quad (7)$$

where a is the radius of a finite spherical volume V_D centered at \underline{r} . He also indicated that V_D does not have to be spherical but is not permitted, in general, to be infinitesimal. If V_D assumes other geometries, the third term on the right side of Equation (7) will have to be modified accordingly. Equation (6) also answered implicitly the question as to how to evaluate the principal-value integration in Equation (6). Thus, for a spherical principal volume of radius a and a constant current \underline{J} ,

$$\text{PV} \int_V \underline{J}(\underline{r}) \cdot \underline{G}^e(\underline{r}, \underline{r}') dV' = \frac{\underline{J}(\underline{r})}{j\omega\epsilon} \cdot \frac{2}{3} e^{-jka} (1 + jka). \quad (8)$$

As will be discussed later, Equations (6) and (8) form the basis on which numerical analyses using free-space electric dyadic Green's function were carried out [6-8].

Chen [9] showed that the infinitesimal principal volume V_c can assume other geometries as long as the integrals over V_c and $V-V_c$ are properly handled. He also derived, as examples, expressions similar to Equation (6) for principal volumes in the shapes of the cube and the circular cylinder.

For fields in the bounded regions, the electric dyadic Green's functions for rectangular cavities and waveguides were discussed by various authors [10-16]. Their expressions are in the form of eigenfunction expansions plus a term containing the Dirac-delta function. Perhaps considering the delta function to be the only singular term, Yaghjian [17] explained the difference in the delta-function terms between Tai, et al. [11] and Rahmat-Samii [12] as being due to their different choices of the principal volume V_c and emphasized the need to include in G^e the shape of the principal volume involved. Johnson, et al., [16] also pointed out the ambiguities in the literature. Recently, Lee, et al. [18] examined this problem from the viewpoint of the potential theory and obtained expressions for the general problem. Most of their conclusions support existing results,

but questions concerning the usefulness of an infinitesimal principal volume V_0 in numerical analyses were raised.

Proper handling of the electric field integral equation in the source region is essential when using it in numerical analyses involving dielectric scatterers. The difficulty arises in the calculation of the "self-cell" or self-coupling matrix elements that must be generated when using the method of moments. For the free space [6,8] and half-space [7], Equations (6) and (8), which are consistent with Equation (7), were employed in the scattering analysis of arbitrarily-shaped dielectric bodies. For the rectangular waveguide [19], the expressions of Tai [10] and Rahmat-Samii [12] were used. To the practicing engineer, it is desirable to remove all discrepancies and subtleties. In the following, it is shown that uniformity and consistency in this subject can be reached on the basis of mathematical analyses and numerical experiments.

B. A Unified and Consistent View

Discussions of the singularity associated with the electric dyadic Green's function in the free space are comprehensive in the literature and opinions are not seriously divided. However, for the bounded regions, such as waveguides and cavities, the discussions are more discordant. The problem can be treated either by the distribution theory or by classical analysis (as in the potential theory). Much of the confusion can be removed by a clear distinction between a classical function and a distribution (or generalized function).

Let us consider the function $g(\mathbf{r}, \mathbf{r}') = \nabla \cdot \nabla' G(\mathbf{r}, \mathbf{r}')$ where $G(\mathbf{r}, \mathbf{r}')$ is the electric dyadic Green's function in the free space. It can be treated in the sense of a classical function. It can also be treated as a distribution. For which only the definition of the distribution is needed. It will be shown that the two approaches are equivalent. In the latter case, we can use the method of potential to obtain the Green's function $G(\mathbf{r}, \mathbf{r}')$ and then differentiate it with respect to \mathbf{r}' .

where the vector \mathbf{A} is defined as well as the vector \mathbf{J} in [1] and [2]. The vector \mathbf{A} satisfies the Lorentz condition and the inhomogeneous Helmholtz equation

$$\nabla^2 \mathbf{A} = -\mathbf{J}(\mathbf{r}, t) + \frac{1}{c^2} \dot{\mathbf{J}}(\mathbf{r}, t) \quad (9a)$$

$$\nabla \cdot \mathbf{A} = \int_V \frac{1}{|\mathbf{r} - \mathbf{r}'|} \nabla' \cdot \mathbf{J}(\mathbf{r}', t) \quad (9b)$$

The vector \mathbf{A} satisfies the Lorentz condition and the inhomogeneous Helmholtz equation

$$\nabla^2 \mathbf{A} = -\mathbf{J}(\mathbf{r}, t) + \frac{1}{c^2} \dot{\mathbf{J}}(\mathbf{r}, t) \quad (9a)$$

subject to the appropriate boundary conditions. The boundary conditions are that \mathbf{A} is finite everywhere, that the radiation condition $\mathbf{A} \cdot \mathbf{R} = 0$ and $\nabla \times \mathbf{A} \cdot \mathbf{R} = 0$ as $R \rightarrow \infty$ exist, and that for the free-space case, the rectangular waveguide and cavity, and the half-space, etc. has been well documented in the literature. Since the integrand in Equation (9b) is less singular than R^{-2} , in fact it is R^{-1} in free-space, the integral in Equation (9b) converges [3, p.148]. By substituting equation (9a) into Equation (9a) and assuming that \mathbf{J} satisfies the so-called "Hölder Condition", it was proved by Kellogg [3] and Fikioris [5] for $k = 0$ and $k \neq 0$ respectively that $\nabla \cdot \mathbf{A}$ exists for the free-space case. This conclusion was later expanded to the bounded regions of waveguides and cavities by Yaghjian [17] and Lee, et al. [18]. It is interesting to note that by assuming the first-order differentiability of \mathbf{J} , Van Bladel [4] was able to establish similar results by using the relations between surface

and volume integrals such as the divergence (Gauss) theorem. The Hölder condition is stronger than continuity, but may be either weaker or stronger than differentiability.

The potential approach is based on familiar and well-established classical analytical techniques and there are no identifiable disputes regarding it. If we choose the delta-function approach based on Equation (3), we should treat it as a distribution. \underline{G}^e is no longer a classical function, but is defined only when it is used in an integral [2,21]. Now, if \underline{G}^e is expressed in terms of functions that appear to be conventional, one may be misled to regard \underline{G}^e as being also conventional. For example, [22, p. 200] in

$$\nabla^2 \left(\frac{e^{-jkR}}{4\pi R} \right) + k^2 \frac{e^{-jkR}}{4\pi R} = -\delta(\mathbf{r}) \quad (11)$$

the left side of the equation appears to be a classical function but can only be defined as a distribution at $R = 0$. Note that the left side of Equation (11) contains a R^{-3} singular term and is closely related to the singular behavior of the free-space electric dyadic Green's function.

Historically, the free-space \underline{G}^e is closely associated with the method of potential and \underline{G}^e for the bounded region is more closely associated with the method of distribution. They are discussed separately as follows.

1. \underline{G}^e for the Free-space

If the current distribution satisfies the so-called Hölder Condition, the electric field in the free-space can be expressed in terms of the electric dyadic Green's function in the following general form

$$\begin{aligned}
\underline{E}(\underline{r}) = & \int_{V-V_{\epsilon}} \underline{J}(\underline{r}') \cdot \underline{G}^e(\underline{r}, \underline{r}') dV' \\
& + \int_{V_{\epsilon}} \{ \underline{J}(\underline{r}') \cdot \underline{G}^e(\underline{r}, \underline{r}') - \underline{J}(\underline{r}) \cdot \underline{G}_0(\underline{r}, \underline{r}') \} dV' \\
& - \frac{1}{j\omega\epsilon} \underline{J}(\underline{r}) \cdot \int_{S_{\epsilon}} \frac{\hat{\underline{n}}'R}{4\pi R^2} ds'
\end{aligned} \tag{12}$$

where

$$\underline{G}_0(\underline{r}, \underline{r}') = \frac{1}{j\omega\epsilon} \nabla' \nabla' \cdot \frac{1}{4\pi R} \tag{13}$$

and where for the free space

$$\underline{G}^e(\underline{r}, \underline{r}') = \underline{G}_0^e(\underline{r}, \underline{r}') \tag{14}$$

Equation (12) applies also to regions for which σ_{ϵ} is perfectly conducting and \underline{G}^e satisfies a $\nabla \cdot \underline{G}$ on S_{ϵ} . For the free-space case, the derivation of equation (12) is similar to the work of Lee, et al. [18], which starts from a vector potential expression for the electric field. This expression can be obtained by a somewhat less rigorous method, also based on the method of potential, using relations between surface and volume integrals, such as the divergence theorem [23]. This alternative method is similar to that of Van Bladel [4] and the classical portion of Lee, et al. [18] and must rely on the existence of the first derivative of the current \underline{J} at the singular point $\underline{r} = \underline{r}'$. In practice, this slight difference in requirements for \underline{J} is not considered to be significant.

If we let the maximum cord of V_{ϵ} vanish, the following expression by Yaghjian [17] emerges from Equation (12)

as well. It must also be pointed out that the evaluation of the integrals over $V-V_\epsilon$ and V_ϵ for a finite V_ϵ is by no means simple and is likely to depend on the particular problem under consideration. Thus, the claim that an infinitesimal principal volume V_ϵ is not suitable for numerical computation appears at best premature.

b. G^e in Regions Bounded by Conducting Surfaces

A very important feature of G^e for the bounded region is that expressions in the literature have been derived from the Ohm-Rayleigh method which expands the Dirac-delta function in terms of the eigenfunctions of a homogeneous Helmholtz equation [2]. Consequently, G^e derived by this method is based on the distribution theory and must be understood as a distribution, or generalized function. Furthermore, being a distribution, G^e does not necessarily need the special handling for its singularity through the principal volume approach since the purpose of the distribution expressions are for the handling of singular integrands. Both the distribution approach and the principal volume approach are discussed in the following.

Yaghjian [17] and Lee, et al. [18], outlined proofs to show that the singularity associated with the electric dyadic Green's function in a bounded region is exactly the same as that for the free-space. Specifically, equations (12) and (13) hold in the bounded region as well if G^e satisfies the radiation condition $\hat{n} \times G^e = 0$ on S , and S is either infinite or perfectly conducting, or both. Waveguides and cavities with perfectly conducting walls are in this category. If the conductivity on the boundary is imperfect, one may still be able to use the equivalent volume current theorem to recast the problem into the ideal case involving either infinite regions or perfectly conducting boundaries.

Derivation of Equation (12) for the bounded region can be carried out by the method of potentials using the standard procedure [17] and [18] and the relationship between G^c and G^s [19]. It should be emphasized that the integrand in (12) should be differentiable.

Since G^c for the bounded regions is often derived from the Ohm-Raleigh method, and hence is a distribution, it can be used either in conjunction with Equation (12) or directly as a distribution. By either method, one should obtain the same results for the electric field.

Numerical computations involving G^c in a bounded region were conducted by Wang [19] in determining the field intensity in an arbitrarily-shaped dielectric or biological body inside a rectangular waveguide. Since G^c is derived by the Ohm-Raleigh method, the question as to what G^c is at $r = r'$ need not be a matter of concern. Meanwhile, the principal volume integration technique is applicable and useful either as a principal or auxiliary tool but is no longer necessary as it is for the free space region. As the distribution theory is now difficult to use, it must be handled with care.

The most severe difficulty encountered in the analysis of the waveguide problem in reference 19 is the handling of the singular integrand, which was only briefly described in the paper. The method was supported by both the distribution theory and the principal volume approach. In the latter method, a "pill box" principal was chosen but other geometries could be used as long as the integrals were correctly handled.

The electric dyadic Green's function pertaining to a rectangular waveguide was first derived by Lai [10] as follows

$$G_T^E = G^E - \frac{1}{2} \iint_{\Sigma} \delta(z - z') \quad (17)$$

where G^E is a double infinite trigonometric series resulting from an eigenfunction expansion of the boundary-value problem. In using the principal volume method, we choose a pill box to enclose the singular

point \underline{r} as shown in Figure 2. Based on the results of Yaghjian [17], we have

$$\int_{V_D} \underline{J} \cdot \underline{G}_T^e dV' = \lim_{\epsilon \rightarrow 0} \left[\int_{Z_1}^{Z-\epsilon} + \int_{Z+\epsilon}^{Z_2} \right] dz' \int_{X_1}^{X_2} dx' \int_{Y_1}^{Y_2} dY' \underline{J} \cdot \underline{G}^1 - \frac{\hat{J}_z Z}{j\omega\epsilon} \quad (18)$$

The integral over Z' in Equation (18) can be integrated and is described by I in Equations (19-20) of Reference 19. The integration over x and y leads to double infinite series identical to those in Equations (16-18) of Reference 19. The series did not appear to converge when it was first computed numerically. It was found later that the rapidly oscillatory part of this series can be summed up in a closed form and the numerical value of the resulting expression converges satisfactorily [19].

We can also view \underline{G}_T^c as a distribution since it was derived from the delta-function method based on Equation (3). Using the equality

$$\int_a^b \sum_{n=1}^{\infty} g_n(x+t) dt = \sum_{n=1}^{\infty} \int_a^b g_n(x+t) dt \quad (19)$$

which holds for every convergent series of distribution [24, p. 47], we can apply it successively for n and m to obtain, for a constant J ,

$$\int_{V_D} \underline{J} \cdot \underline{G}_T^e dv = \sum_m \sum_n \underline{P} \cdot \underline{f}_m(x) g_n(y) \int_{Z_1}^{Z_2} h(\underline{z}, \underline{z}') dz' - \frac{\hat{J}_z Z}{j\omega\epsilon} \quad (20)$$

where \underline{P} is a vector determined by the polarization and amplitude of \underline{J} . Again, the integral over z' and \underline{f}_m and g_n can be summed up to produce

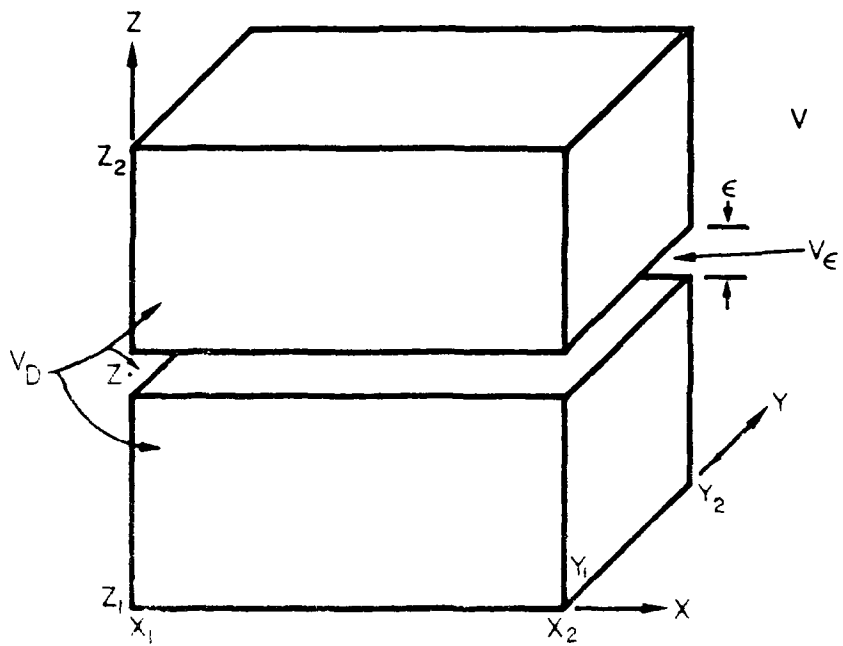


Figure 2. A pillbox principal volume cutting the volume cell V_D into two boxes.

Equations (19-20) and (16-18) in Reference [9]. Thus, Equation (20) is derived from the distribution theory (15) in conjunction with the term $\rho(r)$ in (18) via the principal volume approach.

It is not as difficult to apply (17) and ask what convergence condition is required in the application of Equation (19). According to Schwartz [24,26]

$$\sum_{n=1}^{\infty} (a_n \cos nx + b_n \sin nx)$$

converges distributionally if and only if there is an integer k such

$$|a_n| \leq C |n|^{-k}$$

as $n \rightarrow \infty$. By selecting $k = 2$ for the summation over n and $k = 1$ for the summation over m or vice versa, it can be shown that G^1 is a convergent distribution.

It is also of interest to see what happens if we choose a different principal volume, such as a cube, in using Equation (17). In this case, the second term on the right side of Equation (18) will have to be changed to $-j \cdot \hat{z}$ according to Equation (15). At the same time, V in Figure 2 will have to be reduced and the integral over the added volume in V must be computed and added to the integral on the left of Equation (18). As will become more evident in the next section, G^1 is singular and the integration over these added infinitesimal volumes does not vanish and will, in combination with the rest of the terms, yield the correct value for the electric field.

For J that is not or is not assumed to be constant, Equation (16) can be used in conjunction with Equation (15) (with G_n^1 replaced by G_n , of course) for the principal volume approach. For the distribution approach, the technique of Equation (16) can also be used in Equation (2). The integration of the constant term corresponding to $\delta(r)$ has been discussed and the term corresponding to $t = t(r, r')$ will be an ordinary integral as discussed before.

C. Various Forms of G^e for the Rectangular Cavities

As has been pointed out, G^e for the bounded region derived by the Ohm-Raleigh method is a distribution and must be so treated. Yaghjian [17] and to some extent Johnson, et al. [16] have overemphasized the delta function term. In this section it will be shown that the expressions of Tai and Rozenfeld [11] and Rahmat-Samii [12] are mathematically identical and no discrepancy appears to exist. This finding was previously outlined in a symposium paper [27] and the full derivation follows.

The electric dyadic Green's function derived by Tai and Rozenfeld [11] is of the following form:

$$\underline{G}_I^e = -\frac{1}{k^2} \hat{z} \hat{z} \delta(|\underline{r}-\underline{r}'|) + \sum_{m,n} C_{mn}^* \left[\left(\frac{m}{a} \frac{m'}{a} e + \frac{k_g^2}{k^2} \frac{n}{b} \frac{n'}{b} \right) f_{mn} + \frac{k_g^2}{k^2} \frac{m}{a} \frac{m'}{a} g_{mn} + \frac{k_g^2}{k^2} \frac{n}{b} \frac{n'}{b} \frac{\partial g_{mn}}{\partial z} - \frac{k_g^2}{k^2} \frac{m}{a} \frac{n'}{b} \frac{\partial f_{mn}}{\partial z} \right] \quad (22)$$

where $e^{-j\omega t}$ is implicit and suppressed, and

$$C_{mn}^* = \frac{2(2-\delta_{mn})}{abk_c^2 k_g \sin k_g c} \quad (23)$$

$$f_{mn} = \begin{cases} \text{Sink}_g(c-z) \text{Sink}_g z' \\ \text{Sink}_g z \text{Sink}_g(c-z') \end{cases} \quad \text{for } z > z' \quad (24)$$

$$g_{mn} = \begin{cases} \text{Cosk}_g(c-z) \text{Cosk}_g z' \\ \text{Cosk}_g z \text{Cosk}_g(c-z') \end{cases} \quad \text{for } z > z' \quad (25)$$

$$\underline{z}_0 = \hat{z}_0 \quad (26)$$

$$\underline{m}_e = \nabla_t \phi_e \times \hat{z} \quad (27)$$

$$\underline{n}_0 = \nabla_t \phi_0 \quad (28)$$

$$\epsilon_0 = \text{Sink}_x \text{Sink}_y \quad (29)$$

$$\phi_e = \text{Cosk}_x \text{Cosk}_y \quad (30)$$

$$k_x = \frac{m\pi}{a}, \quad k_y = \frac{n\pi}{b}, \quad k_z = \frac{\lambda\pi}{c}, \quad \lambda, m, n = 0, 1, 2, \dots \quad (31a)$$

$$k_0 = (k^2 - k_x^2 - k_y^2 - k_z^2)^{1/2} \quad (31b)$$

$$k_g = (k^2 - k_y^2)^{1/2} \quad (31c)$$

$$\delta_0 = \begin{cases} 1 & \text{if } \lambda \text{ or } m \text{ or } n = 0 \\ 0 & \text{if } \lambda, m, n \neq 0 \end{cases} \quad (32)$$

The expression by Rahmat-Samii [12] had an error in sign resulting from a misprint. After correction, his expression reads, in terms of the $e^{j\omega t}$ convention chosen,

$$\underline{G}_R^e = -\frac{1}{k^2} \underline{I} \delta(|\underline{r}-\underline{r}'|) - \frac{1}{k^2} \sum_{n=0}^{\infty} \sum_{m=0}^{\infty} \sum_{\ell=0}^{\infty} \frac{\epsilon_{on} \epsilon_{om} \epsilon_{o\ell}}{abc \left[k^2 - \left(\frac{n\pi}{a} \right)^2 - \left(\frac{m\pi}{b} \right)^2 - \left(\frac{\ell\pi}{c} \right)^2 \right]} \left\{ \left[\left(\frac{m\pi}{b} \right)^2 + \left(\frac{\ell\pi}{c} \right)^2 \right] \text{Cos} \frac{n\pi x}{a} \text{Cos} \frac{n\pi x'}{a} \text{Sin} \frac{m\pi y}{b} \text{Sin} \frac{m\pi y'}{b} \right.$$

$$\begin{aligned}
& - \frac{m' m}{a b} \cos \frac{m' x}{a} \sin \frac{m x}{a} \sin \frac{m' y}{b} \cos \frac{m y}{b} \sin \frac{m' z}{c} \sin \frac{m z}{c} \\
& - \frac{m' m}{b a} \sin \frac{m' x}{a} \cos \frac{m x}{a} \cos \frac{m' y}{b} \sin \frac{m y}{b} \sin \frac{m' z}{c} \sin \frac{m z}{c} \\
& - \frac{m' m}{c a} \sin \frac{m' x}{a} \sin \frac{m x}{a} \cos \frac{m' y}{b} \cos \frac{m y}{b} \sin \frac{m' z}{c} \cos \frac{m z}{c} \\
& - \frac{m' m}{c b} \sin \frac{m' x}{a} \sin \frac{m x}{a} \sin \frac{m' y}{b} \cos \frac{m y}{b} \sin \frac{m' z}{c} \cos \frac{m z}{c} \\
& - \frac{m' m}{c a} \sin \frac{m' x}{a} \sin \frac{m x}{a} \sin \frac{m' y}{b} \sin \frac{m y}{b} \cos \frac{m' z}{c} \sin \frac{m z}{c} \\
& - \frac{m' m}{c b} \sin \frac{m' x}{a} \sin \frac{m x}{a} \sin \frac{m' y}{b} \sin \frac{m y}{b} \cos \frac{m' z}{c} \cos \frac{m z}{c} \\
& - \frac{m' m}{c a} \sin \frac{m' x}{a} \sin \frac{m x}{a} \cos \frac{m' y}{b} \sin \frac{m y}{b} \cos \frac{m' z}{c} \sin \frac{m z}{c} \\
& - \frac{m' m}{c b} \sin \frac{m' x}{a} \sin \frac{m x}{a} \cos \frac{m' y}{b} \sin \frac{m y}{b} \cos \frac{m' z}{c} \cos \frac{m z}{c} \\
& - \frac{m' m}{c a} \sin \frac{m' x}{a} \sin \frac{m x}{a} \sin \frac{m' y}{b} \cos \frac{m y}{b} \sin \frac{m' z}{c} \sin \frac{m z}{c} \\
& - \frac{m' m}{c b} \sin \frac{m' x}{a} \sin \frac{m x}{a} \sin \frac{m' y}{b} \cos \frac{m y}{b} \sin \frac{m' z}{c} \cos \frac{m z}{c} \\
& - \frac{m' m}{c a} \sin \frac{m' x}{a} \sin \frac{m x}{a} \sin \frac{m' y}{b} \sin \frac{m y}{b} \cos \frac{m' z}{c} \sin \frac{m z}{c} \\
& - \frac{m' m}{c b} \sin \frac{m' x}{a} \sin \frac{m x}{a} \sin \frac{m' y}{b} \sin \frac{m y}{b} \cos \frac{m' z}{c} \cos \frac{m z}{c}
\end{aligned}$$

since a and a' are exchanged between the notations in Equations (22) and Equation (24). The conclusion was that the term involving the Dirac-delta function was $-\frac{1}{2} \delta(z)$ in Equation (22) of Tai and Rozenfeld, but was $-\frac{1}{2} \delta(z)$ in Rahmat-Samii's expression of Equation (33). We will show that Equation (22) is identical to Equation (33) and therefore no discrepancy exists. We begin with Equation (24) of Tai and Rozenfeld [11] as follows:

$$\begin{aligned}
G_z^t &= \sum_{m, n} \frac{C}{K^2 - k^2} \{ m m' e^{-m' z} \sin k_z z \sin k_z z' \\
&+ \frac{m m'}{2} \sin k_z z \sin k_z z' \}
\end{aligned}$$

$$\begin{aligned}
& + \frac{k_c^2(k^2 - k_z^2)}{k^2} \frac{\xi \xi'}{\xi_0 \xi_0'} \cos k_z z \cos k_z z' \\
& - \frac{k_z k_c^2}{k^2} \frac{\xi \eta'}{\xi_0 \xi_0'} \cos k_z z \sin k_z z' \\
& + \frac{\eta \xi'}{\xi_0 \xi_0'} \sin k_z z \cos k_z z' \Big] , \tag{35}
\end{aligned}$$

where

$$k^2 = k_x^2 + k_y^2 + k_z^2 \tag{36}$$

Substitution of Equations (23-32) into Equation (35) yields

$$\begin{aligned}
G_{T}^e = & - \frac{1}{k^2} \sum_{n=0}^{\infty} \sum_{m=0}^{\infty} \sum_{\ell=0}^{\infty} \frac{4(2-\delta_0)}{abc[k^2 - k^2]} \\
& \left\{ \begin{aligned}
& \ddot{xx}(k^2 - k_x^2) \cos k_x x \cos k_x x' \sin k_y y \sin k_y y' \sin k_z z \sin k_z z' \\
& + \ddot{yy}(k^2 - k_y^2) \sin k_x x \sin k_x x' \cos k_y y \cos k_y y' \sin k_z z \sin k_z z' \\
& + \ddot{zz}(k^2 - k_z^2) \sin k_x x \sin k_x x' \sin k_y y \sin k_y y' \cos k_z z \cos k_z z' \\
& + \ddot{xy}(-k_x k_y) \cos k_x x \sin k_x x' \sin k_y y \cos k_y y' \sin k_z z \sin k_z z' \\
& + \ddot{yx}(-k_x k_y) \sin k_x x \cos k_x x' \cos k_y y \sin k_y y' \sin k_z z \sin k_z z' \\
& + \ddot{yz}(-k_y k_z) \sin k_x x \sin k_x x' \cos k_y y \sin k_y y' \sin k_z z \cos k_z z' \\
& + \ddot{zy}(-k_z k_y) \sin k_x x \sin k_x x' \sin k_y y \cos k_y y' \cos k_z z \sin k_z z' \\
& + \ddot{xz}(-k_x k_z) \cos k_x x \sin k_x x' \sin k_y y \sin k_y y' \sin k_z z \cos k_z z' \\
& + \ddot{zx}(-k_z k_x) \sin k_x x \cos k_x x' \sin k_y y \sin k_y y' \cos k_z z \sin k_z z' \Big\} . \tag{37}
\end{aligned} \right.
\end{aligned}$$

$$= \frac{1}{k^2} \sum_{n=0}^{\infty} \sum_{m=0}^{\infty} \sum_{l=0}^{\infty} \frac{4(2-\delta_0)}{abc[k^2 - k'^2]} (k^2 - k'^2) \cos k_x x \cos k_x x' \cos k_y y \cos k_y y' \cos k_z z \cos k_z z'$$

$$\cos k_x x \cos k_x x' \cos k_y y \cos k_y y' \cos k_z z \cos k_z z'$$

$$= -\frac{1}{k^2} \delta(|\underline{r}-\underline{r}'|) - \frac{1}{k^2} \sum_{n=0}^{\infty} \sum_{m=0}^{\infty} \sum_{l=0}^{\infty} \frac{4(2-\delta_0)}{abc} \frac{k_y^2 + k_z^2}{k^2 - k'^2}$$

$$\cos k_x x \cos k_x x' \cos k_y y \cos k_y y' \cos k_z z \cos k_z z' \quad (38)$$

$$= \frac{1}{k^2} \sum_{n=0}^{\infty} \sum_{m=0}^{\infty} \sum_{l=0}^{\infty} \frac{4(2-\delta_0)}{abc[k^2 - k'^2]} (k^2 - k'^2) \sin k_x x \sin k_x x'$$

$$\cos k_y y \cos k_y y' \cos k_z z \cos k_z z'$$

$$= -\frac{1}{k^2} \delta(|\underline{r}-\underline{r}'|) - \frac{1}{k^2} \sum_{n=0}^{\infty} \sum_{m=0}^{\infty} \sum_{l=0}^{\infty} \frac{4(2-\delta_0)}{abc} \frac{k_x^2 + k_z^2}{k^2 - k'^2}$$

$$\sin k_x x \sin k_x x' \cos k_y y \cos k_y y' \cos k_z z \cos k_z z' \quad (39)$$

$$= \frac{1}{k^2} \sum_{n=0}^{\infty} \sum_{m=0}^{\infty} \sum_{l=0}^{\infty} \frac{4(2-\delta_0)}{abc[k^2 - k'^2]} (k^2 - k'^2) \sin k_x x \sin k_x x' \sin k_y y \sin k_y y'$$

$$\cos k_z z \cos k_z z' = -\frac{1}{k^2} \delta(|\underline{r}-\underline{r}'|) - \frac{1}{k^2} \sum_{n=0}^{\infty} \sum_{m=0}^{\infty} \sum_{l=0}^{\infty} \frac{4(2-\delta_0)}{abc}$$

$$\frac{k_x^2 + k_y^2}{k^2 - k'^2} \sin k_x x \sin k_x x' \sin k_y y \sin k_y y' \cos k_z z \cos k_z z' \quad (40)$$

Substitution of Equations (38-40) into Equation (37) yields an expression of \underline{G}_T^e identical to \underline{G}_R^e of Equation (33), with the understanding that m and n are exchanged and that

$$4(2-\delta_o) = \epsilon_{on}\epsilon_{om}\epsilon_{ol} \quad (41)$$

if at least two of the three integers, m, n and l, are nonzeros (when two or more of them are zero, the series term is zero). We can also prove directly that Equations (22) and (33) are identical either by substituting only Equation (40) into Equation (37) or by using Equations (38), (39) and the following relations

$$\begin{aligned} \sum_{z=0}^{\infty} \frac{1}{K^2 - k^2} \text{Sink}_z z \text{Sink}_z z' \\ = \frac{c}{2k_g \text{Sink}_g c} \left\{ \begin{array}{l} \text{Sink}_g (c-z) \text{Sink}_g z' \\ \text{Sink}_g z \text{Sink}_g (c-z') \end{array} \right\} \quad z' > z \quad (42) \end{aligned}$$

$$\begin{aligned} \sum_{z=0}^{\infty} \frac{\epsilon_{ol}}{K^2 - k^2} \text{Cosk}_z z \text{Cosk}_z z' \\ = \frac{-c}{k_g \text{Sink}_g c} \left\{ \begin{array}{l} \text{Cosk}_g (c-z) \text{Cosk}_g z' \\ \text{Cosk}_g z \text{Cosk}_g (c-z') \end{array} \right\} \quad z' > z \quad (43) \end{aligned}$$

$$\begin{aligned} \sum_{z=0}^{\infty} \frac{k_z}{K^2 - k^2} \text{Sink}_z z \text{Cosk}_z z' \\ = \frac{-c}{2\text{Sink}_g c} \left\{ \begin{array}{l} \text{Sin}(c-z) \text{Cosk}_g z' \\ -\text{Sink}_g z \text{Cosk}_g (c-z') \end{array} \right\} \quad z' > z \quad (44) \end{aligned}$$

and

$$\begin{aligned} \sum_{z=0}^{\infty} \frac{k_z}{K^2 - k^2} \text{Cosk}_z z \text{Sink}_z z' \\ = \frac{c}{2\text{Sink}_g c} \left\{ \begin{array}{l} -\text{Cosk}_g (c-z) \text{Sink}_g z' \\ \text{Cosk}_g z \text{Sin}(c-z') \end{array} \right\} \quad z' > z \quad (45) \end{aligned}$$

which were originally employed by Tai and Rozenfeld and can be directly derived from well known identities [20, p. 581]. This finding that the expressions of Rahmat-Samii and Tai and Rozenfeld are identical, even though they appear in different forms, has also been observed by Professor Tai [21]. For a more detailed description of the proof, the reader is referred to an earlier interim report [28].

SECTION III

COMPACT RANGE SCATTERING MEASUREMENTS

Compact Range Scattering Measurements Technique [29]: There has been an increasing amount of interest in the compact range for antenna and scattering measurements. The compact range technique was first implemented in X and Ku bands [29], and was recently extended to 30 GHz [30]. At frequencies below 2 GHz, a number of technical difficulties have long been generally recognized. Major obstacles include the edge diffraction of the reflector, multipaths of the illuminating wave, and precision of the instrumentation. These difficulties have been overcome and compact range RCS measurements were extended to as low as 1 GHz.

The cancellation method [31] was employed in the scattering measurement. Figure 3 shows a block diagram illustrating the principle of the set up and Figure 4 shows the physical arrangement of the cancellation network. The use of high-precision microwave components and heavy 1.4 inch semi-rigid cable is essential to obtain a deep null insensitive to temperature variations and vibration. Even the 1.4 inch semi-rigid cable was sometimes found to be sensitive to vibration and had to be fastened to the mounting structure with a damping mechanism. The network was mounted on a plexiglass board which was seated on a layer of foam as shown in Figure 4. Other shock-mounting devices were also placed below the tables, the receivers, the transmitter, the frequency "lock-box", etc. A 1-4 GHz solid-state cavity-tuned source with an output power of 20 to 200 mw was built for the measurement system. When connected with a lock-box, a frequency stability of 1 part in 10^6 was maintained. The dual-channel phase and amplitude receiving system is shown in Figure 5.

The compact range used in this study consists of a 12-foot high by 16-foot wide reflector as shown in Figure 6. The reflector was fed by a 24 in. x 32 1/2 in. rectangular horn, shown in Figure 7, located at a focal distance of about 12 feet. Both the reflector and horns are fabricated by standard methods with average mechanical tolerances. Figure 8 shows a styrofoam support for the target under test.

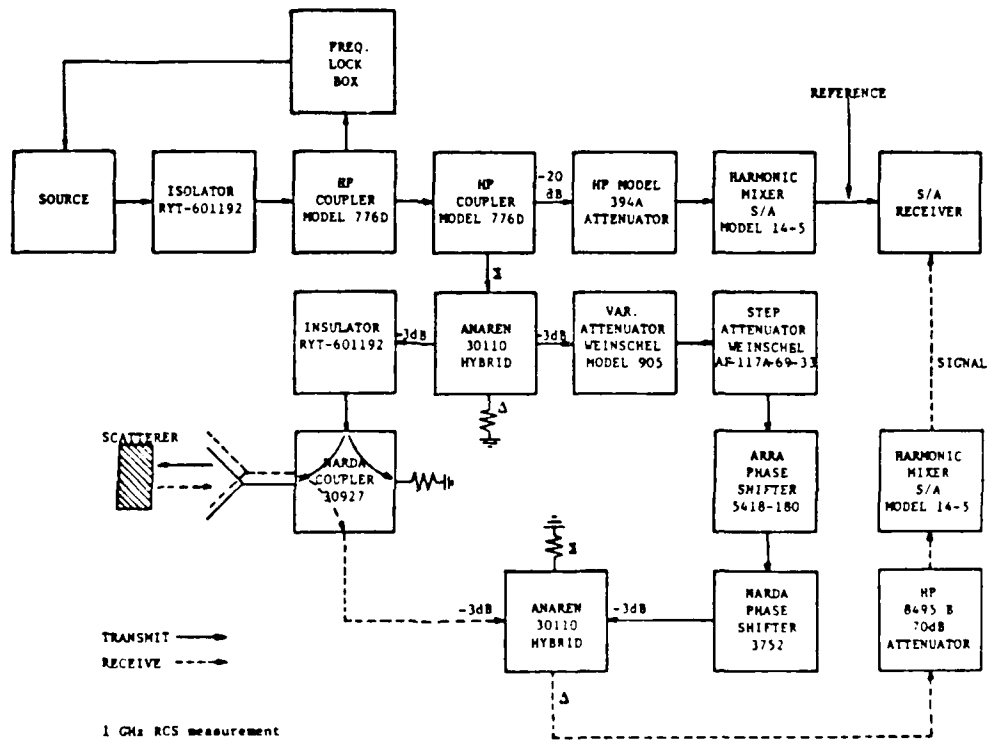


Figure 3. Block diagram for 1 GHz compact range RCS measurement.

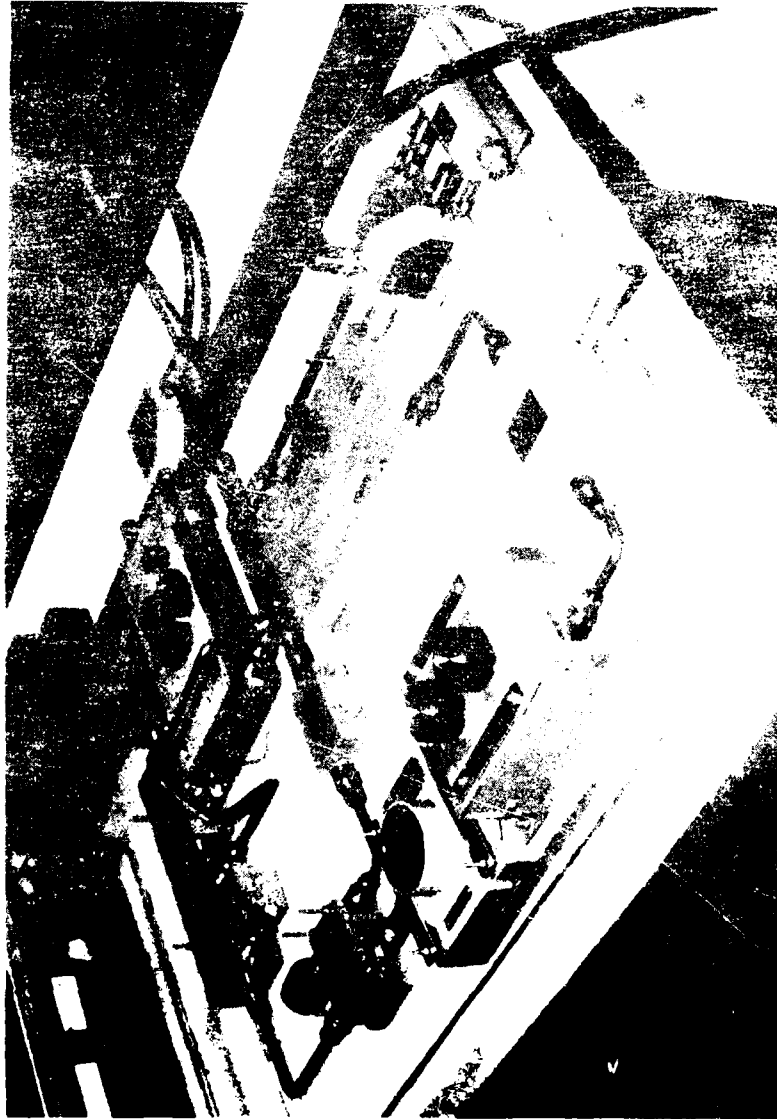


Figure 4. The arrangement of the shock-mounted cancellative network used in the 1 GHz scattering measurements.

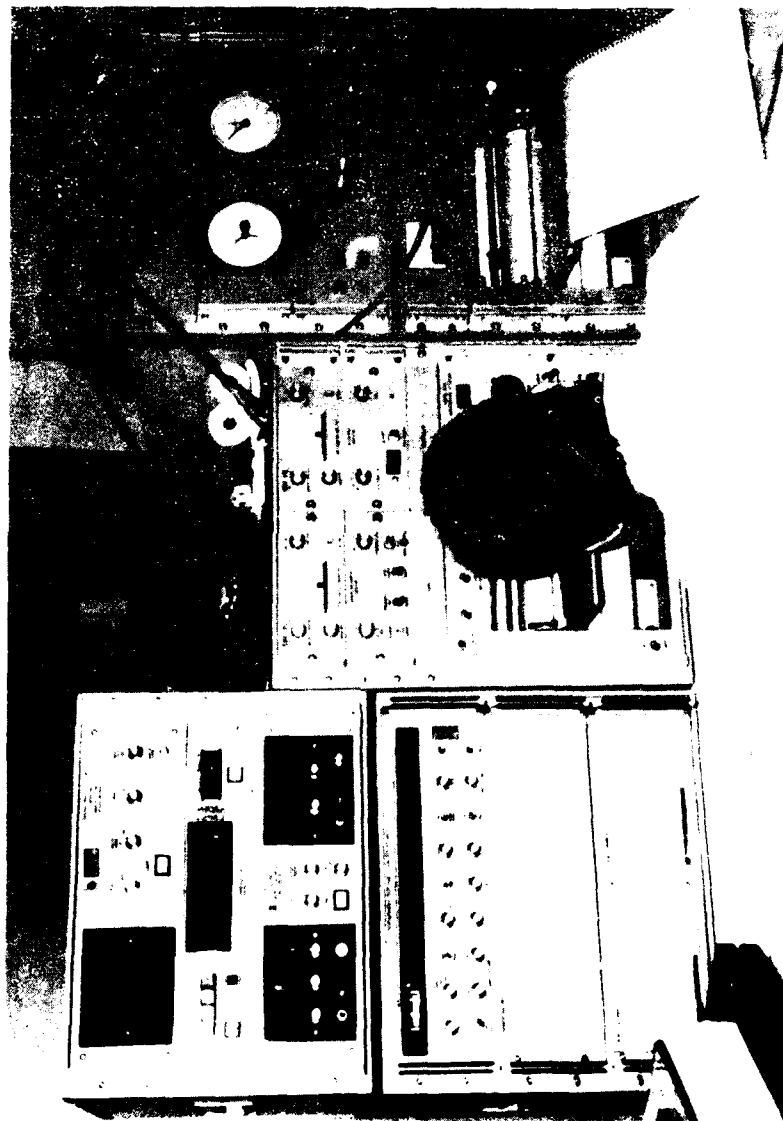


Figure 5. The dual-channel receiving system used in the compact range measurement.



Figure 9. Partial view of the 1-foot high, 16-foot wide reflector used in the compact range.

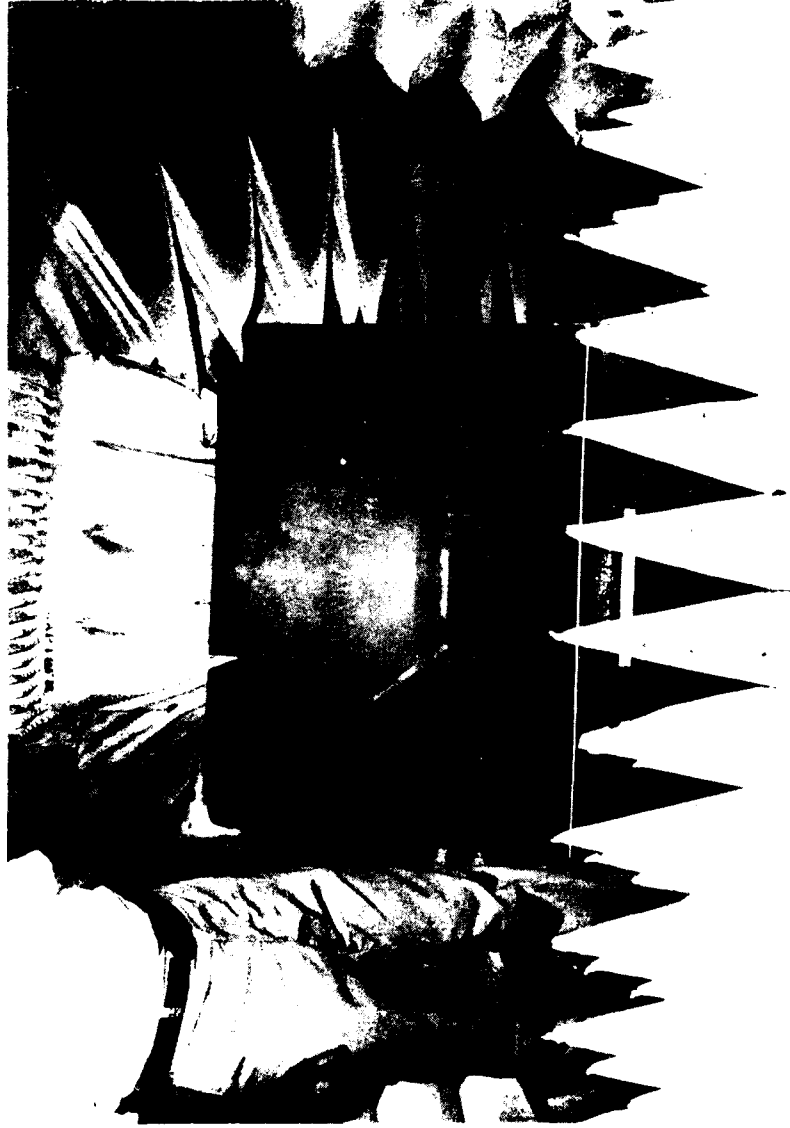


Figure 7. The rectangular horn with a 24 in. x 32 1/2 in. aperture used as a feed for the reflector in the compact range.

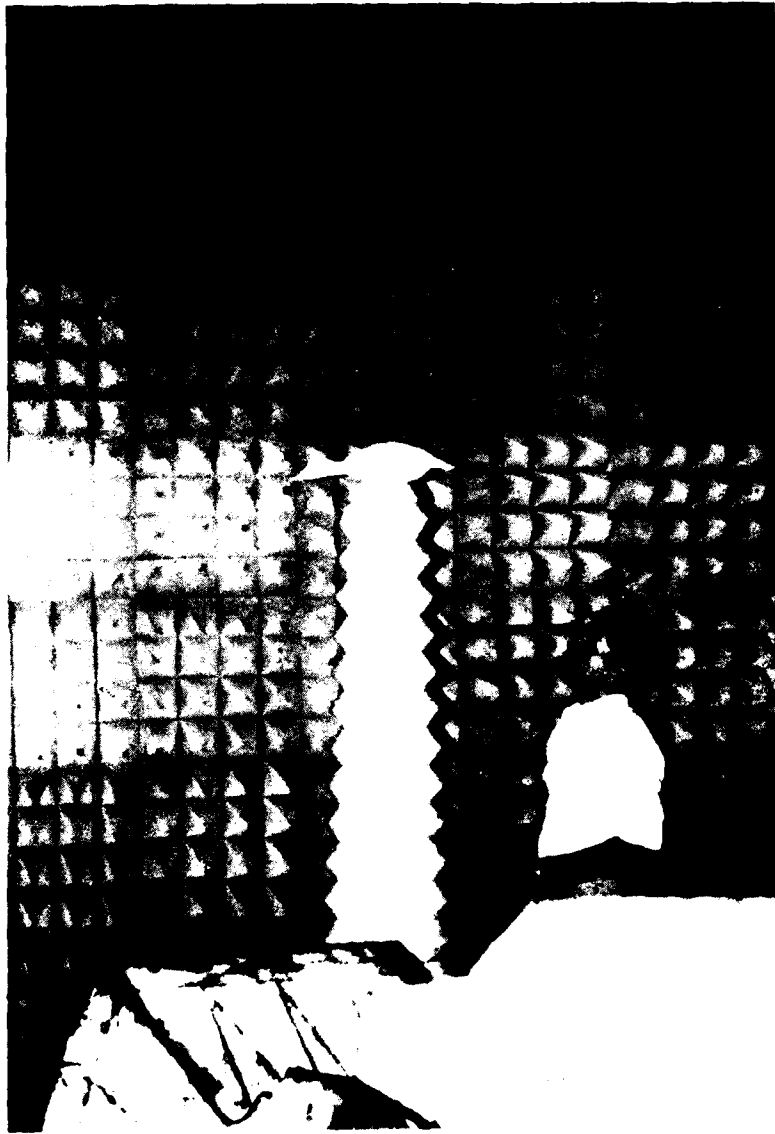


Figure 8. Styrofoam support for the scattering target used in the compact range.

At 1 GHz and lower, the multipath propagation, leakage and parasitic excitation along the source, cable and the components and equipments can cause severe difficulty. In fact, leakage from the source was initially found to be only 30 dB below the illuminating field in the quiet zone. These problems were overcome through careful shielding and the use of microwave absorbers.

The field in the quiet zone was probed with a dipole, and amplitude variations of less than ± 1 dB and phase variations less than ± 5 degrees over an area of 5 ft. x 3 ft. were achieved. Since the horn used is an ordinary rectangular horn, further improvement in the quiet zone illumination may be achievable by using low-side-lobe feeds such as a corrugated horn.

The ultimate criterion for the radar cross-section range using the cancellation method is the stability and depth of the null achievable. The deeper the null, the smaller echo return the system can detect. Also a stable null insures accurate and consistent measurements. To achieve stability and depth for the null, sufficiently high power and frequency stability of the source are essential. The sensitivity of the receiver is usually sufficient since the environmental noise in the range is usually quite high. In the 1 GHz measurements, we were able to obtain a null depth of -50 dBSM during the day and -60 dBSM in the night, which could be maintained for an average duration of 1.5 to 2 minutes.

The sensitivity of the compact range is displayed by measurements shown in Table I on small conducting spheres shown in Figure 9 whose echo areas are accurately known. The close agreement shows that accurate measurements can be made for small scatterers with low echo return. Figure 10a and 10b show measurements on a circular cylinder 2.76 wavelengths long for E and H plane aspect angles. Figure 11a and 11b show the measured data for flat conducting plates. Figures 12a and 12b show the measured data for rectangular conducting boxes. All these measurements are in good agreement with data in the literature, as can be seen in Figures 9 through 12. However, there is some confusion in the literature concerning the polarization of the data which remains to be clarified.

TABLE I
COMPARISON BETWEEN COMPACT RANGE MEASUREMENT
AND EXACT CALCULATIONS FOR CONDUCTING SPHERES
CALIBRATED WITH THE 0.04403λ SPHERE

Radius in Wavelengths	RCS in dBsm	
	Theoretical	Measured
.04403	-46.14	-46.1
.05503	-40.41	-40.4
.06054	-37.63	-37.6
.06604	-35.45	-35.5
.07154	-33.42	-33.4
.07705	-31.80	-31.8
.10456	-25.44	-25.4
.11010	-22.82	-22.8

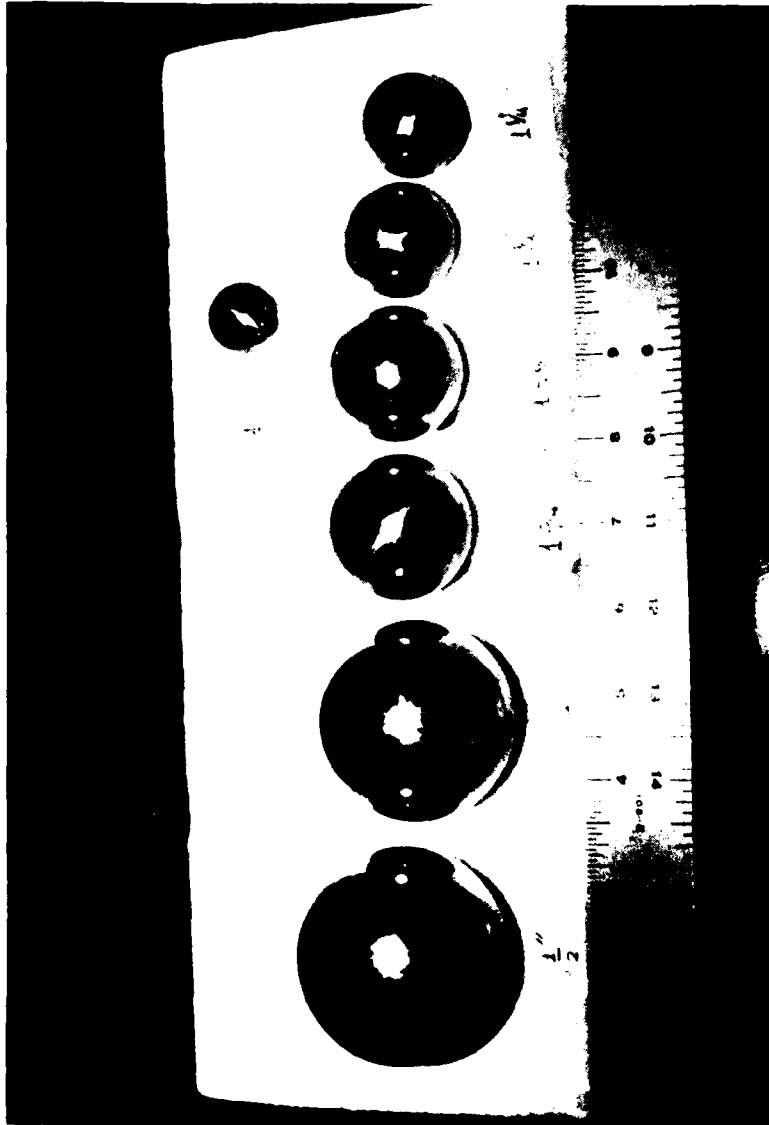
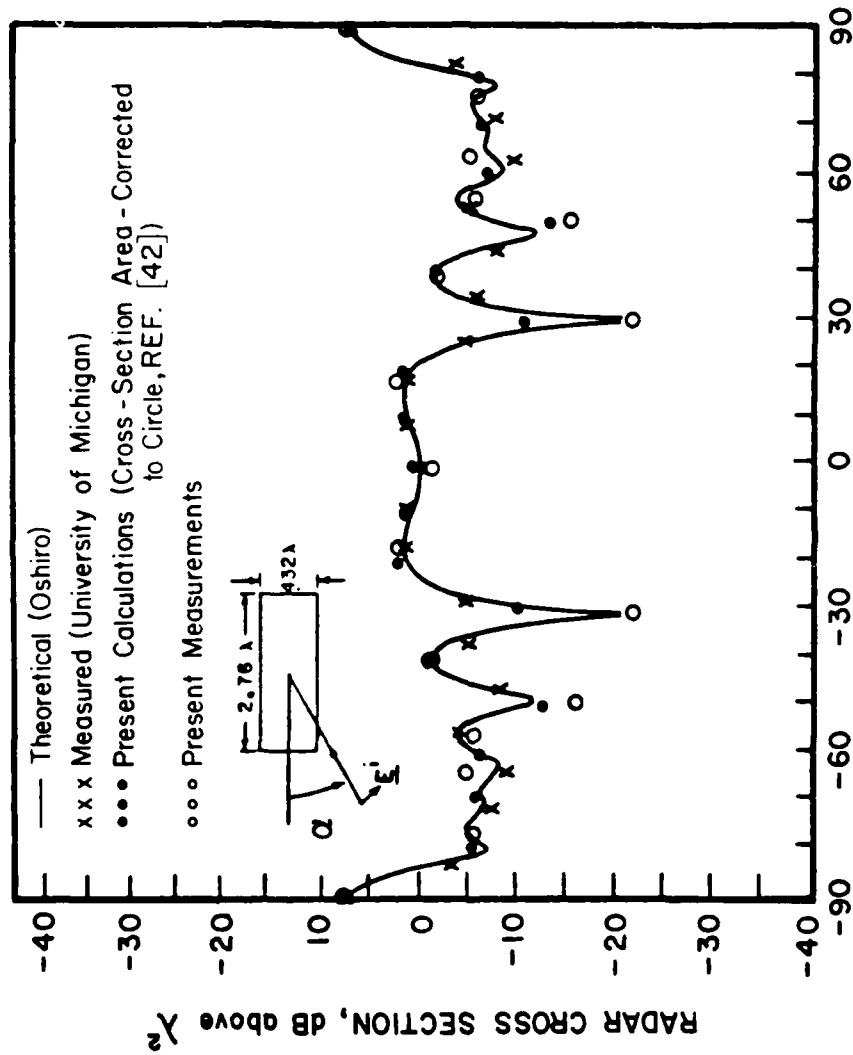


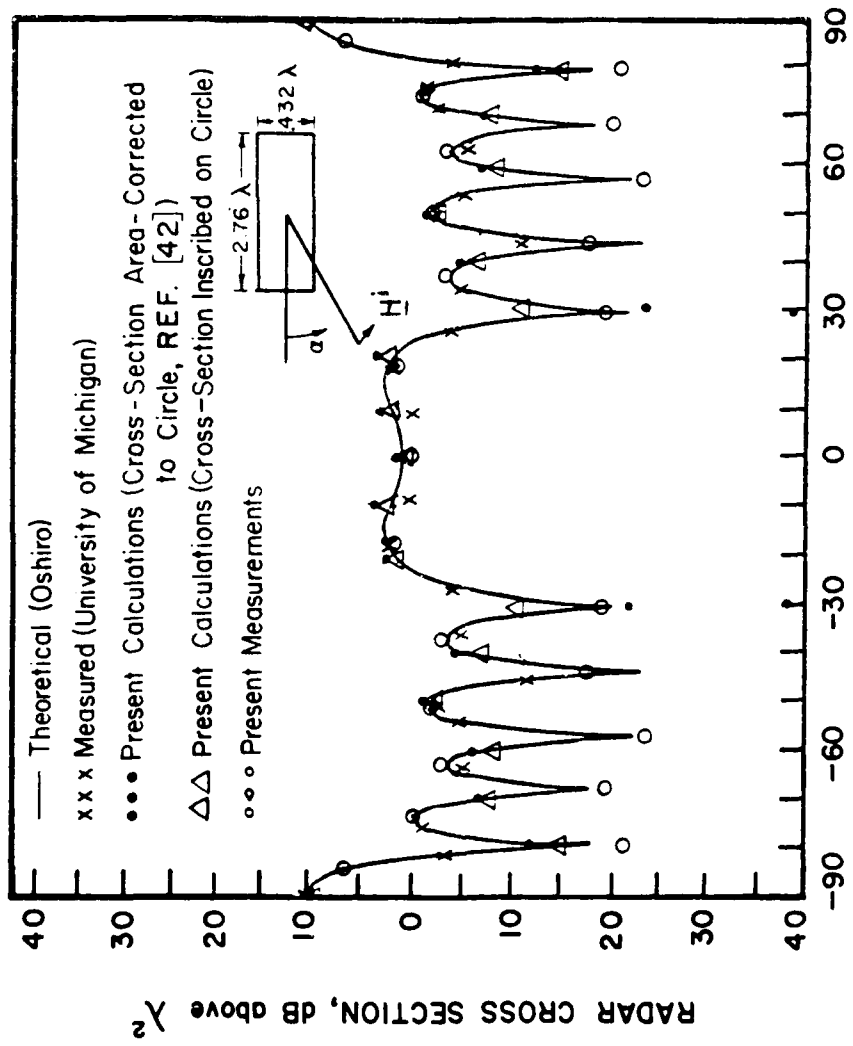
Figure 9. Stainless-steel spheres used in the calibration of the scattering measurement.



E - PLANE ASPECT ANGLE α (DEGREES)

a) E-plane pattern

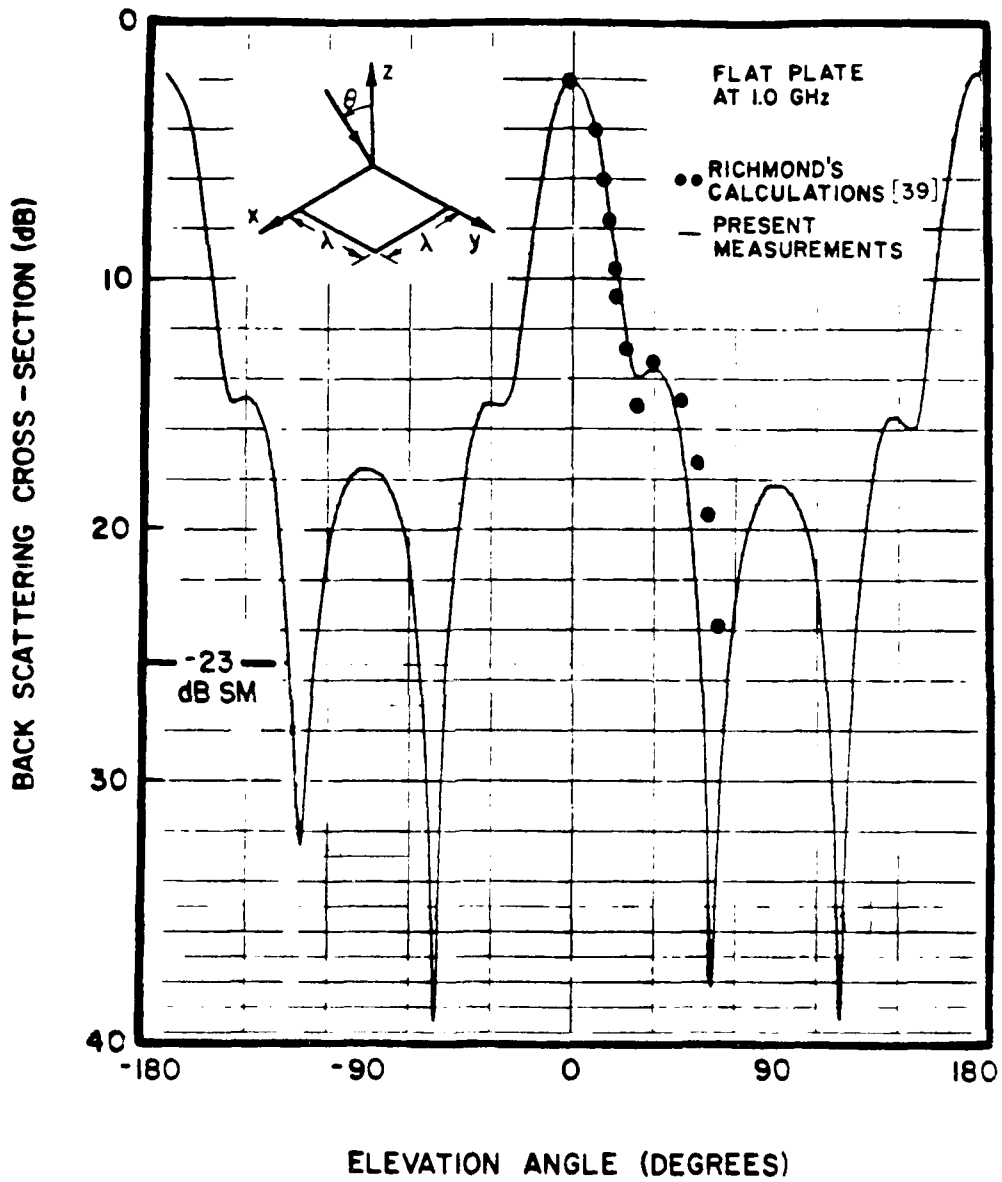
Figure 10. Comparison between compact range measurements and other known data for a finite circular cylinder (continued).



H-PLANE ASPECT ANGLE α (DEGREES)

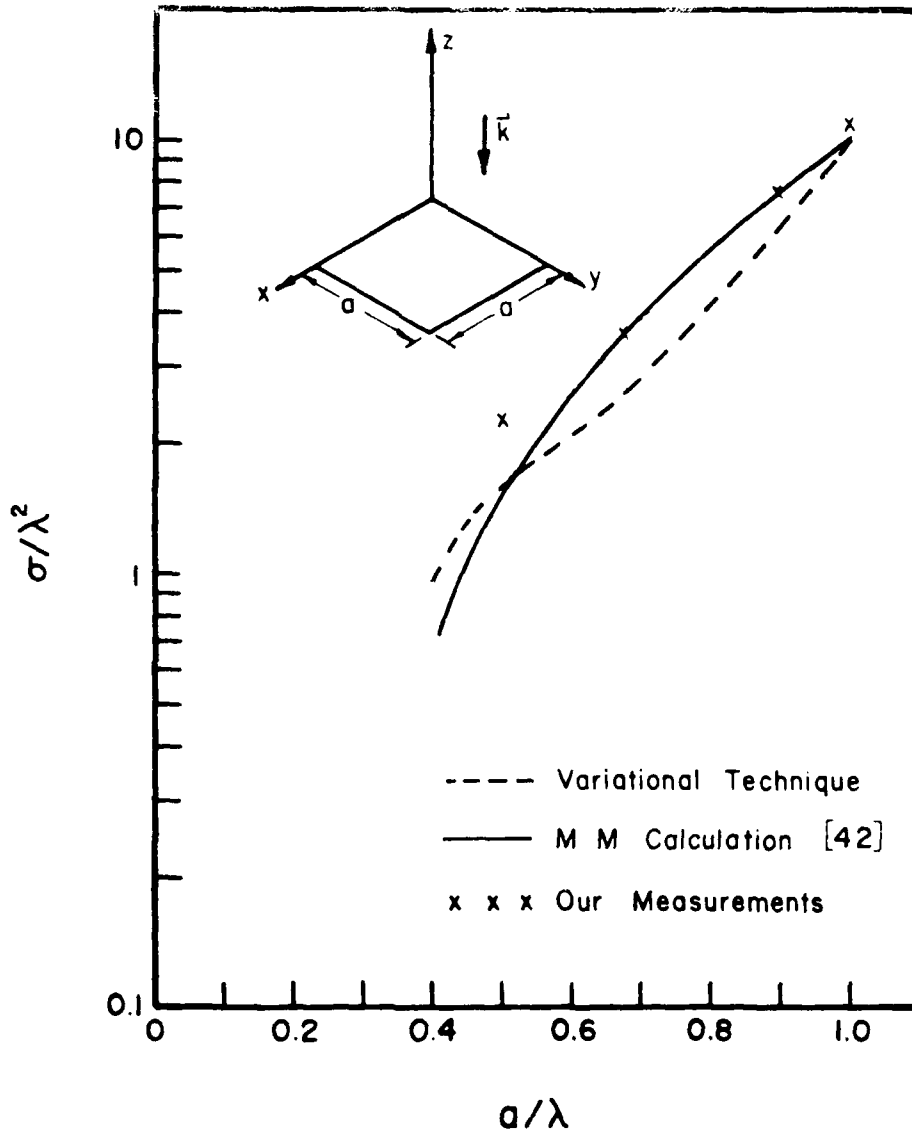
b) H-plane pattern

Figure 10. Comparison between compact range measurements and other known data for a finite circular cylinder.



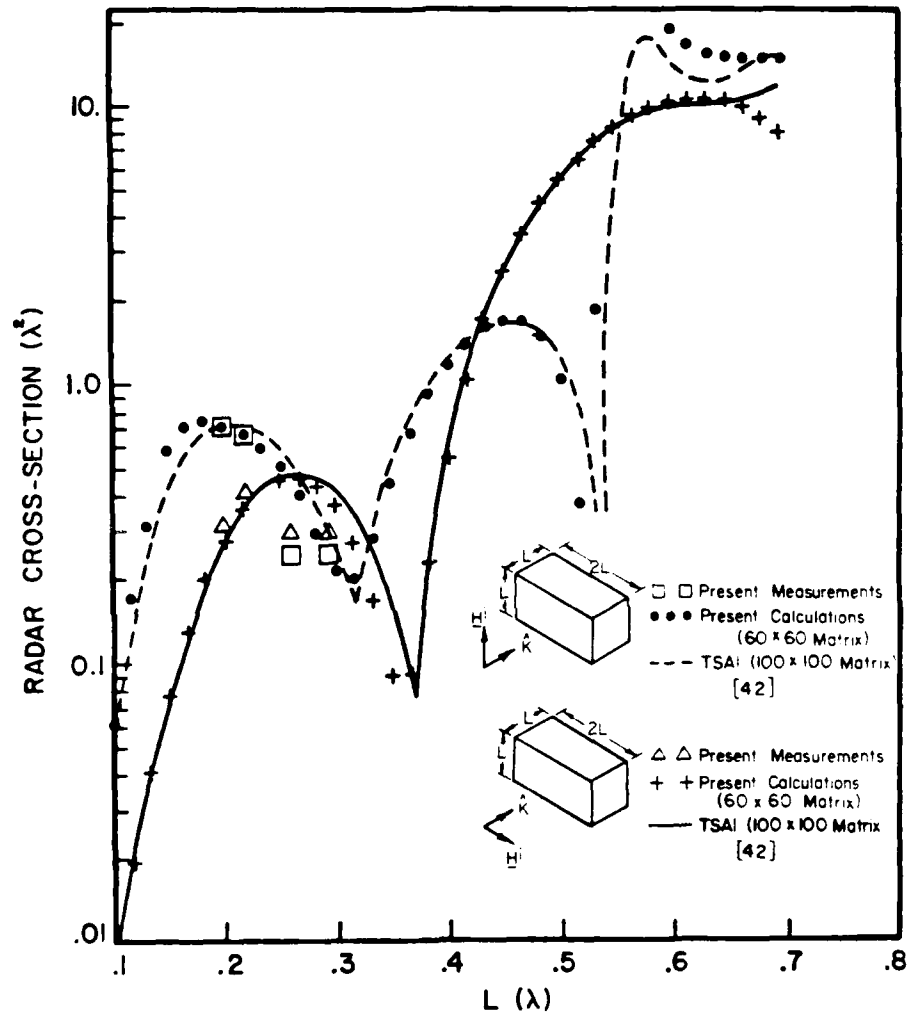
a) Backscattering pattern as a function of elevation angle.

Figure 11. Comparisons of measured and calculated backscattering cross-section of a square plate.



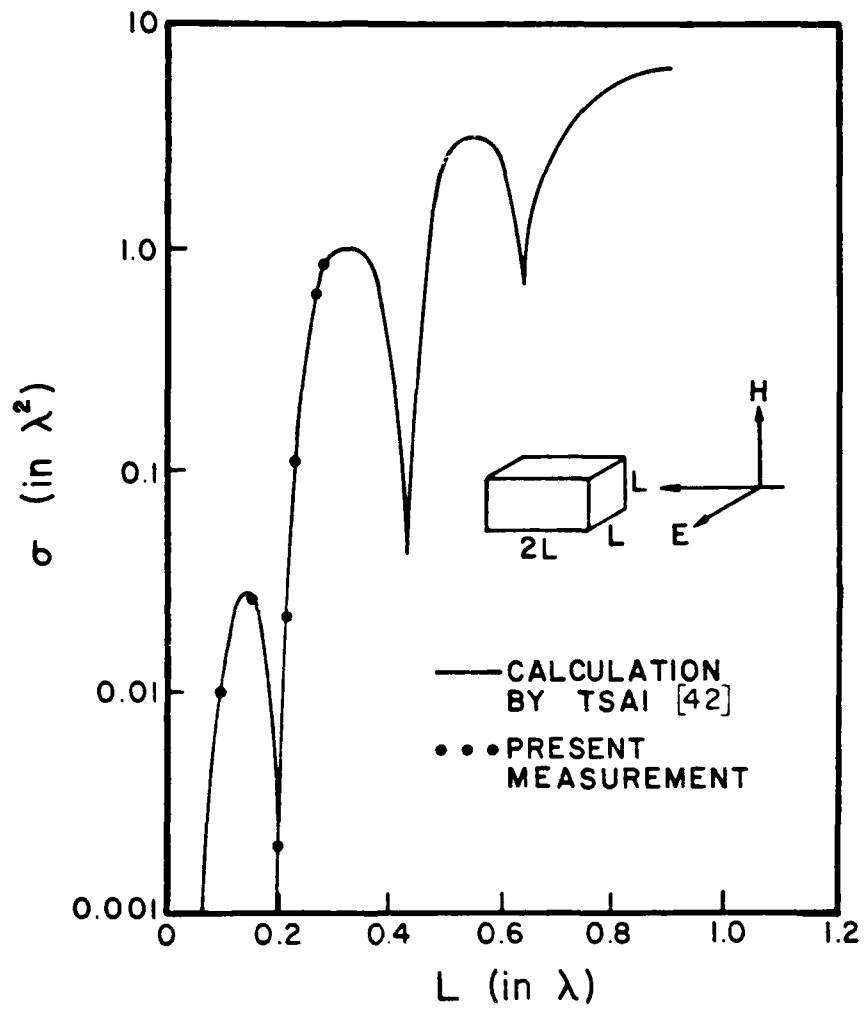
b) Backscattering cross-section as a function of plate size.

Figure 11. Comparisons of measured and calculated backscattering cross-section of a square plate.



a) Backscatter as a function of length as viewed from the side

Figure 12. Compact range scattering measurement of conducting boxes (continued).



b) Backscatter as a function of length as viewed from the end

Figure 12 . Compact range scattering measurement of conducting boxes.

4.1. Simulation of Biological Bodies

A major difficulty in measurements involving a biological body is the lack of consistency and stability. A living bird or animal undergoes physiological changes all the time. They may feed less today, and they may move during the tests. This difficulty can be very frustrating and the interested reader may consult reference 32 for methods considered by Blacksmith and Mack [33].

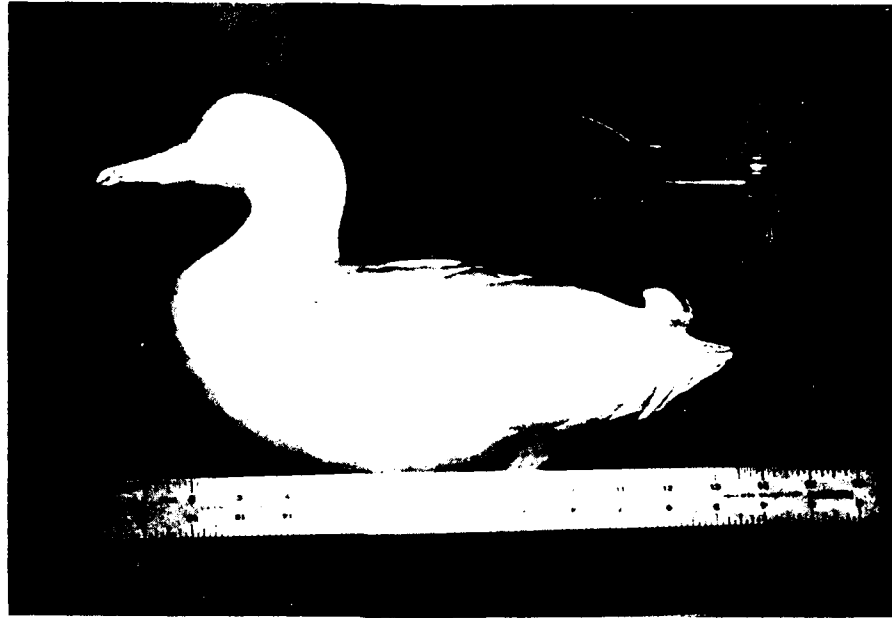
Since the physical configuration and the dielectric property are the only parameters involved in the scattering measurements, it is feasible to perform the test on a simulated model. While the simulation model removes the inconsistency and instability inherent in real biological bodies, there exists some degree of uncertainty as to how close the simulation can be realistically accomplished. For example, it is difficult to simulate the feathers, skin, blood vessels, etc. However, feathers and skin have low dielectric constants and can sometimes be conveniently ignored. The blood vessels have high water content but are usually surrounded by muscle tissues which also contain water.

Simulation techniques for biological bodies were developed by Guy [34], who employed various chemicals to simulate the complex dielectric constant of fat, bone, and muscle tissue. His method was used in the fabrication of bird models in this research program.

Before making the model, a styrofoam mold is constructed to hold and support the moist jellied "Super-stuff" plastic. The mold is derived from a bird model made of plaster of paris. Figure 13 shows the side and front views of a sitting bird model made of plaster of paris. Figure 14 shows the side and front views of a flying bird model made of plaster of paris. Figure 16 shows the side view of a "Super-stuff" simulated flying Green Wingtail, SB4, in a styrofoam holder.

The "Super-stuff" simulated muscle tissue is composed of the following materials

Saline solution (12g salt/liter)	76.5%	(by weight)
Powdered polyethylene	15.2%	
Super-stuff	8.4%	

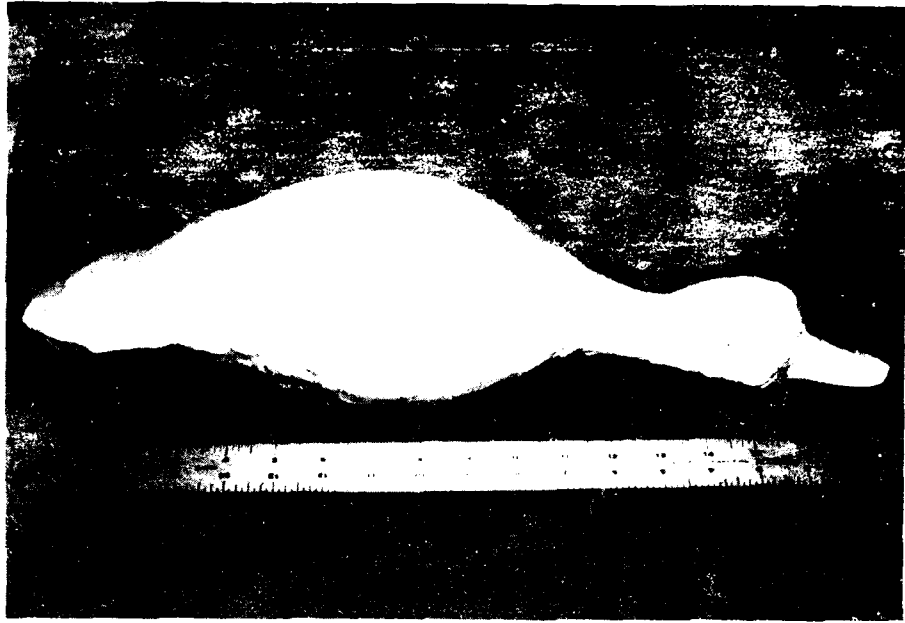


(a) Side view

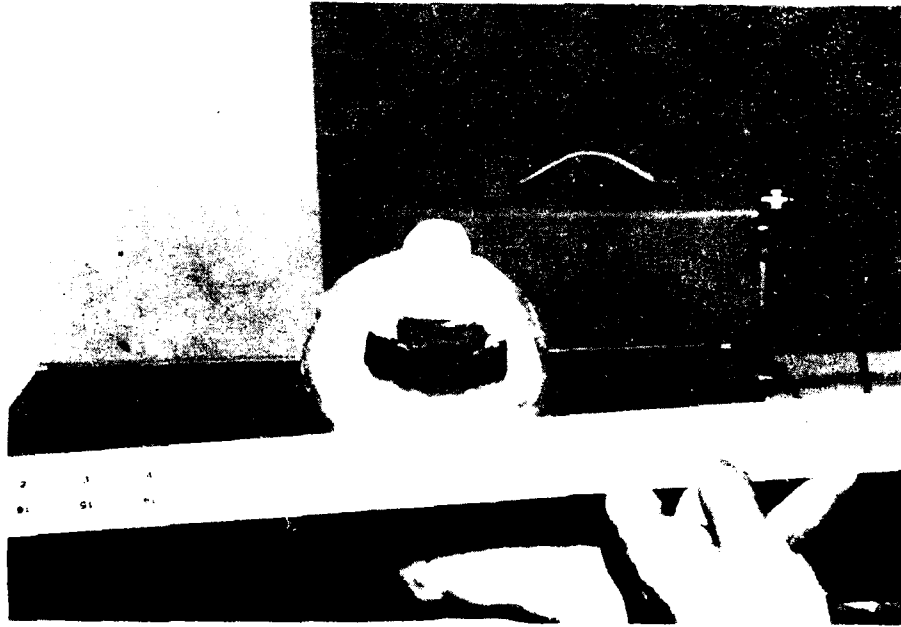


(b) Front view

Figure 13. Side and front views of a sitting bird made of plaster of paris.



(a) Side view



(b) Front view

Figure 14. Side and front views of a flying bird made of plaster of paris.



Figure 10. Side view of a "Super-stuff" simulated bird, SB4, in a styrofoam holder.

The "Super-stuff" is a jelling agent manufactured by Oil Center Research Corp. in Laffayette, Louisiana. The mixing process, which was improved here by trial and error, is critical to the homogeneity of the simulated tissue. Spectroscopic-grade salt is first added to deionized water in a blending mixer in an oven. After reaching 200°F the solution is stirred for about 2 minutes. Fine polyethylene powder is then slowly poured into the solution which is now being stirred at high speed. After half of the polyethelene powder is poured in, the rest of the powder is mixed with the super-stuff and poured into the solution being stirred at high speed. The temperature and stirring help to remove bubbles and attain homogeneity. The temperature is then raised to 450°F for two minutes and the mixture is then allowed to cool.

Although it is usually possible to make a simulation model to meet the required dimensions, it is not easy to obtain the required complex dielectric constant with high accuracy. In order to insure reasonable accuracy in the model, the in-vivo probe measurement technique [35] was used to determine the complex permittivity of the model. Ordinarily there is about 5 percent error in this dielectric constant measurement. In all the simulation models measured, the disagreements between the anticipated and measured complex permittivity were mostly within 5 percent of each other.

SECTION IV

NUMERICAL SOLUTIONS FOR VARIOUS DIELECTRIC SCATTERERS

An exact solution for three-dimensional dielectric scatterers in free space exists only for the sphere. For scatterers of arbitrary shapes, numerical analyses employing the volume integral equation have been conducted [6-7,36-38]. There are other numerical and approximate methods which are devoted to the estimates of SAR (Specific Absorption Rate) [38], which is the average power absorbed per unit weight of the biological body. However, there appears to be little research in the analysis of the scattering cross section of arbitrarily-shaped dielectric and biological bodies.

In this section we discuss the use of the volume integral equation to compute the scattering cross section of three-dimensional arbitrarily-shaped dielectric bodies including rectangular and I-shaped boxes, spheres, finite circular cylinders, and simulated birds.

The basic volume integral equation has been discussed in detail in Reference 6. The dielectric body can be replaced by an equivalent volume current \underline{J} such that

$$\underline{J} = j\omega(\epsilon - \epsilon_0) \underline{E} \quad (46)$$

where ω is the angular frequency, \underline{E} is the electric field, ϵ_0 and ϵ are the complex permittivity in free space and the dielectric body, respectively. The volume integral equation in terms of the unknown \underline{J} is

$$\oint_V G(\underline{r}, \underline{r}') \underline{J}(\underline{r}') dv - \frac{\epsilon + 2\epsilon_0}{3j\omega\epsilon_0(\epsilon - \epsilon_0)} \underline{J}(\underline{r}) = \underline{E}^i(\underline{r}), \quad (47)$$

where

$$G(\underline{r}, \underline{r}') = -j\omega\epsilon_0 \left(\underline{I} + \frac{\nabla\nabla}{k^2} \right) \frac{\exp(-jk|\underline{r}-\underline{r}'|)}{4\pi|\underline{r}-\underline{r}'|} .$$

$\underline{E}^i(\underline{r})$ = incident electric field intensity,

\oint_V = Principal volume integral excluding the singular point at $|\underline{r}-\underline{r}'|$

\underline{I} = unit dyad

The solution of Equation (47) can be carried out by the method of moments. The dielectric body, generally heterogeneous, is divided into rectangular box cells and the equivalent current is expanded into a series of pulse functions, each of which is uniform in one cell and vanishes outside the cell. The Dirac-delta function, defined at the center of each volume cell, is used as the weighting function. By taking a scalar product on both sides of equation (47) with a weighting function and integrating over V , we generate a system of linear equations which is then solved numerically on a computer. The scattering cross section is then computed in terms of the equivalent current \underline{J} by numerical integration.

Numerical computations have been conducted for dielectric and biological bodies of various shapes including cubes, cylinders, spheres, rectangular and I-shaped boxes, and simulated birds. Good agreements have been observed for the field distribution inside the dielectric body in comparison with the data from Michigan State University [6,36,37]. For scattering calculations, the only data available in the literature were for spheres and finite circular cylinders. The present calculation showed correctly the sharp resonance behavior of the back-scatter cross section as a function of frequency. But the frequencies of resonance were about 20 percent lower than those based on the Mie series computation. This discrepancy could be due to the reduced apparent size of the sphere in the simulation using rectangular cells. Agreement with the finite cylinder is good. These results are presented in detail as follows.

A. Scatterers of Simple Shapes

Figure 16 shows the calculated back-scatter cross section for a finite dielectric cylinder in comparison with the data from Richmond [39]. Figure 17 shows the geometry of a rectangular box of saline water and the way the volume cells are divided and numbered. The calculated field distribution is displayed in Tables 2a, 2b and 2c for the x-component, z-component and total field of the electric field intensity. They are in good agreement with Michigan State data [36]. Figure 18 shows the calculated back-scatter cross section of this rectangular box of saline water in comparison with the measured data obtained at the Georgia Tech compact range.

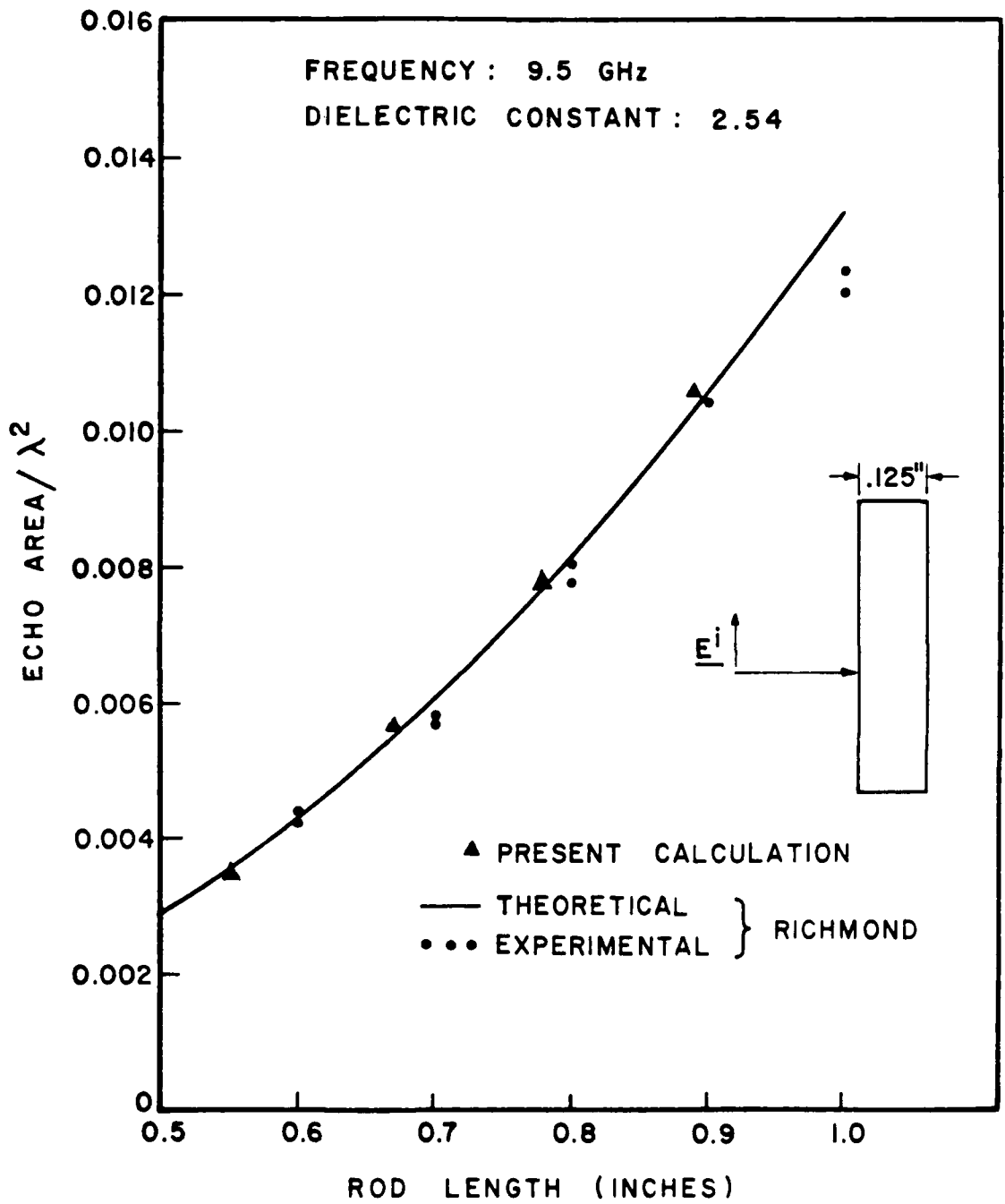


Figure 16. Comparison between the calculated results and Richmond's data for a dielectric cylinder.

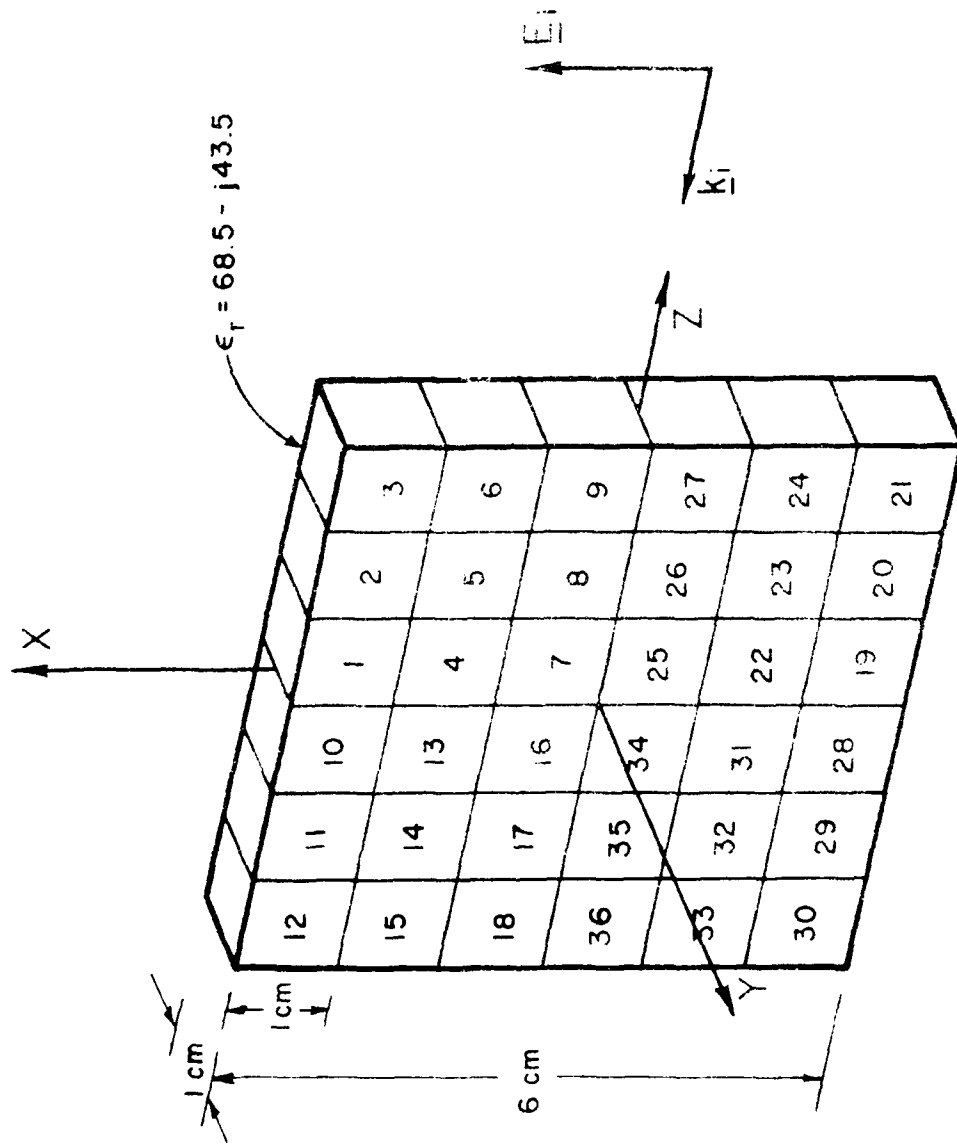


Figure 1. Rectangular box with a dielectric material and a plane wave excitation (numbers are the block numbers for the volume cells).

TABLE II
ELECTRIC FIELD DISTRIBUTION IN THE 36-CELL RECTANGULAR BLOCK

E_x - DISTRIBUTION IN THE 36-CELL
RECTANGULAR BLOCK

CELL NO.	PRESENT CALCULATION	MICHIGAN STATE	
		CALCULATED	MEASURED
1	.0510	.0518	.0518
2	.0600	.0573	.0523
3	.0952	.0976	.1632
4	.0816	.0862	.0862
5	.0883	.0827	.0832
6	.1040	.1090	.2355
7	.0870	.0935	.0935
8	.1225	.1180	.1180
9	.1355	.1410	.2869
10	.0292	.0339	.0459
11	.1008	.1050	.0878
12	.1611	.1570	.2017
13	.0930	.1020	.1258
14	.1956	.2020	.2020
15	.2546	.2480	.1256
16	.1345	.1460	.1460
17	.2267	.2330	.2330
18	.3294	.3220	.5410

TABLE II (Continued)

 E_z -DISTRIBUTION IN THE 36-CELL
RECTANGULAR BLOCK

CELL NO.	PRESENT CALCULATION	MICHIGAN STATE	
		CALCULATED	MEASURED
1	.2127	.2140	.2167
2	.1719	.1710	.1647
3	.1326	.1310	---
4	.0982	.0963	.0963
5	.0955	.0927	.0927
6	.0730	.0698	---
7	.0930	.0991	.0925
8	.0723	.0783	.0820
9	.0325	.0364	---
10	.2207	.2230	.2230
11	.1355	.1360	.1456
12	.0554	.0544	---
13	.0666	.0626	.0626
14	.0330	.0378	.0344
15	.0342	.0348	---
16	.0964	.1010	.1010
17	.0932	.0963	.0963
18	.0543	.0563	---

TABLE II (Continued)

E₁ - DISTRIBUTION IN THE 36-CELL
RECTANGULAR BLOCK

CELL NO.	PRESENT CALCULATION	MICHIGAN STATE	
		CALCULATED	MEASURED
1	.2187	.2202	---
2	.1821	.1803	---
3	.1633	.1633	---
4	.1277	.1292	---
5	.1301	.1242	---
6	.1271	.1294	---
7	.1274	.1362	---
8	.1422	.1416	---
9	.1394	.1456	---
10	.2226	.2256	---
11	.1689	.1718	---
12	.1703	.1662	---
13	.1144	.1137	---
14	.1984	.2047	---
15	.2569	.2505	---
16	.1655	.1775	---
17	.2451	.2521	---
18	.3339	.3269	---

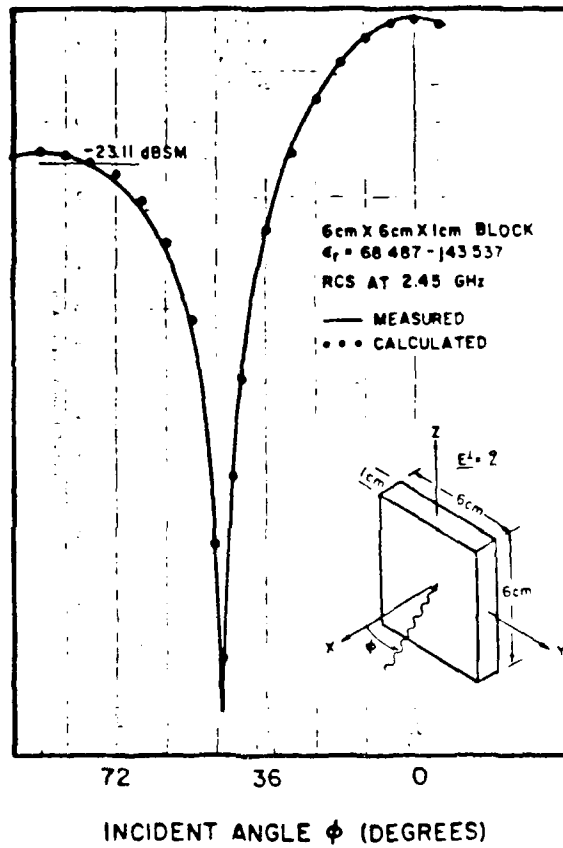


Figure 18. Comparison between calculated and measured RCS of square boxes of saline water shown in Figure 18.

Figure 19 shows an I-shaped box of saline water under plane wave excitation. The numbers are the index number for the volume cells. Tables 11(a), 11(b) and 11(c) show the calculated x , y and total z fields inside the I-shaped box of saline water. The agreements between the present calculation and that at Michigan State University [36] are good. Figure 20 shows the comparison between the measured and calculated back-scatter cross section data generated at Georgia Tech. The disagreement could be partially due to the acrylic box as indicated in the figure. Good agreements with Michigan State data were observed also for three other cases, including a cube and two rectangular cylinders, which will not be presented here.

Computations were also made for the dielectric sphere. Figure 21 shows the back-scatter cross section of a dielectric sphere with a relative permittivity of 2.592. The results deteriorate as Ka becomes greater than 1. Figures 22 and 23 show the computed results for a dielectric sphere with a complex dielectric constant of $29.43 - j0.158$ using 128-cell and 256-cell, respectively. The results are rather disappointing when compared with data generated by Burr and Lo [40], as shown in Figures 22 and 23. The resonance frequencies were shifted by 20 percent and the resonance peaks are off by 30 percent. This failure in predicting resonance phenomena in a dielectric sphere by the volume integral equation approach is in contrast to the high accuracy achieved for the calculation of conducting spheres by a surface integral equation approach [41,42].

The results for the sphere were presented in the 1980 IEEE AP-S Symposium. Both Professors Chen and Nyquist of the Michigan State University attended the meeting and commented that they had also observed similar difficulties with the sphere. They have further noticed that if the incident field $\exp(-jkr)$ is decomposed into a sine and cosine terms, the solution corresponding to one term is well behaved and that for the other is ill-behaved.

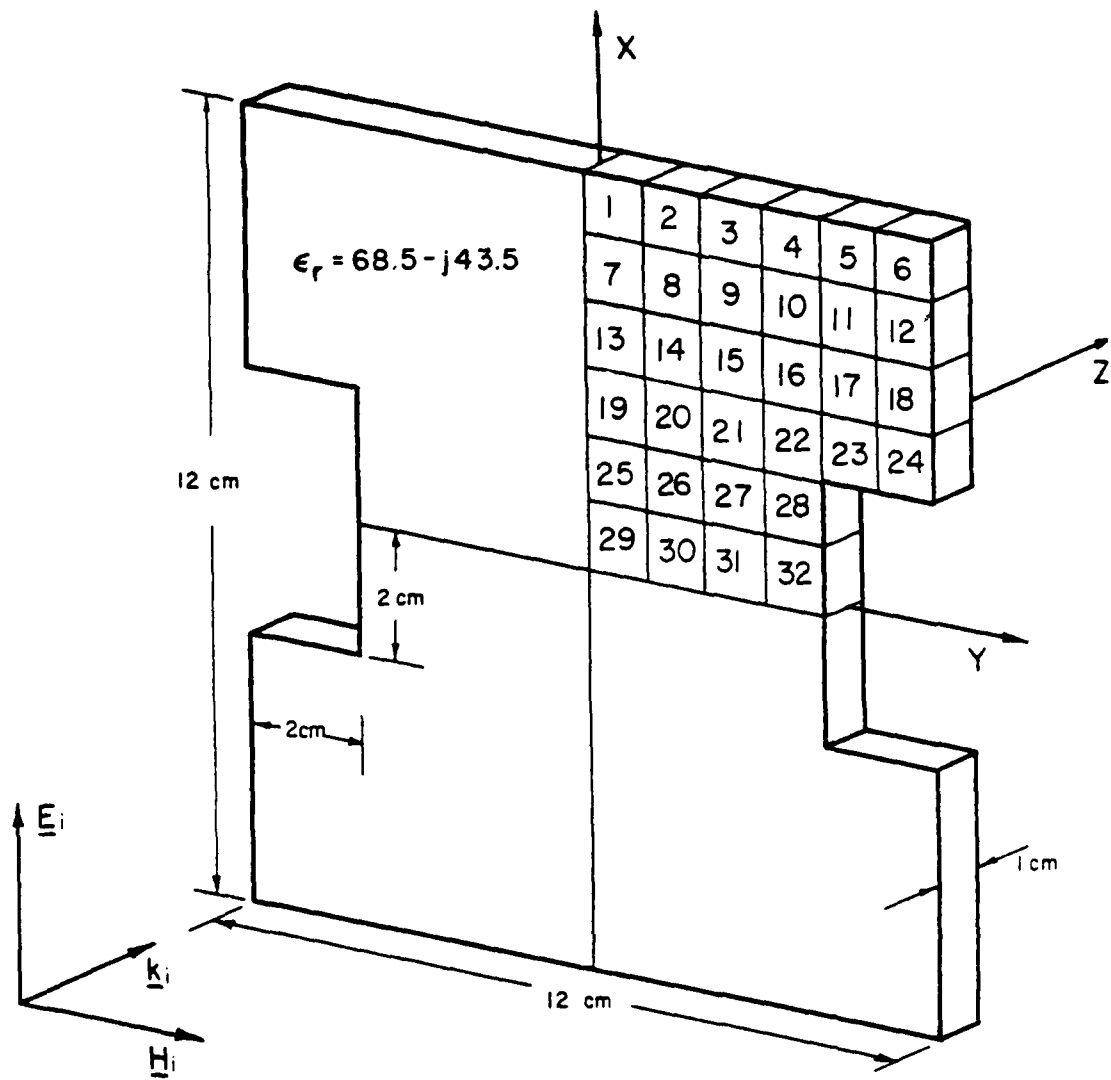


Figure 19. An I-shaped box of saline water under plane wave excitation (numbers are the index numbers for the volume cells).

TABLE III
ELECTRIC FIELD DISTRIBUTION IN THE 128-CELL BLOCK

E_x -DISTRIBUTION IN THE 128-CELL BLOCK

CELL NO.	PRESENT CALCULATION	MICHIGAN STATE	
		CALCULATED	MEASURED
1	.0545	.0573	---
2	.0342	.0353	---
3	.0656	.0676	---
4	.0279	.0294	---
5	.0906	.0879	---
6	.0899	.0887	---
7	.0787	.0807	---
8	.0557	.0558	---
9	.1028	.1071	---
10	.0165	.0173	---
11	.1103	.1057	---
12	.1027	.1018	---
13	.0775	.0769	.0770
14	.0681	.0681	.0681
15	.0967	.1017	.1017
16	.0393	.0386	.0518

TABLE 111 (Continued)

 E_x -DISTRIBUTION IN THE 128-CELL BLOCK

CELL NO.	PRESENT CALCULATION	MICHIGAN STATE	
		CALCULATED	MEASURED
17	.0985	.0873	.0911
18	.0940	.0941	.0766
19	.0562	.0577	---
20	.0544	.0575	---
21	.0601	.0571	---
22	.0571	.0562	---
23	.0577	.0571	---
24	.0577	.0613	---
25	.0577	.0421	---
26	.0577	.0665	---
27	.0601	.0571	---
28	.1111	.1491	---
29	.0613	.0617	.0617
30	.0611	.0695	.0739
31	.0696	.0661	.0661
32	.1834	.1887	.0766

TABLE III(Continued)

E_y-DISTRIBUTION IN THE 128-CELL BLOCK

CELL NO.	PRESENT CALCULATION	MICHIGAN STATE	
		CALCULATED	MEASURED
1	.0228	.0239	---
2	.0482	.0501	---
3	.0467	.0424	---
4	.0698	.0623	---
5	.0743	.0681	---
6	.0497	.0466	---
7	.0309	.0303	---
8	.0867	.0858	---
9	.1254	.1256	---
10	.1215	.1234	---
11	.0892	.0912	---
12	.0490	.0500	---
13	.0197	.0192	.0243
14	.0450	.0420	.0316
15	.0496	.0423	.0423
16	.0565	.0486	.0486

TABLE III(Continued)

 E_y -DISTRIBUTION IN THE 128-CELL BLOCK

CELL NO.	PRESENT CALCULATION	MICHIGAN STATE	
		CALCULATED	MEASURED
17	.0713	.0671	.0547
18	.0567	.0544	---
19	.0170	.0162	---
20	.0512	.0485	---
21	.0957	.0937	---
22	.1370	.1382	---
23	.1482	.1506	---
24	.1131	.1136	---
25	.0299	.0296	---
26	.0658	.0641	---
27	.0580	.0544	---
28	.0304	.0262	---
29	.0164	.0162	.0194
30	.0375	.0369	.0371
31	.0355	.0344	.0344
32	.0165	.0157	---

TABLE III(Continued)

E_t-DISTRIBUTION IN THE 128-CELL BLOCK

CELL NO.	PRESENT CALCULATION	MICHIGAN STATE	
		CALCULATED	MEASURED
1	.05906	.06208	---
2	.05910	.06123	---
3	.08048	.07979	---
4	.07517	.06709	---
5	.11720	.11119	---
6	.10280	.10019	---
7	.08449	.08627	---
8	.10300	.10235	---
9	.16220	.16500	---
10	.12270	.12460	---
11	.14180	.13961	---
12	.11380	.11342	---
13	.07995	.07926	---
14	.08163	.08001	---
15	.10870	.11015	---
16	.06883	.06206	---

TABLE III (Continued)

 E_t -DISTRIBUTION IN THE 128-CELL BLOCK

CELL NO.	PRESENT CALCULATION	MICHIGAN STATE	
		CALCULATED	MEASURED
17	.11520	.10853	---
18	.10980	.10869	---
19	.05870	.05897	---
20	.07472	.07522	---
21	.10760	.10702	---
22	.16680	.16954	---
23	.16210	.16252	---
24	.14080	.14030	---
25	.05210	.05146	---
26	.09062	.09236	---
27	.07433	.06949	---
28	.14720	.15167	---
29	.06537	.06579	---
30	.07588	.07870	---
31	.07810	.07450	---
32	.18410	.18940	---

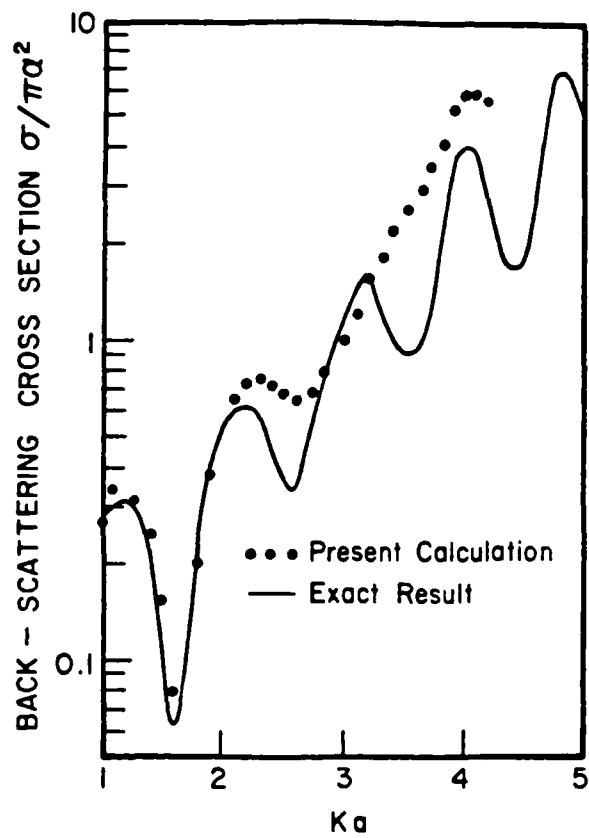


Figure 21. Calculation of RCS of a sphere with a dielectric constant of 2.592 as a function of radius a .

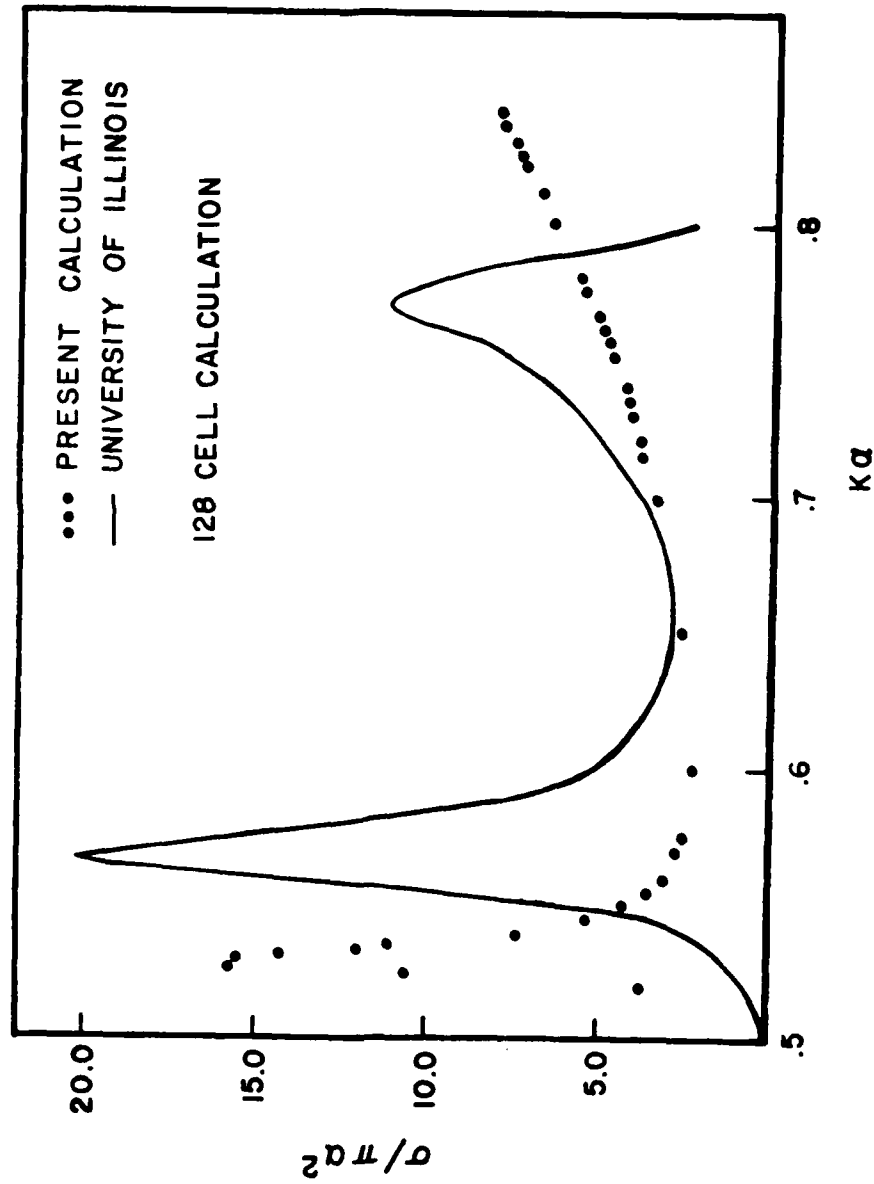


Figure 22. Calculation of back-scatter cross-section for a sphere of radius a and $\epsilon_r = 29.43 - j0.158$.

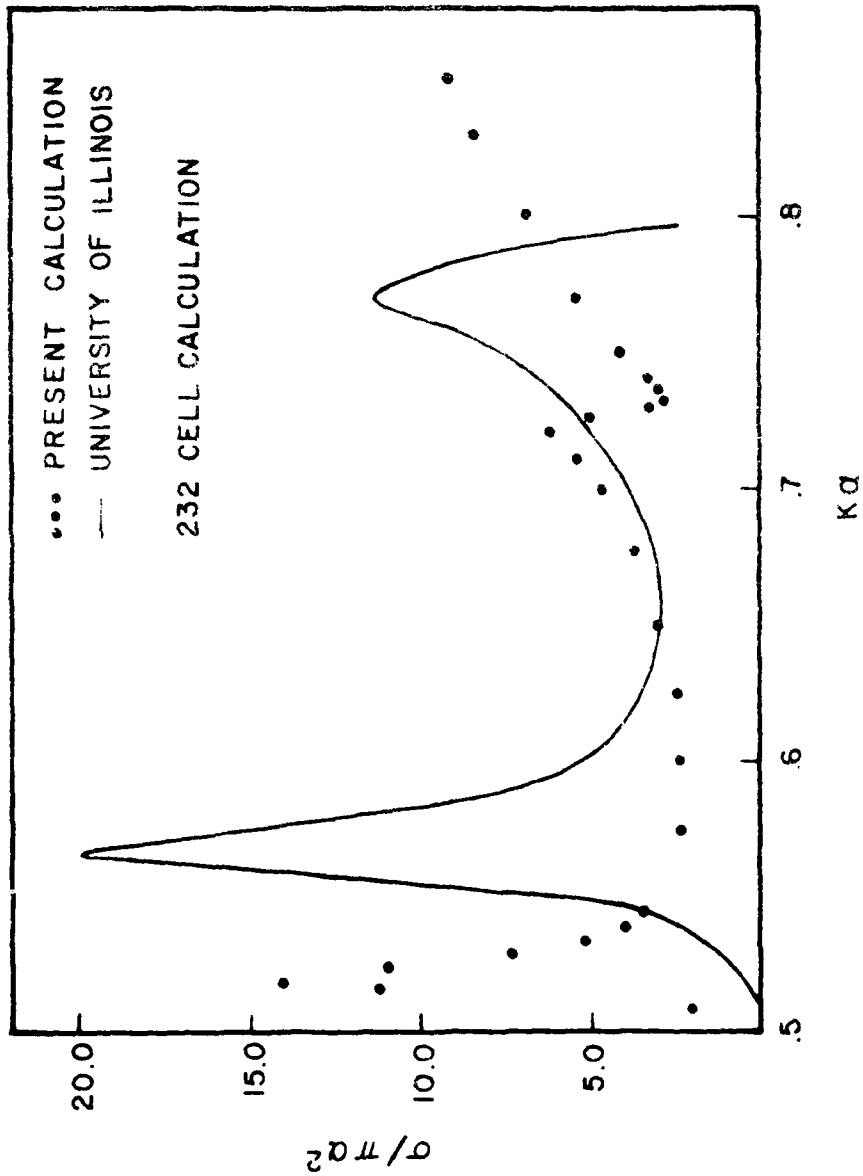


Figure 23. Calculation of backscattered cross-section for a sphere of radius a and $F_1 = 20.5$ (Ref. 168).

B. Scattering Computation for 1-foot birds

The Green Wingtail, which is an important migrant bird, was selected for extensive measurement and computation. This bird is typically 14.75 to 15.50 inches and weighs about a pound. At 1 GHz this bird is about 1 wavelength in length. Figures 13 and 14 show plaster-of-paris models for a Green Wingtail in sitting and flight positions, respectively.

Four simulation models, SB1 through SB4, were generated in this project. For the first three models, a number of problems developed in the experimental work. The permittivity was too high or too low or not uniform. These difficulties and the unsatisfactory data for the sphere directed the computation toward a more conservative approach. It was then decided that measurement for the bird should be started with a smaller bird exactly as the numerical model made of a group of cubic volume cells. With this principle in mind, SB4 was fabricated. Figure 24 shows the print-out of the cell centers for the side, front and top views for SB4. Figure 26 shows the geometry of the coordinate system and a plane wave incident in the x-z plane, which is the plane of symmetry for the bird. Figures 27 and 28 show fair agreement between the computed and measured results. It is noticed that the agreement is good as long as there is no sharp variation in the pattern. This difficulty in predicting sharp field variation and resonance phenomena may explain the use of specific absorption rate (SAR) in dealing with dielectric scattering problems [38].

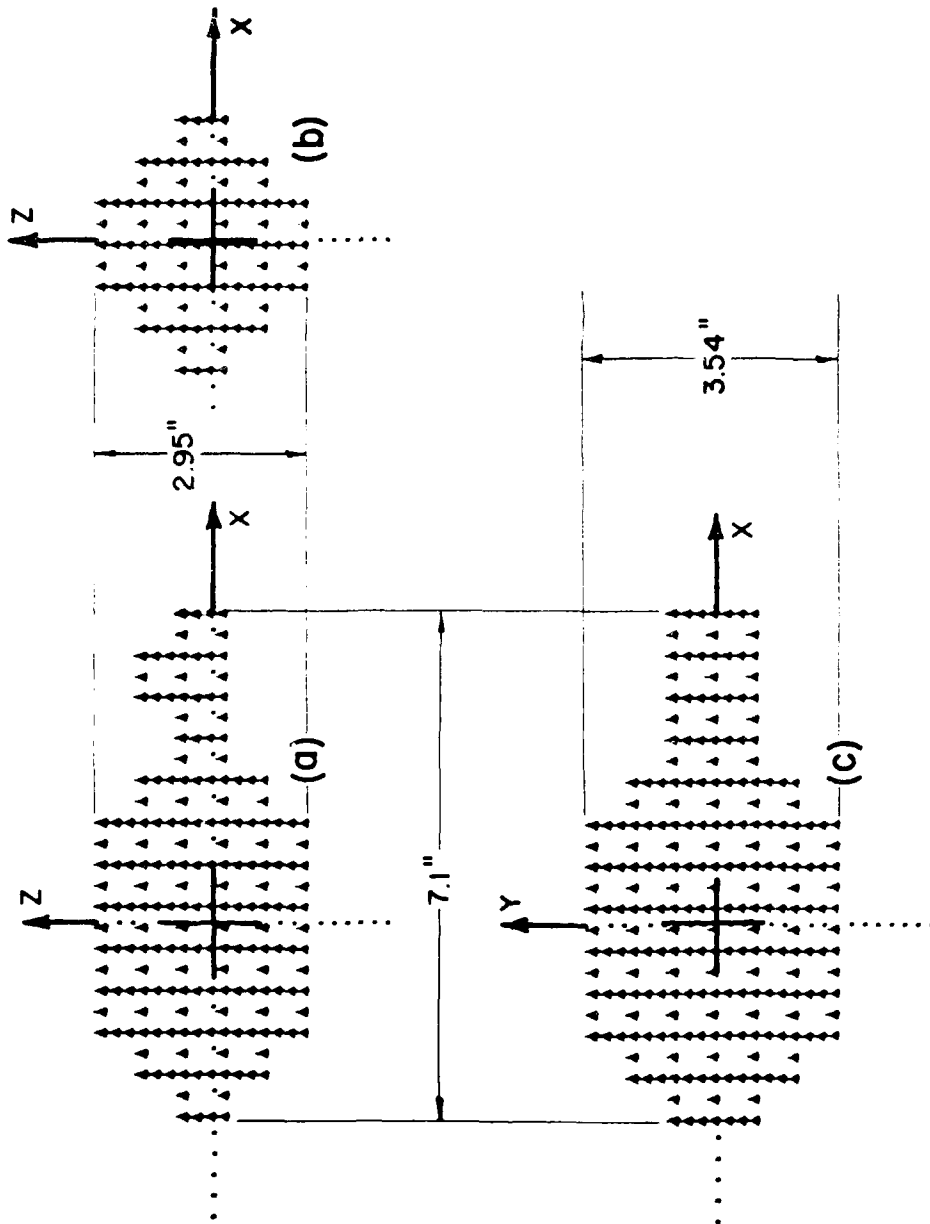


Figure 24. Side(a), front(b), and top(c) views of the 118 cell bird no. SB-4 to simulate a 0.8 pound Green-Winged Teal, $\sigma_F = 47.0 - j13.2$.

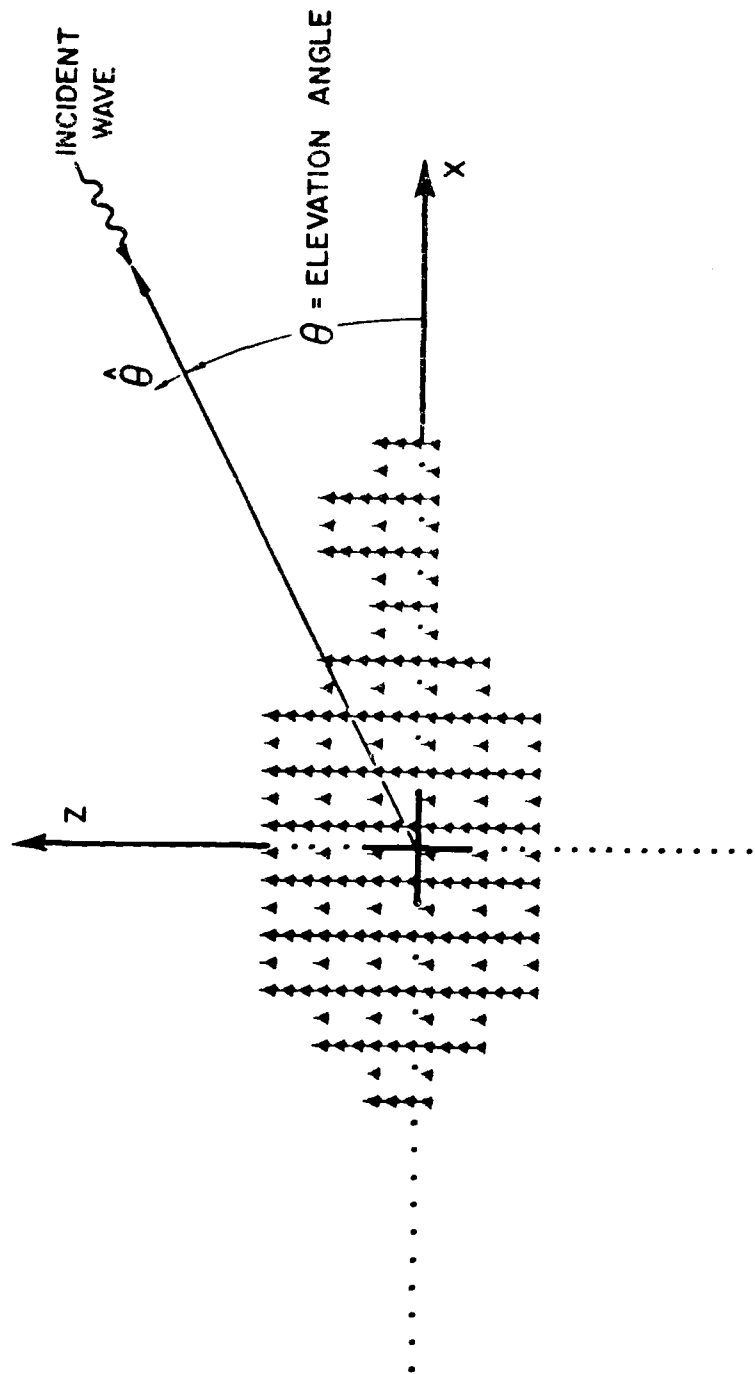


Figure 25. Simulated bird model SB4 under plane wave excitation.

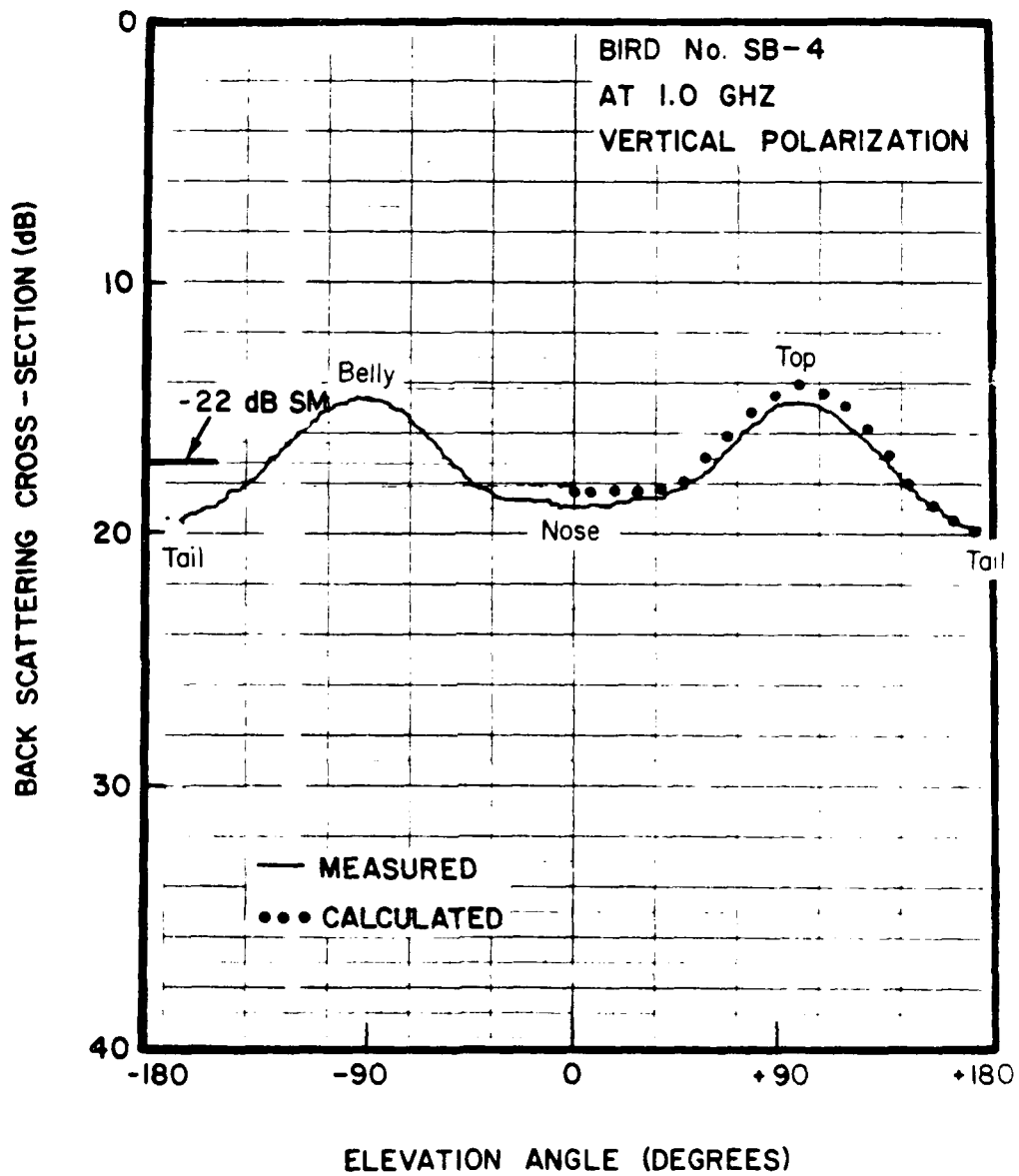


Figure 26. Back scattering cross section of bird SB4 versus elevation angle θ with vertical polarization as shown in Figures 25 and 26.

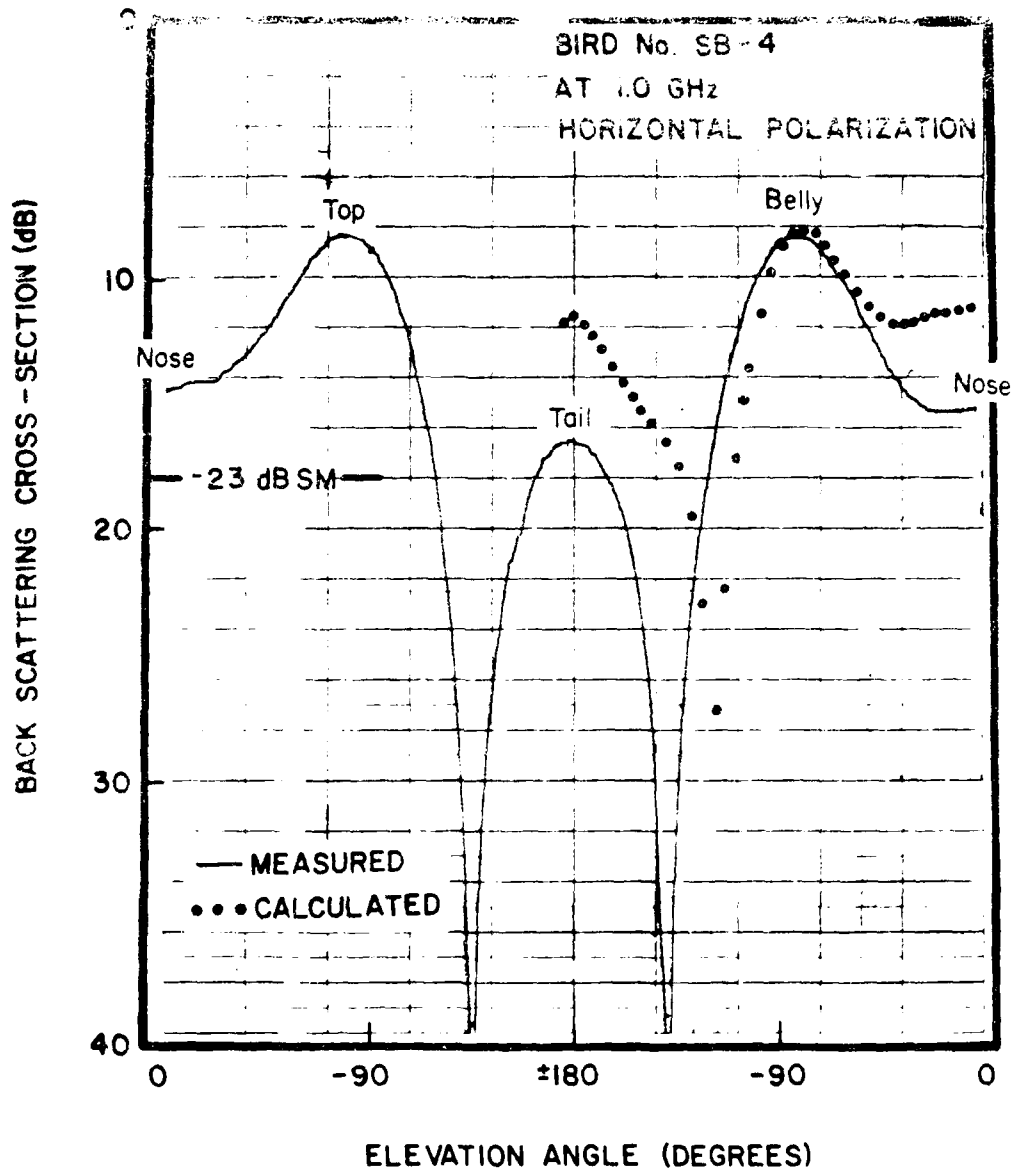


Figure 27. Back scattering cross section of bird SB4 versus elevation angle θ with horizontal polarization as shown in Figures 25 and 26.

SECTION V
IMPROVEMENTS OF COMPUTER ALGORITHM

A number of modifications have been made on the existing Georgia Tech volume integral equation algorithm to make it more efficient for the computation of dielectric scatterers. Major improvements included: (1) the reduction of execution time and central memory requirement by 50% by using symmetrical matrices, and (2) the reduction of execution time and central memory requirement by 75% for scattering problems with one-plane symmetry and by 87.5% for scatterers with two-plane symmetry. In addition, the banded matrix [43,44] and virtual memory [45] techniques have been implemented successfully for small scatterers and a new local-file manipulation technique has been explored.

A. Symmetrical Matrices

It can be shown that the matrix of the volume integral equation algorithm is symmetrical if the following conditions are satisfied.

- (1) the dielectric body is homogeneous and has a constant permittivity,
- (2) the volume cells are equal in size,
- (3) the volume cells are identical in shape.

The third condition is not critical and can often be ignored. To prove this, one can examine the following matrix elements in the algorithm.

$$Z_{pk}^{ln} = \int -j\omega u_0 \left[\delta_n^k + \frac{1}{k_0^2} \frac{\partial^2}{\partial u_n \partial u_k} \right] \frac{e^{-jk_0 |\underline{r}_p - \underline{r}'|}}{4\pi |\underline{r}_p - \underline{r}'|} B_l^k(\underline{r}') d\underline{r}' - \frac{\epsilon_r(\underline{r}_p) + 2}{3j\omega [\epsilon_r(\underline{r}_p) - \epsilon_0]} \delta_k^n \delta_p' \quad (48)$$

and

$$Z_{ln}^{pk} = \int -j\omega u_0 \left[\delta_k^n + \frac{1}{k_0^2} \frac{\partial^2}{\partial u_k \partial u_n} \right] \frac{e^{-jk_0 |\underline{r}_l - \underline{r}'|}}{4\pi |\underline{r}_l - \underline{r}'|} B_p^n(\underline{r}') d\underline{r}'$$

$$-\frac{\epsilon_p(\mathbf{r}_p) + 2}{3j\omega[\epsilon(\mathbf{r}_p) - \epsilon_0]} \delta_n^k \delta_l^p \quad (49)$$

where $k, n = 1, 2, 3$ or x, y, z

$l, p = 1, 2, \dots, L$; the index number of volume cell,

δ_n^k = the Kronecker delta function,

B_{lk}^k = a pulse function being unity in the l th volume cell associated with k (which designates x, y or z and is merely a dummy index number of no consequence to the integration).

Since the pulse function B_p^n restricts the domain of integration to the unit volume, cell l in Equation (48) and cell p in Equation (49),

$|\mathbf{r}_l - \mathbf{r}'_l|$ and $|\mathbf{r}_p - \mathbf{r}'_p|$ are equal. Thus Z_{pk}^{ln} and Z_{ln}^{pk} are equal under the three conditions stated.

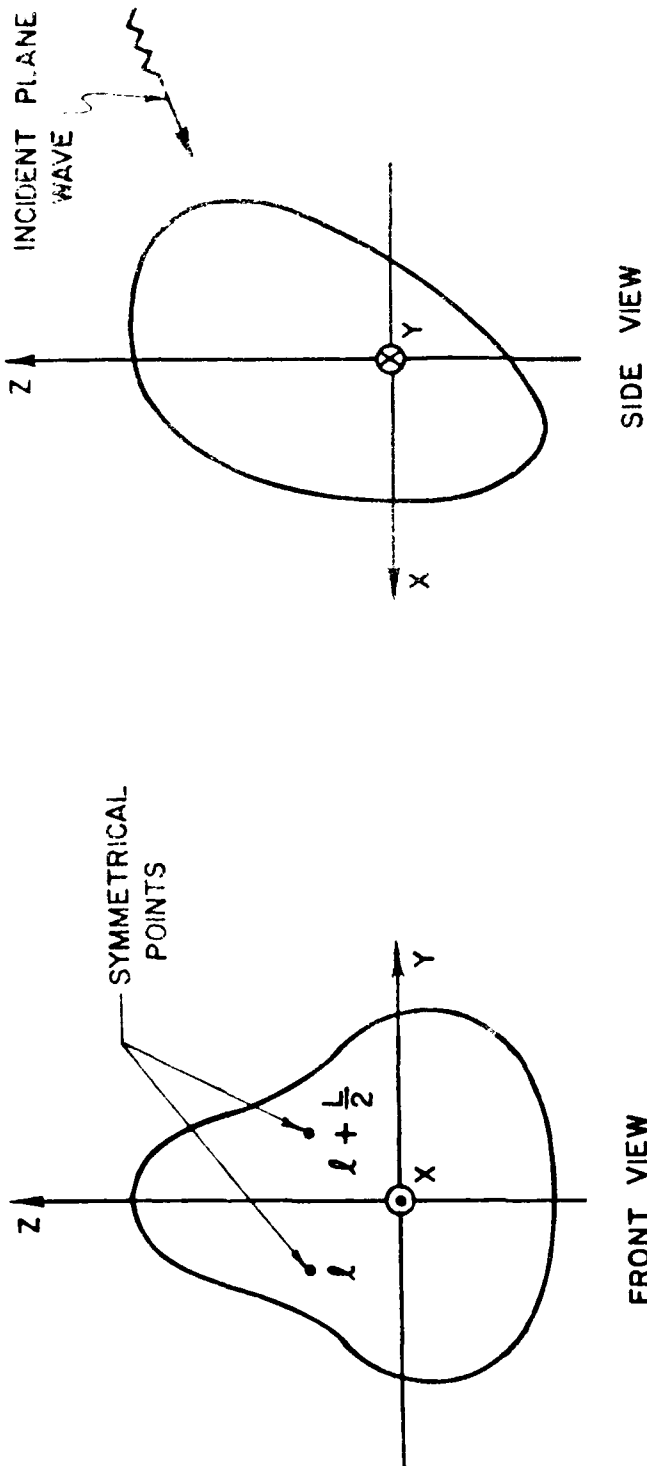
For a symmetrical matrix, there are standard subroutines to handle its inversion or solution. The improved Georgia Tech algorithm is given an acronym "BPWSM" to denote "Biological-Plane-Wave-Symmetrical Matrix". This algorithm has been successfully applied in a number of cases with a resulting 50% reduction in computer central memory and execution time.

COMPUTATIONAL SCHEMES

Two improved algorithms, BHPW2 and BHPW4, have been completed to handle scattering problems with one-plane and two-plane symmetries with resulting reductions of 75% and 87.5% in computer time and central memory, respectively. These are discussed separately as follows.

(1) Scattering problems with one-plane symmetry (BHPW2)

When the direction of propagation of an incident plane wave is in the plane of symmetry of a conducting scatterer, it is recognized that some symmetric behavior must exist in the induced current on the surface of the scatterer. Without loss of generality, Cartesian coordinates can be set up so that the plane of symmetry coincides with the XZ plane as shown in Figure 1b. The polarization



PLANE OF SYMMETRY - XZ

Figure 28. A symmetrical scatterer illuminated by a plane wave incident in the plane of symmetry.

of the incident wave is assumed to be either parallel or perpendicular to the XZ plane. Arbitrary polarization can be decomposed into two components, one parallel and the other perpendicular to the XZ plane. The overall scattering problem can then be treated by superposing the fields due to these two component incident fields.

At two symmetrical points ℓ and $\ell + L/2$ in Figure 28, the components of the induced currents exhibit the following relationships

$$\begin{aligned} J_{\ell}^x &= J_{\ell + L/2}^x \quad , \\ J_{\ell}^y &= -J_{\ell + L/2}^y \quad , \\ J_{\ell}^z &= J_{\ell + L/2}^z \quad , \end{aligned} \tag{50}$$

when the incident \underline{E}^i is parallel to the z-axis. In Equation (50), J_{ℓ}^x denotes, for example, the x component of the induced current in the ℓ th cell.

When the incident \underline{E}^i is parallel to the y-axis, the induced current on the scatterer has the following property

$$\begin{aligned} J_{\ell}^x &= -J_{\ell + L/2}^x \quad , \\ J_{\ell}^y &= J_{\ell + L/2}^y \quad , \\ J_{\ell}^z &= -J_{\ell + L/2}^z \quad . \end{aligned} \tag{51}$$

The matrix equation to be solved is

$$\sum_{\ell=1}^1 \sum_{k=1}^3 J_{\ell}^k z_{pk}^{\ell n} = v_p^n \quad (52)$$

$$\begin{aligned} n &= 1, 2, 3 \\ p &= 1, \dots, L. \end{aligned}$$

Since the excitation is symmetrical, we have

$$v_{\ell}^n = v_{\ell + L/2}^n \quad (53)$$

Substitution of Equations (50) and (53) into Equation (52) yields

$$\sum_{k=1}^{L/2} \sum_{\ell=1}^3 J_{\ell}^k [z_{pk}^{\ell n} + z_{pk}^{(L/2+\ell)n} (-1)^{k+1}] = v_p^n, \quad (54)$$

$$\begin{aligned} n &= 1, 2, 3 \\ p &= 1, 2, \dots, L/2 \\ \text{for } \underline{E}^i &= z \end{aligned}$$

Substitution of Equation (51) and (53) into Equation (52) yields

$$\sum_{\ell=1}^{L/2} \sum_{k=1}^3 J_{\ell}^k [z_{pk}^{\ell n} + z_{pk}^{(L/2+\ell)n} (-1)^k] = v_p^n \quad (55)$$

$$\begin{aligned} n &= 1, 2, 3 \\ p &= 1, 2, \dots, L/2 \\ \text{for } \underline{E}^i &= \hat{y} \end{aligned}$$

Equations (54) and (55) show that the number of equations has been reduced from 32 to 16(2).

1) x -plane symmetry.

Figure 29 shows a scattering problem symmetrical with respect to the x - z and y - z planes. The directive of propagation of a plane wave is assumed to be parallel to the z -axis. When $\hat{E}_z^i = \hat{z}$, we have

$$\left\{ \begin{array}{l} J_x^1 = J_x^2 = J_x^3 = J_x^4 \\ J_y^1 = -J_y^2 = -J_y^3 = J_y^4 \\ J_z^1 = J_z^2 = J_z^3 = J_z^4 \end{array} \right. \quad (56)$$

When $\hat{E}_z^i = \hat{y}$, we have

$$\left\{ \begin{array}{l} J_x^1 = J_x^2 = -J_x^3 = -J_x^4 \\ J_y^1 = J_y^2 = J_y^3 = J_y^4 \\ J_z^1 = -J_z^2 = -J_z^3 = J_z^4 \end{array} \right. \quad (57)$$

In addition, the excitation at cells 1,2,3 and 4 is identical. The number of Equations in Equation (54) can therefore be reduced to one-quarter of its original size as follows

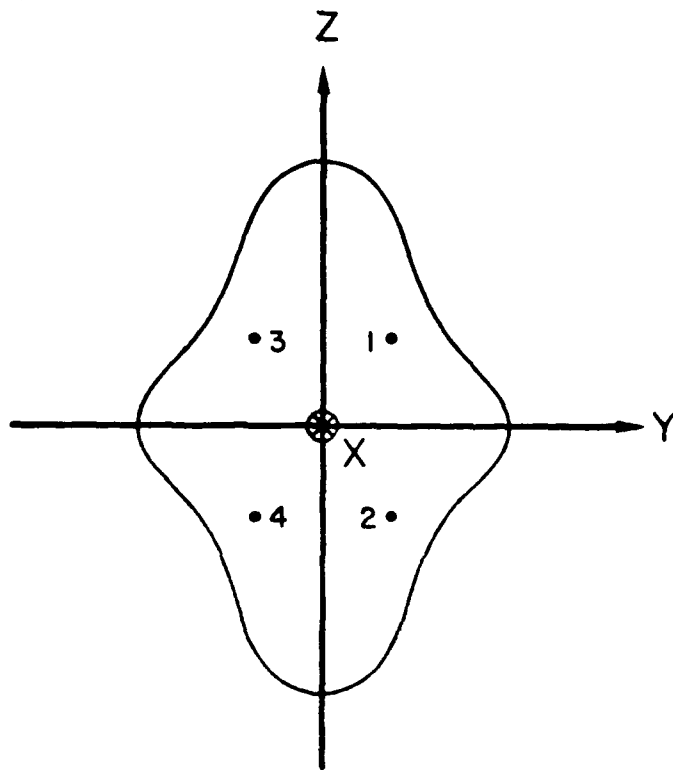


Figure 29. A scattering problem with two-plane symmetry.

$$\sum_{\ell=1}^{L/4} \sum_{k=1}^3 J_{\ell}^k \left\{ z_{pk}^{\ell n} + (-1)^{k+1} \left[z_{pk}^{(L/4+\ell)n} + z_{pk}^{(L/2+\ell)n} \right] + z_{pk}^{(3/4 L+\ell)n} \right\} = V_p^n \quad (58)$$

$$n = 1, 2, 3$$

$$p = 1, 2, \dots, L/4$$

when $\underline{E}^i = \hat{z}$.

Substitution of Equations (57) into Equation (52) yields

$$\sum_{\ell=1}^{L/4} \sum_{k=1}^3 J_{\ell}^k \left\{ z_{pk}^{\ell n} + (-1)^{k(1-\delta_{1k})} z_{pk}^{(L/4+\ell)n} + (-1)^{k(1-\delta_{2k})} z_{pk}^{(L/2+\ell)n} + (-1)^{k(1-\delta_{3k})} z_{pk}^{(3/4 L+\ell)n} \right\} = V_p^n \quad (59)$$

$$n = 1, 2, 3$$

$$p = 1, 2, \dots, L/4$$

when $\underline{E}^i = \hat{y}$. In Equations (59) δ_{ju} is the Kronecker delta.

C. Banded Matrix Techniques

The banded matrix technique has been previously employed by Ferguson, et al. [43] and Balestri, et al. [44] in the scattering and radiation of thin-wire structures. These authors have demonstrated that the banded matrix technique can reduce the computer execution time in the computation of thin-wire scattering and radiation involving small matrices. They also demonstrated that wire-grid problems involving more wire segments than can be managed in the computer central memory can be solved by the banded matrix technique after proper numbering of wire segments. The segments are

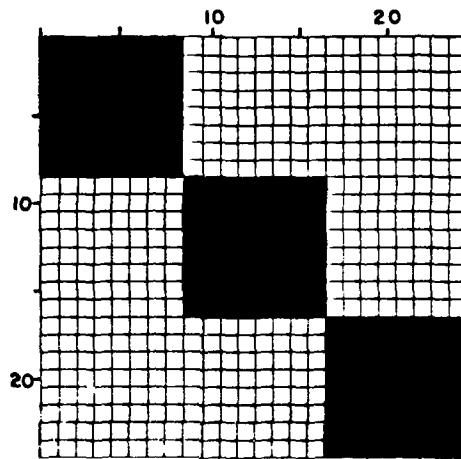
numbered such that the difference between segment numbers for all neighboring segment pairs is small as compared with the total number of segments. In this case the large matrix elements are kept close to the principal diagonal of the matrix.

The basic banded matrix technique has been applied to the Volume Integral Equation algorithm. However, there are three unknowns in the n th cell in the Volume Integral Equation approach, while there is only one unknown in the n th segment in the wire algorithm. Fortunately the matrix generated in the Volume Integral Equation algorithm has a tendency to be banded. Figure 31 shows the matrix for the case of a simple cylinder formed with a linear array of volume cells. It can be seen that a diagonal band extended to one third of the columns and the rows must be included in order to include all the nonzero elements. It is also noted that outside this band all the matrix elements are zero. This phenomenon is due to the lack of coupling between orthogonal components of the electromagnetic source and field. For an object of more complex geometry, such as a sphere, elements throughout the entire matrix can be nonzero except for those related to the coupling between orthogonal components in the self cell. Figure 32 shows the matrix for the case of a prolate spheroid of 12 cells, which is weakly banded with some nonzero elements away from the diagonal band.

We now define the normalized width of the diagonal band as

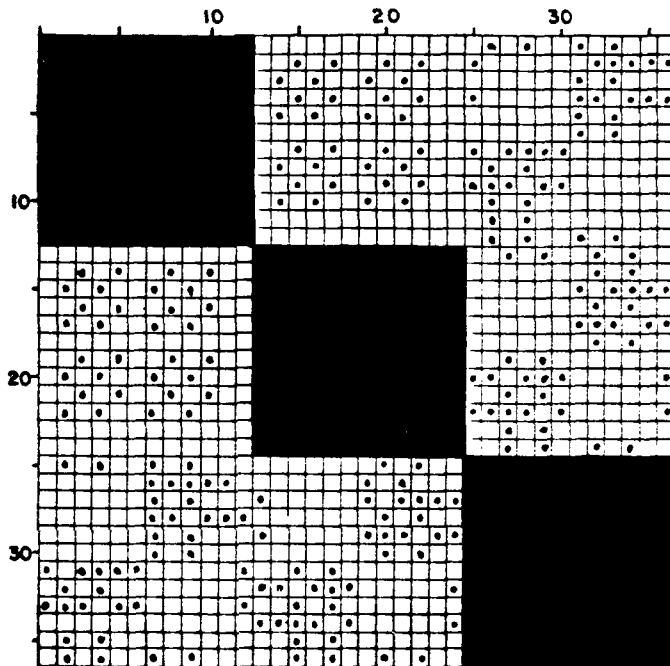
$$\text{Normalized Width of diagonal band} = [(\text{number of rows in band}) + (\text{number of columns in band})] / [(\text{total number of rows}) \times 2] \quad (60)$$

Numerical tests have been conducted to explore the convergence of the solutions as a function of the normalized width of the diagonal band. Figure 33 shows that the error in the solution is reduced as the width of the diagonal band is increased. The error falls to near zero when the normalized width of the diagonal band is only 0.6. Note that for a general matrix the error reaches zero when the normalized width of the diagonal band approaches unity. It is also noteworthy that the error is only 5% when the normalized width of the diagonal is 0.15 or larger. Thus, a



Note: \blacksquare The size of the shaded area in the square cell is proportional to the magnitude of the matrix element.

Figure 30. A display of the magnitude of matrix elements in a VIE matrix for an 8-cell dielectric cylinder which is strongly banded.



Note: \blacksquare The size of the shaded area in the square cell is proportional to the magnitude of the matrix element.

Figure 31. A display of the magnitude of matrix elements in a VIE matrix for a 12-cell prolate spheroid which is weakly banded.

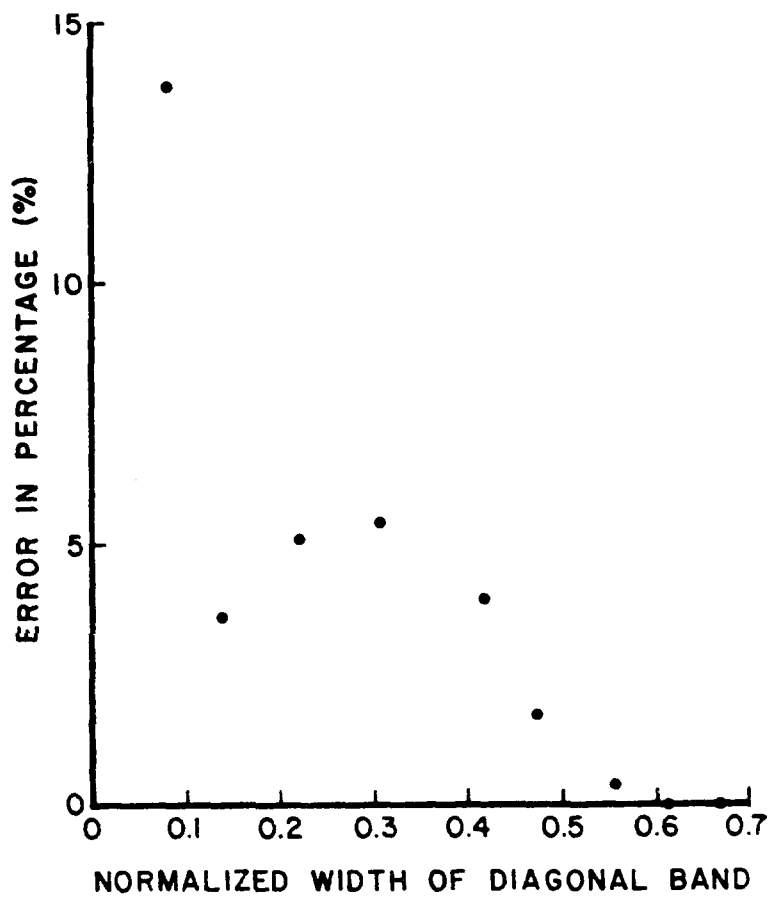


Figure 32. Convergence of solution for the case of a 12-cell prolate spheroid expressed in percentage of error as a function of the normalized width of diagonal band.

significant reduction of execution time can be attempted for a small scatterer. These numerical tests also strongly indicate that a large scatterer, which can not be handled in the computer central memory, may be treated using the banded matrix technique.

D. Virtual Memory Technique

The virtual memory is a software technique, in contrast to the extended-memory hardware capability, to store data in a digital computer for rapid and efficient access in computer-aided numerical analyses to overcome the limitations imposed by the size of the computer central memory. The basic algorithm had been developed by Carbre [45] for real-valued data, and was employed in the present research to expand the capability of the Volume Integral Equation algorithm to handle large dielectric scatterers. When using exclusively the computer central memory to handle the matrix in the computation, the CDC CYBER-74 computer at Georgia Tech can only deal with matrices of about 38,300 complex elements, or about 65 volume cells. The use of the virtual memory technique can potentially make it possible to handle a matrix with 4×10^6 complex elements, or 660 volume cells, which is about ten times the size of those limited by the computer central memory. A serious disadvantage of the virtual memory technique is its extremely large execution time, often ten times more than methods using central core memory alone.

The tasks involved in implementing the virtual memory technique in the Volume Integral Equation algorithm are twofold; the Carbre algorithm must be extended to handle complex data and be integrated into the process of the moment method solution. Both of these difficulties have been overcome and successfully tested for small and medium scatterers. For large scatterers considerably exceeding the central memory, the computational efficiency is low and needs to be improved.

There are two steps involved in the numerical solution of a system of linear equations. First the matrix elements involved must be computed and stored for easy access. Secondly, the matrix equation must be solved by a certain process using either the central memory alone or the virtual memory, which uses both the central memory and disk memory. Both steps need large computer execution time and the key issue is to reduce the computer time to a level acceptable for practical computations.

E. Local-File Manipulation Technique

As has been noted in the preceding section, the virtual memory technique is capable of handling large matrices beyond the capacity of the computer central memory, but it is handicapped by the extremely long execution time needed. For example, 150,000 CPU sec is required in a computer run involving the solution of a 486 x 487 matrix. Furthermore, the CPU time required increases astronomically with the number of matrix elements when it exceeds the capacity of the computer central memory. In order to overcome this difficulty, a highly efficient "local-file manipulation" technique was developed at Georgia Tech. This technique, which has been tested only for small and medium-sized matrices, utilizes both the discs and the central memory for the storage of the matrix elements.

Similar to the virtual memory technique, the local-file manipulation method is a software technique and it has been written at Georgia Tech in Fortran V and COMPASS languages; the latter being a machine language used on CDC Cyber 74. The key elements of the program include twenty-seven subroutines, eleven of which are written in COMPASS. These subroutines were implemented in the dielectric scattering calculation program used in this research project. They can be divided into three groups according to their functions as illustrated in Figure 33 and Table IV. Appendix I lists all these subroutines and describe their functions.

The key features of the local-file manipulation technique are in the efficient ways of storing and recalling the matrix elements as well as the specific method of solving the system of linear equations by the lower-upper decomposition method.

All the matrix elements are stored in the present program in four local files, each of which is allocated a certain disc space. The matrix elements are first divided into, say, three portions as shown in Figure 34. Elements in each of the corresponding rows of the three partitions are computed and stored in small arrays in the core memory. As soon as the three rows have been fully generated, these three rows are transferred from core

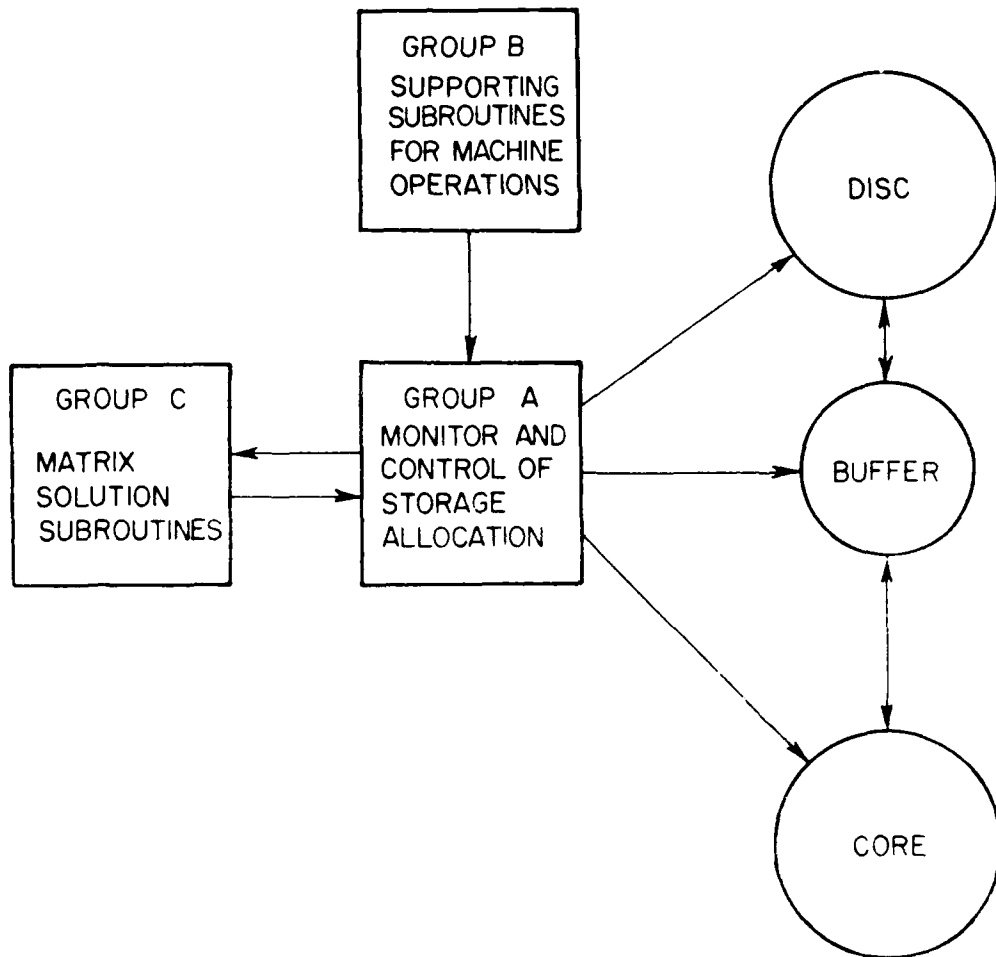


Figure 33. Block diagram for the local-file manipulation algorithm.

AD-A096 062

GEORGIA INST OF TECH ATLANTA ELECTROMAGNETIC EFFECTI--ETC F/G 20/3
A STUDY OF THE ANALYSIS AND MEASUREMENTS OF THREE-DIMENSIONAL A--ETC(U)
DEC 80 J J WANG, C PAPANICOLOPULOS F19628-78-C-0223

UNCLASSIFIED

RADC-TR-80-372

NL

2 of 2
AD-A
096062



END
DATE
FILMED
4-81
DTIC

TABLE IV
 SUBROUTINES USED IN THE LOCAL-FILE
 MANIPULATION ROUTINE

GROUP A SUBROUTINES	GROUP B SUBROUTINES	GROUP C SUBROUTINES
MMINIT	MMALOCK	MMCDCOM
MMSTAT	MMLINK	MMCFBS
MMLOCK	MMSUPRT	MMCRNRM
MMSROW	MMCIO	MMCRSUB
MMGROW	MMMSG	
MMSLLM	CDD	
MMBAHED	MMECL	
MMUPACK	MMCLPT	
MMGBUF	MMFSET	
MMINBND	MMRBUSY	
MMGIRA	MMSPLM	
MMSINED		

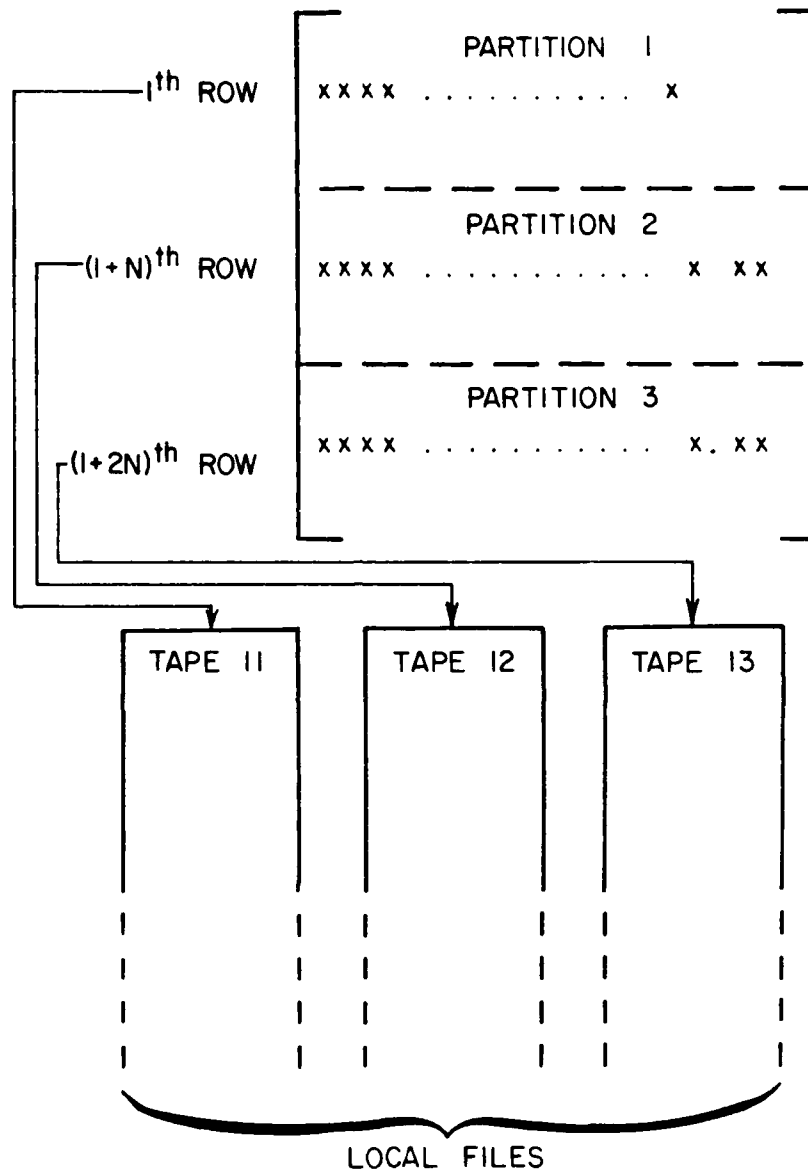


Figure 34. The local-file simultaneous storage process for the I^{th} , $(I + N)^{\text{th}}$ and $(I + 2N)^{\text{th}}$ rows in a large $3N \times 3N$ matrix.

memory to local files in binary form with a "WRITE" statement. The process is repeated for N times until the complete matrix has been generated and stored in the three local files. This storage process is highly efficient in comparison with the conventional virtual memory technique because matrix elements of entire rows are read simultaneously into local files.

The solution of the matrix or the system of linear equations in the present local-file manipulation technique uses the lower-upper decomposition method described in Appendix II. There are two important features in this technique; the restorage of the matrix elements based on their frequencies of impending usage and the solution of the matrix by the lower-upper decomposition method.

In the restorage of the matrix elements a priority table is generated and stored in core memory to assign the "priority" level for each. Three priority levels, high, last and low, are assigned to the rows. The "high" priority is assigned to the row for which immediate and frequent access is needed. The local-file manipulation algorithm has been tested on the Georgia Tech CDC Cyber 74 computer with good results for small and medium sized matrices. Figure 35 shows a comparison for the time required for the generation and storage of the matrix elements between the virtual memory algorithm of Carbrey and the present local-file manipulation algorithm. This greatly improved efficiency in the storage process is probably due to the row storage method discussed previously. The matrix solution time required in the local-file manipulation technique is also much less time consuming than the Carbrey algorithm as shown in Figure 36. These comparisons are made only for small matrices and it remains to be seen whether similar comparisons hold for very large matrices. Unfortunately further study for the case of large matrices cannot be conducted within the time and resources of the present research program. It appears, however, that the local-file manipulation technique will prove to be considerably superior to the Carbrey virtual memory technique when applied to large matrices. A major advantage of the lower-upper decomposition process is that one does not have to repeat the matrix element generation

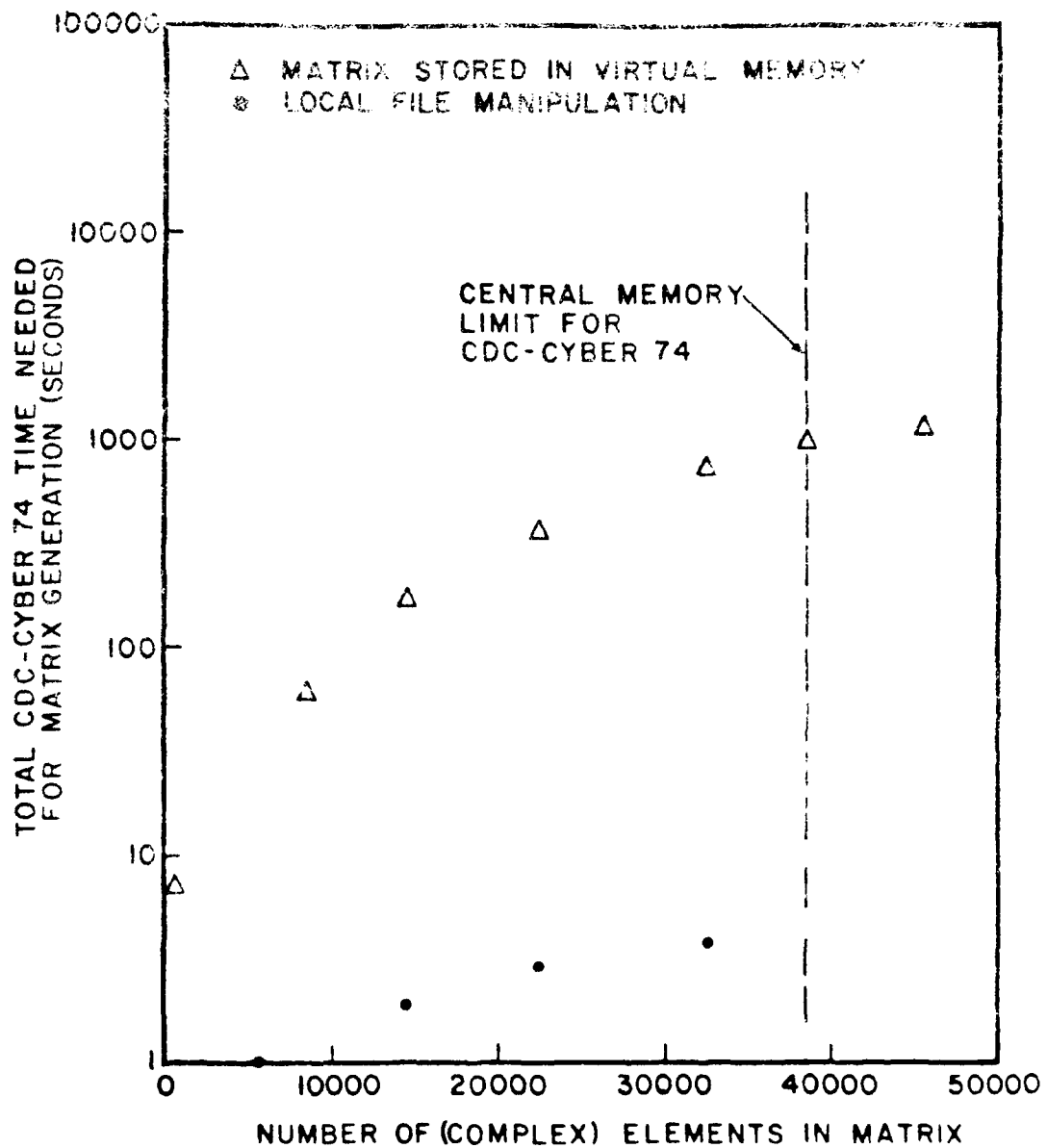


Figure 35. Comparison of computer time required to generate (including input/output time) a matrix of various size by various matrix storage methods.

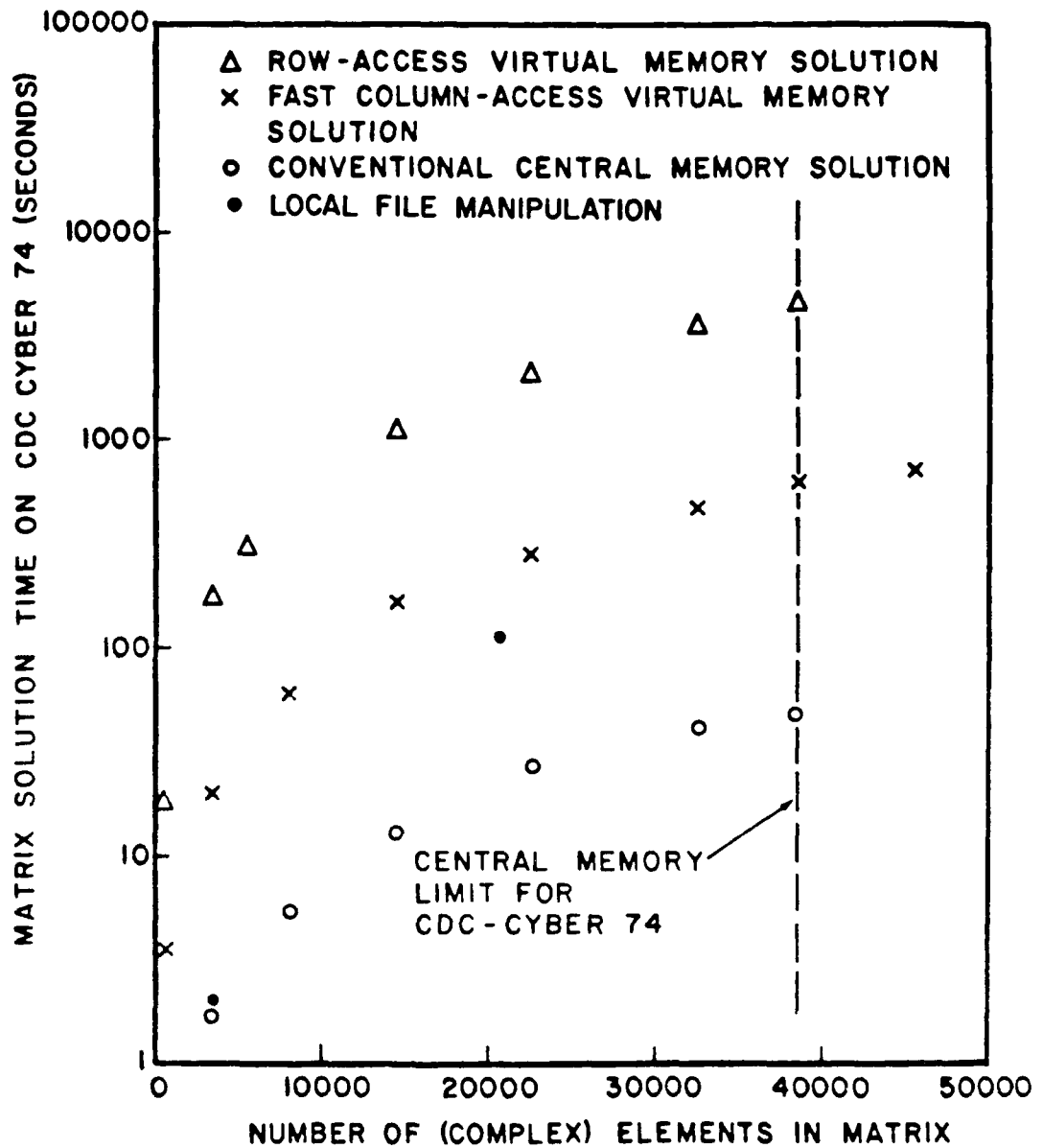


Figure 36. Comparison of matrix solution time on CDC CYBER-74 by various methods.

for different excitations and therefore saves large CPU time when the angle and polarization of illumination are changed. A disadvantage of this method is that it requires twice as much storage space as other methods such as the Gaussian-elimination method because of the need to store both the upper and lower matrices [L] and [U]. However, this disadvantage is not of significant consequence when it is used in the local-file manipulation method. Since the matrices are stored in the virtually unlimited disc space, the efficiency of storage and access to the matrices are more important than the size of the storage space required. In addition, the enlarged storage requirement in this method can be reduced by the band-storage-mode technique [46].

SECTION VI
 METHODOLOGY FOR THE MODELING OF THE SCATTERING
 OF A FLOCK OF FLYING BIRDS

In radar applications, the electromagnetic scattering from a flock of flying birds interferes with the detection and identification of objects, but it can also be used to track bird migratory patterns [47,48]. Radar return from birds is often observed as a large dot angel, which occurs at all microwave frequencies on virtually every type of radar. One of the most outstanding features of the scattering from a flock of birds, and hence the radar angel, is its irregularity; with variations of as much as three orders of magnitude [49]. This irregularity is due to that of the individual bird [3] and the density and formation of the flock.

Although the lack of repeatability and regularity in the scattering measurements for birds appears to fit a statistical model, several aspects of the problem are highly deterministic. The formation of a specific flock is quite orderly and therefore will probably be more accurately modeled deterministically. The individual birds can be better modeled statistically because of the variations in size, shape, and movements among them.

Let $\sigma(\nu, \nu)$ be a random variable which represents the back-scatter cross-section from a specific type of bird as shown in Figure 37. the total radar cross-section $\sigma_t^2(\nu, \nu)$ can be approximated by

$$\sigma_t^2(\nu, \nu) = \sum_{n=1}^N \sigma^2(\nu, \nu) e^{-2jk_0 \mathbf{r} \cdot \mathbf{r}_n} \quad (61)$$

where \mathbf{r} is a unit vector parallel to the line of sight between the radar and a reference bird in the flock, \mathbf{r}_n is the distance from the reference bird to a bird designated as number n , N is the total number of birds in the flock. Let the superscript $\bar{}$ denote "average", we have the expected total RCS of the flock as

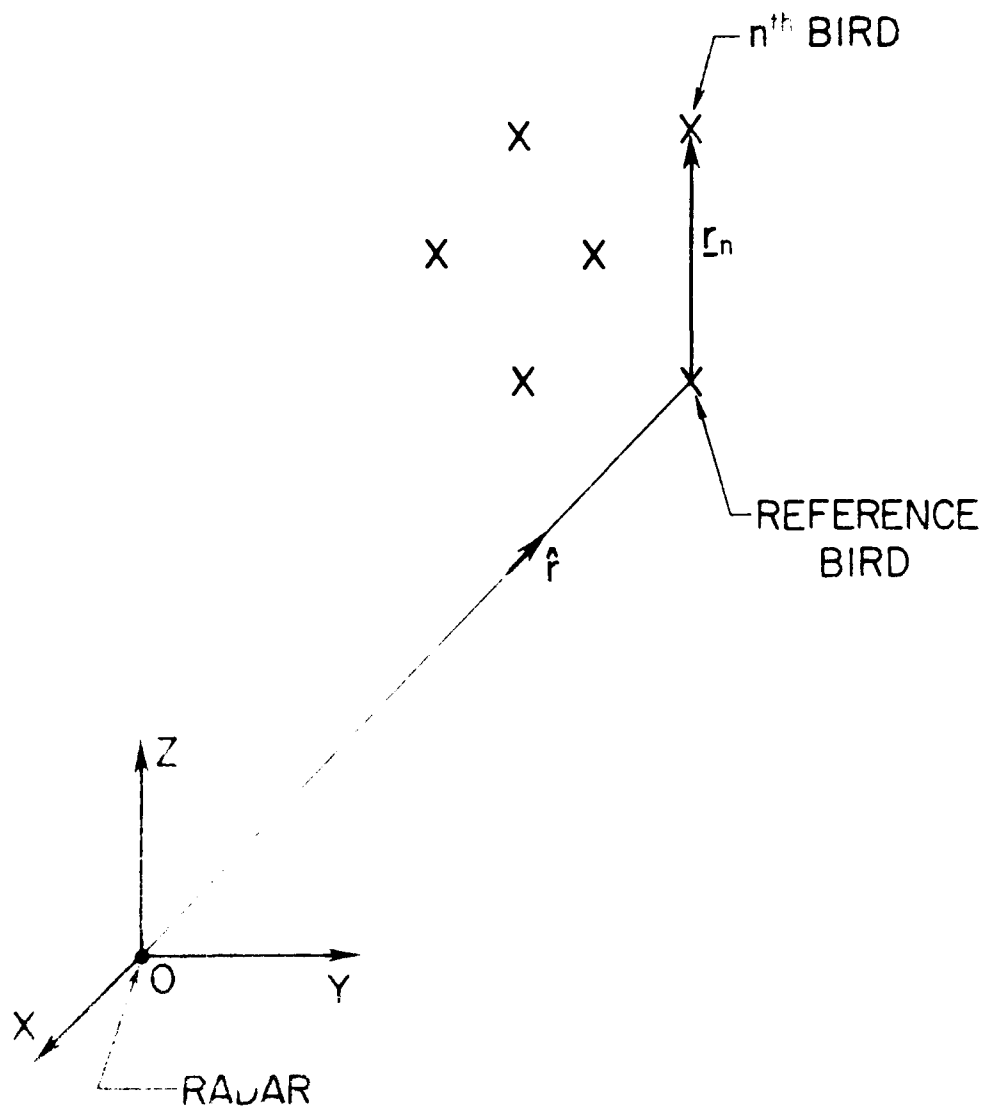


FIG. 1. Geometry of Bird Position Relative to Radar Station.

$$\sigma_t^2(\theta, \phi) = \sigma^2(\theta, \phi) \sum_{n=1}^N e^{-j2k_0 \hat{r} \cdot \underline{r}_n} \quad (62)$$

where it is assumed that the formation of the flock is deterministic, at least for the time interval under consideration.

The time variation of the radar return from a flock of flying birds is primarily due to the wing flapping and the flight path movement. The effect of this variation appears as radar scintillation and Doppler frequency shifts. Modeling of these phenomena can be based on the statistical characteristics of the random variable $\sigma(\theta, \phi)$ pertaining to a single bird.

Depending on the available data on the single bird, there are several ways to model the scattering characteristics of a flock of birds by using Equations (61) and (62). Equation (61) can be used to generate a Monte-Carlo simulation with the statistical parameters of the single bird. If it is desired to include the effect of the array formation, \underline{r}_n can also be considered as a random variable and be included in the model. If we are only interested in the time average scattering cross-section, Equation (62) is convenient to use as long as the average scattering cross-section of a single bird is known. The single bird data can be obtained by computation and measurement techniques discussed in this report. The techniques of modeling a flock of birds from scattering data of a single bird is similar in many ways to that of chaff cloud scattering problem, which has been recently investigated at Georgia Tech [50-52]. No numerical modeling was carried out in the research program because of the lack of quality data which can be used to compare with the model.

SECTION VII
CONCLUSIONS AND RECOMMENDATIONS

Research has been conducted in the analysis and measurements of three-dimensional arbitrarily-shaped heterogeneous dielectric and biological bodies. The discrepancies in the literature regarding the singularity of the electric dyadic Green's functions were resolved. The discrepancies were centered at the singularity of the rectangular cavity. It was shown in this report that the apparent discrepancies do not exist and a unified and consistent view was presented.

Compact range scattering measurements were successfully conducted at 1 GHz. Techniques in fabricating simulation models using the "Superstuff" were investigated and several 1-foot birds were made. Extensive numerical analysis was carried out for dielectric scatterers of various shapes including cylinders, rectangular blocks, I-shaped blocks, spheres, and a 1-foot bird. The accuracy of these computations was good except for the resonant sphere, for which the resonance frequencies were shifted by about 20 percent.

Various numerical techniques have been investigated. Computer central memory requirements and execution time were reduced by 50 percent with the symmetrical matrix technique and by 75 percent for scatterers of one-plane symmetry. Banded matrix and virtual memory techniques have been implemented in the Volume Integral Equation algorithm and tested successfully for small scatterers. A new local-file manipulation technique for handling matrices larger than core capacity was explored and the results for small matrices showed that it is potentially much more efficient than the virtual memory algorithm developed by Carbrej.

It is recommended that the computational techniques developed in this research program be extended to the analysis of larger lossy dielectric bodies. In addition, the Surface Integral Equation approach should be explored to see whether its numerical convergence is more rapid than the Volume Integral Equation approach. The derivation of an exact solution

for the dielectric prolate spheroid appears to be a feasible research subject which should lead to accurate and useful data for dielectric scattering problems.

SECTION VIII

REFERENCES

1. P.M. Morse and H. Feshbach, Methods of Theoretical Physics, McGraw-Hill Book Co., Inc., New York 1953.
2. C.T. Tai, Dyadic Green's Functions in Electromagnetic Theory, Intext Educational, Scranton, PA, 1971.
3. O.D. Kellogg, Foundations of Potential Theory, Springer Verlag, New York 1967 (reprinted from 1st ed., 1929).
4. J. Van Bladel, "Some remarks on Green's dyadic for infinite space," IEEE Transactions on Ant. and Prop., Vol. AP-9, pp. 603-60, Nov. 1961.
5. J.G. Fikioris, "Electromagnetic field inside a current-carrying region," J. Math. Phys., Vol. 6, pp. 1617-1620, Nov. 1965.
6. D.E. Livesay and K.M. Chen, "Electromagnetic fields induced inside arbitrarily shaped biological bodies," IEEE Trans. Microwave Theory Tech., Vol. MIT-25, pp. 1223-1229, Dec. 1977.
7. G.W. Hohmann, "Three-dimensional induced polarization and electromagnetic modeling," Geophysics, Vol. 40, pp. 309-324, April 1975.
8. J.J.H. Wang, F.L. Cain, and E.C. Burdette, "Numerical Modeling of Three-dimensional arbitrarily-shaped heterogeneous biological bodies under complex excitations," 1978 International Symposium on the Biological Effects of Electromagnetic Waves, Ottawa, Canada, June 1978.
9. K.M. Chen, "A simple physical picture of tensor Green's function in source region," Proc. IEEE, Vol. 65, pp. 1202-1204, 1977.
10. C.T. Tai, "On the eigenfunction expansion of dyadic Green's functions," Proc. IEEE, Vol. 61, pp. 480-481, 1973.
11. C.T. Tai, and P. Rozenfeld, "Different representation of dyadic Green's functions for a rectangular cavity," IEEE Trans. Microwave Theory Tech., Vol. MIT-24, pp. 597-601, Sept. 1976.
12. Y. Rahmat-Samii, "On the question of computation of the dyadic Green's function at the source region in waveguides and cavities," IEEE Trans. Microwave Theory Tech., Vol. MIT-23, pp. 762-765, Sept. 1975.
13. R.E. Collin, "On the incompleteness of E and H modes in waveguides," Can. J. Phys., Vol. 51, pp. 1136-1140, June 1973.
14. A.G. Howard, et al., "On the longitudinal component of the Green's function inside," Proc. IEEE, Vol. 61, pp. 1124-1126, Dec. 1973.

15. A.Q. Howard and D.B. Seidel, "Singularity extraction in kernel functions in a closed region problem," Radio Science, Vol. 13, pp. 425-429, May-June, 1978.
16. W.A. Johnson, A.Q. Howard, and D.G. Dudley, "On the irrotational component of the electric Green's dyadic," Radio Science, Vol. 14, pp. 961-967, November-December, 1979.
17. A.D. Yaghjian, "Electric dyadic Green's functions in the source region," Proc. IEEE, Vol. 68, pp. 248-263, Feb. 1980.
18. S.W. Lee, J. Boersma, C.L. Law and G.A. Deschamps, "Singularity in Green's function and its numerical evaluation," IEEE Transactions on Ant. and Prop., Vol. AP-28, pp. 311-317, May 1980.
19. J.J.H. Wang, "Analysis of a three-dimensional arbitrarily shaped dielectric or biological body inside a rectangular waveguide," IEEE Trans. Microwave Theory Tech., Vol. MTT-26, pp. 457-462, July 1978.
20. R.E. Collin, Field Theory of Guided Waves, McGraw-Hill Book Co., Inc., New York 1969.
21. C.T. Tai, "Electric dyadic Green's functions in the source region," submitted to IEEE proceedings for publication; communicated to this author 2 July 1980.
22. J. Arzac, Fourier Transforms and the Theory of Distribution, Prentice-Hall, Englewood Cliffs, N.J., 1966.
23. J. Van Bladel, Electromagnetic Fields, McGraw-Hill Book Co., Inc., New York 1964, Appendix 3.
24. P. Antosik, J. Mikusiński and R. Sikorski, Theory of Distributions - the Sequential Approach, Elsevier Scientific Publishing Company, Amsterdam, 1973.
25. L. Schwartz, Théorie des distributions, Vol. I, Actualities Scientifiques et Industrielles, Hermann & Cie, Paris 1957.
26. L. Schwartz, Généralisation de la notion de fonction, de dérivation, de transformation de Fourier, et applications mathématiques et physiques, Annales Univ. Grenoble, Vol. 21, pp. 57-74, 1945.

27. F. E. Harrington, Time-Harmonic Electromagnetic Fields, McGraw-Hill Book Co., Inc., New York, 1961.
28. J. L. H. Wang and C. Papanicolaopolous, "Analysis and Measurements of three-dimensional arbitrarily-shaped dielectric scatterers", Interim Report, Contract F19628-78-C-0223, Rome Air Development Center, Griffiss AFB, N.Y., February 1980, AD-80417.
29. R.C. Johnson, H.A. Ecker, and R.A. Moore, "Compact Range Techniques and Measurements", IEEE Transactions on Ant. and Prop., Vol. AP-17, No. 5, pp. 568-576, Sept. 1969.
30. D.W. Hess, F.G. Willwerth and R.C. Johnson, "Compact Range Improvements and Performance at 30 GHz", 1977 International IEEE AP-S Symposium, pp. 264-267, Stanford, Cal., June 1977.
31. R.W.P. King and T.T. Wu, The Scattering and Diffraction of Waves, Harvard University Press, Cambridge, Mass., 1957.
32. I.S. Rombauer and M.R. Becker, The Joy of Cooking, The Bobbs-Merrit Co., New York, pp. 389-424, 1953.
33. P. Blacksmith, Jr., and R.B. Mack, "On Measuring the Radar Cross Sections of Ducks and Chickens", Proceedings of IEEE, Vol. 53, p. 1125, August, 1965.
34. A.W. Guy, "Analyses of Electromagnetic Fields Induced in Biological Tissues by Thermographic Studies on Equivalent Phantom Models", IEEE Trans. Microwave Theory Tech., Vol. MTT-19, No. 2, pp. 205-214, February 1971.
35. E.C. Burdette, F.L. Cain and J. Seals, "In-Vivo Determination of Energy Absorption in Biological Tissue", Final Technical Report, U.S. Army Grant DAAG29-75-G-0182, Engineering Experiment Station, Georgia Institute of Technology, January 1979.
36. B.S. Guru and K.M. Chen, "Experimental and Theoretical Studies on Electromagnetic Fields Induced Inside Finite Biological Bodies", IEEE Trans. Microwave Theory Tech., Vol. MTT-24, No. 7, pp. 433-440, July 1976.
37. D.P. Nyquist, K.M. Chen and B.S. Guru, "Coupling Between Small Thin-Wire Antennas and a Biological Body", IEEE Transactions on Ant. and Prop., Vol. AP-25, No. 6, Nov. 1977.
38. M.J. Hagmann, O.P. Gandhi, and C.H. Durney, "Numerical Calculation of Electromagnetic Energy Deposition for a Realistic Model of Man", IEEE Transactions on Ant. and Prop., Vol. MTT-27, No. 9, Sept. 1979.

39. J.H. Richmond, "Digital Computer Solutions of the Algebraic Equations for Scattering Problems", Proc. IEEE, Vol. 53, pp. 796-804, August 1965.
40. D.C. Adams and L.L. Lo, "Remote Sensing of Conductivity by Multiple Resonances in RCS", IEEE Transactions on Ant. and Prop., Vol. AP-21, No. 4, p. 554-561, July 1973.
41. J.J.H. Wang, "Numerical Analysis of Three-dimensional Arbitrarily-shaped Conducting Scatterers by Trilateral Surface Cell Modeling", Radio Science, Vol. 13, No. 6, pp. 947-952, Nov.-Dec., 1978.
42. J.J.H. Wang, "Study of Surface-patch Techniques for Modeling 3-D Radiating or Scattering Objects", Interim Technical Report, Contract F19628-78-C-0224, Engineering Experiment Station, Georgia Institute of Technology, Dec. 1979 (being approved for public release). A084185.
43. T. Ferguson, T.H. Lehman and R.J. Balestri, "Efficiency Solution of Large Moment Problems: Theory and Small Problem Results", IEEE Transactions on Ant. and Prop., Vol. AP-24, No. 2, pp. 230-235, March 1976.
44. R.J. Balestri, T.R. Ferguson and E.R. Anderson, "General Electromagnetic Model for the Analysis of Complex Systems". Technical Report RADC-TR-77-137, Vol. I and II, Rome Air Development Center (RBCT), Griffis AFB, N.Y., April 1977, Vol I - A046026, Vol II - A046027.
45. B.R. Carbrey, "User Manual: Virtual Memory Subroutines". Picatinny Arsenal, Dover, N.J., Transmitted to Georgia Tech, November 1977.
46. IMSL Library Manual, International Mathematical and Statistical Libraries, Inc., Houston, Texas, 1979.
47. L.L. Bonham and L.V. Blake, "Radar Echoes from Birds and Insects", Sci. Monthly, Vol. 82, p. 204-209, 1956.
48. D. Levine, Radargrammetry, McGraw-Hill Book Co., Inc., . 235, New York, 1960.
49. G.E. Pollon, "Distributions of Radar Angels", IEEE Trans. Aerospace and Elect. Syst., Vol. AES-8, No. 6, November 1972.
50. J.J.H. Wang, "Analysis and Computer Modeling of Chaff Clouds", Georgia Tech Interim Report No. 3 on Project A-1840, Subcontract No. A6HM-567195 from Autonetics Group, Rockwell International Corporation, Prime Contract N00024-76-C-7107, Atlanta, Ga., July 1976.

51. W.P. Cooke, J.J. Wang and C.E. Ryan, Jr., "Consulting and Research Services in Support of the DG-AEGIS Electromagnetic Analysis Programs and the Ship Image Program", Georgia Tech Final Report on Project A-1819-002, Subcontract A6HM-567192 from Autonetics Group, Rockwell International Corporation, Atlanta, Ga., March 1972.
52. W.P. Cooke, J.J. Wang, B.J. Cown, and J.D. Adams, "Consulting and Research Services in Support of the Ship Image Model Development Program", Georgia Tech Report on Project A-1999, Subcontract No. A7HM-567218 from Autonetics Group, Rockwell International Corporation, Prime Contract No. N00024-76-C-7294, Atlanta, Ga., July 1972.

APPENDIX I
SUBROUTINES USED IN LOCAL-FILE MANIPULATION ALGORITHM

APPENDIX I
SUBROUTINES USED IN LOCAL-FILE MANIPULATION ALGORITHM

Sixteen of the subroutines are written in FORTRAN V and eleven of them are in the COMPASS machine language.

A. Subroutines Written in FORTRAN V

- 1) MMCDCOM - Decomposes a complex matrix to lower and upper submatrices.
- 2) MMCFBS - Solves the decomposed matrix using forward and backward substitution.
- 3) MMCRNRM - Normalizes a row in a matrix by dividing each (except the first) element of the row by its first element. The first element of the new row is then replaced by its reciprocal.
- 4) MMCRSUB - Performs complex row-subtraction and the pivoting operation in the lower-upper decomposition method.
- 5) MMINIT - Pre-sets matrix storage allocation among several local-files, allocates local-file addresses and allocates buffers for the first few rows. This is an initialization of parameters, which may be altered during the execution of the program.
- 6) MMSSTAT - Provides statistical information regarding the status and the efficiency of the core and buffer storage allocation as well as other program execution characteristics.
- 7) MMGBUF - Searches for and provides a free buffer upon request.
- 8) MMINBND - Assigns the priority for a row based on whether it is of current interest or not.
- 9) MMFSET - Sets up a file-environment table for an I/O operation and starts the I/O operation.
- 10) MMLOCK - Assigns buffers and insures that the buffer is available for usage.
- 11) MMGTRA - Gets the disc address of a matrix-row from the address tables such as the row map, buffer maps, FET, etc.
- 12) MMSINBD - Sets a map of in-bound/out-of-bound rows for later use by MMINBND.
- 13) MMGRDW - Gets a matrix row from disc and stores it into the core through the buffer.

- 14) MMSROW - Gets a matrix-row from the core and stores it into the disc through the buffer. This is the reverse process of MMGROW.
- 15) MMSLIM - Determines and updates the priority table which assigns the matrix rows to be stored into the core memory.
- 16) MMBAHED - Gets matrix rows to be used soon from the disc and stores them into the buffer. This is a portion of MMGROW and is not needed for MMSROW.

B. Subroutines Written in COMPASS

- 1) MMALLOC - Allocates central memory space for the buffers to be used; Sets up parameters such as the number of local-files to hold the generated matrix, the number of rows per super-row, and the number of simultaneous I/O requests that are allowed.
- 2) MMLINK - Links subroutines which allocate buffers, set file environment tables, row-maps, buffer-maps, and subroutines indirectly calling other subroutines.
- 3) MMSUPRT - Contains a collection of subroutines to direct the computer to perform several simultaneous operations to take advantage of the overlapping mode of execution of the Cyber-74.
- 4) MMCIO - Invokes "CIO" to process FET (file environment table). FET is a file-table containing information such as the address of the randomly-accessed records of a particular file. "CIO" stands for combined I/O operations and is used to perform the I/O operation in COMPASS. In FORTRAN, COBOL and other high level languages the I/O is performed automatically.
- 5) MMSG - Displays messages on the computer-operator console and optionally displays messages in the dayfile.
- 6) CDD - Converts binary display to decimal display.
- 7) MCKGL - Monitors the I/O process to insure that the I/O operation is completed.
- 8) MMCOPY - Copies data from one array to the other.
- 9) MMRBSY - Checks if an I/O for a particular super-row is in process.
- 10) MMSPLIN - Sets the PPU limits. (A peripheral processor unit (PPU) is a small processor which provides communication paths between the central processor and the individual peripheral devices such as the disc unit. In this subroutine the user can limit or expand the number of simultaneously executed I/O requests depending on the computer's load, time of day, etc.
- 11) MMUPACK - Unpacks the row-map and buffer-map. Keeps track on a table of file-numbers corresponding to row, super rows, and buffers. Checks if a buffer cannot be released for a particular row.

APPENDIX II
MATRIX SOLUTION BY THE LOWER-UPPER DECOMPOSITION METHOD.

APPENDIX II
MATRIX SOLUTION BY THE LOWER-UPPER DECOMPOSITION METHOD

The lower-upper decomposition method for the solution of a matrix equation is based on the following theorem .

Theorem. Let $[A]$ denote a $N \times N$ square matrix whose elements are denoted by a_{ij} , where i and j refer to the row and column of the element. Let $[A_k]$ denote a $k \times k$ square matrix which is a left-upper submatrix of $[A]$ defined as

$$[A_k] = [a_{ij}]; i, j = 1, \dots, k. \tag{AI-1}$$

If all the submatrices $[A_k]$, $k=1, \dots, N$, are nonsingular, then $[A]$ can be decomposed uniquely into the following form

$$[A] = [L] [U] \tag{AII-2}$$

where all the three matrices are all of dimensions $N \times N$, and $[L]$ and $[U]$ are referred to as the lower and upper triangular matrices of the following form

$$L = \begin{bmatrix} 1 & 0 & 0 & \dots & 0 \\ \ell_{21} & 1 & 0 & \dots & 0 \\ \vdots & \vdots & \vdots & \ddots & \vdots \\ \ell_{n1} & \ell_{n2} & \dots & \dots & 1 \end{bmatrix} \tag{AII-3}$$

$$U = \begin{bmatrix} u_{11} & u_{12} & \dots & u_{1n} \\ 0 & u_{22} & \dots & u_{2n} \\ \vdots & \vdots & \ddots & \vdots \\ 0 & 0 & \dots & u_{nn} \end{bmatrix} \tag{AII-4}$$

By transferring [A] into the product of two such matrices, one can solve the matrix equation by forward and backward substitution to be explained later. First we will show how [L] and [U] can be evaluated.

$$\begin{aligned}
 [A] &= \begin{bmatrix} u_{11} & u_{12} & u_{13} & \dots & \dots & \dots \\ \lambda_{21}u_{11} & \lambda_{21}u_{12} + u_{22} & \lambda_{21}u_{13} + u_{23} & \dots & \dots & \dots \\ \lambda_{31}u_{11} & \lambda_{31}u_{12} + \lambda_{32}u_{22} & \lambda_{31}u_{13} + \lambda_{32}u_{23} + u_{33} & \dots & \dots & \dots \\ \vdots & \vdots & \vdots & \vdots & \vdots & \vdots \\ \vdots & \vdots & \vdots & \vdots & \vdots & \vdots \end{bmatrix} \\
 &= \begin{bmatrix} a_{11} & a_{12} & a_{13} & \dots & \dots & \dots \\ a_{21} & a_{22} & a_{23} & \dots & \dots & \dots \\ \vdots & \vdots & \vdots & \vdots & \vdots & \vdots \\ \vdots & \vdots & \vdots & \vdots & \vdots & \vdots \\ a_{n1} & a_{n2} & a_{n3} & \dots & \dots & a_{nn} \end{bmatrix} \quad [AII-5]
 \end{aligned}$$

By equating the individual elements in the equation above, we obtain:

a) For the first row of U

$$u_{1j} = a_{1j} \quad j=1,2,\dots,N$$

b) For the first column of L

$$l_{i1} = a_{i1}/u_{11} \quad i=1,2,\dots,N$$

c) For the second row of U

$$u_{2j} = a_{2j} - l_{21}u_{1j} \quad j=2,3,\dots,N$$

d) For the second column of L

$$l_{i2} = (a_{i2} - l_{i1}u_{12})/u_{22} \quad i=2,3,\dots,N$$

(3) The third row of U

$$u_{3j} = a_{3j} - \sum_{k=1}^{p-1} u_{3k} a_{kj} - u_{2j} a_{2j}$$

.....

(A11-6)

All the matrix elements u_{ij} and a_{ij} can then be obtained in sequence according to the set of Equations (A11-6). Note that the simple process of determining the unknown u_{ij} and a_{ij} involves only straightforward substitution of the known a_{ij} and the previously calculated u_{ij} and a_{ij} following the order specified in Equation (A11-6). Note that Equation (A11-6) can be denoted in general as

$$u_{pj} = a_{pj} - \sum_{k=1}^{p-1} u_{pk} a_{kj} \quad j=p, p+1, \dots, N$$

$$a_{iq} = (a_{iq} - \sum_{k=1}^{q-1} u_{ik} a_{kq}) / u_{qq} \quad i=q+1, \dots, N \quad (\text{A11-7})$$

Let us now use this lower-upper decomposition method to solve the following matrix equation

$$[A] [X] = [b] \quad (\text{A11-8})$$

Applying Equation (A1-2) to (A1-8), we have

$$[L] [U] [X] = [b] \quad (\text{A11-9})$$

or then

$$[Y] = [U] [X], \quad (\text{A11-10})$$

We have

$$[L] [y] = [b] \tag{AII-11}$$

Equation (AII-11), which can be written explicitly as follows

$$\begin{aligned} y_1 &= b_1 \\ l_{12}y_1 + l_{22}y_2 &= b_2 \\ \dots\dots\dots & \\ l_{n1}y_1 + l_{n2}y_2 + \dots + l_{nn}y_n &= b_n \end{aligned} \tag{AII-12}$$

can be solved by the trivial forward substitution method, which merely solves the set of equations (AII-12) sequentially by direct substitution of the previously calculated y_i 's.

Next we write Equation (AII-10) explicitly as

$$\begin{aligned} u_{11}x_1 + u_{12}x_2 + \dots + u_{1n}x_n &= y_1 \\ u_{22}x_2 + \dots + u_{2n}x_n &= y_2 \\ \dots\dots\dots & \\ u_{nn}x_n &= y_n \end{aligned} \tag{AII-13}$$

It is now obvious that the unknown x_i 's can be solved sequentially by a back-forward substitution method starting from the last equation since y_n 's have been solved in Equation (AII-12).



MISSION
of
Rome Air Development Center

RADC plans and executes research, development, test and selected acquisition programs in support of Command, Control Communications and Intelligence (C³I) activities. Technical and engineering support within areas of technical competence is provided to ESD Program Offices (POs) and other ESD elements. The principal technical mission areas are communications, electromagnetic guidance and control, surveillance of ground and aerospace objects, intelligence data collection and handling, information system technology, ionospheric propagation, solid state sciences, microwave physics and electronic reliability, maintainability and compatibility.

Printed by
United States Air Force
Hanscom AFB, Mass. 01731

DATE
FILMED
-8